

**MATHEMATICAL MODEL AND NUMERICAL TECHNIQUE
OF BLOOD FLOW IN THE SYSTEM OF HUMAN CORONARY
ARTERIES WITH NO GRAFT AND WITH A BYPASS GRAFT**

BURASKORN NUNTADILOK

**A THESIS SUBMITTED IN PARTIAL FULFILLMENT
OF THE REQUIREMENTS FOR
THE DEGREE OF DOCTOR OF PHILOSOPHY
(MATHEMATICS)
FACULTY OF GRADUATE STUDIES
MAHIDOL UNIVERSITY
2012**

COPYRIGHT OF MAHIDOL UNIVERSITY

Thesis
entitled

**MATHEMATICAL MODEL AND NUMERICAL TECHNIQUE
OF BLOOD FLOW IN THE SYSTEM OF HUMAN CORONARY
ARTERIES WITH NO GRAFT AND WITH A BYPASS GRAFT**

.....
Mr. Buraskorn Nuntadilok
Candidate

.....
Prof. Benchawan Wiwatanapataphee,
Ph.D.
Major advisor

.....
Prof. Julian Poulter, Ph.D.
Co-advisor

.....
Prof. I Ming Tang, Ph.D.
Co-advisor

.....
Lect. Kittisak Chayantrakom, Ph.D.
Co-advisor

.....
Lect. Meechoke Chuedoung, Ph.D.
Co-advisor

.....
Prof. Banchong Mahaisavariya,
M.D., Dip Thai Board of Orthopedics
Dean
Faculty of Graduate Studies
Mahidol University

.....
Prof. Yongwimon Lenbury, Ph.D.
Program Director
Doctor of Philosophy Program in
Mathematics
Faculty of Science, Mahidol University

Thesis
entitled
**MATHEMATICAL MODEL AND NUMERICAL TECHNIQUE
OF BLOOD FLOW IN THE SYSTEM OF HUMAN CORONARY
ARTERIES WITH NO GRAFT AND WITH A BYPASS GRAFT**

was submitted to the Faculty of Graduate Studies, Mahidol University
for the degree of Doctor of Philosophy (Mathematics)

on
October 26, 2012

.....
Mr. Buraskorn Nuntadilok
Candidate

.....
Assoc. Prof. Suwon Tangmanee, Ph.D.
Chair

.....
Prof. Benchawan Wiwatanapataphee,
Ph.D.
Member

.....
Prof. Julian Poulter, Ph.D.
Member

.....
Prof. I Ming Tang, Ph.D.
Member

.....
Lect. Kittisak Chayantrakom, Ph.D.
Member

.....
Lect. Meechoke Chuedoung, Ph.D.
Member

.....
Prof. Banchong Mahaisavariya,
M.D., Dip Thai Board of Orthopedics
Dean
Faculty of Graduate Studies
Mahidol University

.....
Prof. Skorn Mongkolsuk, Ph.D.
Dean
Faculty of Science
Mahidol University

ACKNOWLEDGEMENTS

I would like to express my deep and sincere gratitude to my advisor, Professor Benchawan Wiwatanapataphee for her invaluable guidance and continuous support. Her great knowledge and experience have inspired me to do research.

I am grateful to my co-advisors, Professor Julian Poulter, Professor I Ming Tang, Dr. Kittisak Chayantrakom, and Dr. Meechoke Chuedoung, for their kindness, valuable advice and suggestions. I deeply thank my external examiner, Associate Professor Suwan Thangmanee, for his advice and comments.

Special appreciation is further extended to my teachers who taught me and gave me invaluable knowledge. My thanks also go to all staff members of the Department of Mathematics for their great cooperation and help. I would like to thank all of my friends for their helpfulness, friendship and encouragement.

I gratefully acknowledge the Faculty of Science and graduate school, Mahidol University for the financial support for my presentation in Singapore.

Finally, I would like to deeply thank my family for their love and encouragement and support throughout my study.

Buraskorn Nuntadilok

MATHEMATICAL MODEL AND NUMERICAL TECHNIQUE OF BLOOD FLOW IN THE SYSTEM OF HUMAN CORONARY ARTERIES WITH NO GRAFT AND WITH A BYPASS GRAFT

BURASKORN NUNTADILOK 5136161 SCMA/D

Ph.D. (MATHEMATICS)

THESIS ADVISORY COMMITTEE : BENCHAWAN WIWATANAPATAPHEE, Ph.D., JULIAN POULTER, Ph.D., I MING TANG, Ph.D., KITTISAK CHAYANTRAKOM, Ph.D., MEECHOKE CHUEDOUNG, Ph.D.

ABSTRACT

In this research, we investigated the behavior of blood flow in the system of human coronary arteries with no graft and with a bypass graft. The three-dimensional computational domain consists of the ascending aorta, the arch of aorta, the proximal left coronary artery, the right coronary artery (RCA), and a graft. Blood is considered as an incompressible non-Newtonian fluid. The continuity equation and Navier-Stokes equations with pulsatile conditions on the boundaries, governing the motion of blood flow, are solved by using finite element method.

The numerical results show that at the stenosis region the pressure of blood drops dramatically, the shear rate tends to increase, and the velocity of blood decreases as the degree of stenosis increases. The numerical results also show that the coronary artery system with a bypass graft can improve the blood pressure along the stenosed RCA and decrease the shear rate and the blood velocity at the stenosis site.

KEY WORDS: BLOOD FLOW / BYPASS GRAFT / CORONARY ARTERY / STENOSIS / FINITE ELEMENT METHOD

117 pages

แบบจำลองทางคณิตศาสตร์และเทคนิคเชิงตัวเลขของการไหลของเลือดในระบบหลอดเลือดหัวใจ
ของมนุษย์ที่ไม่มีการผ่าตัดหลอดเลือดหัวใจบายพาสและมีการผ่าตัด

MATHEMATICAL MODEL AND NUMERICAL TECHNIQUE OF BLOOD FLOW IN THE
SYSTEM OF HUMAN CORONARY ARTERIES WITH NO GRAFT AND WITH A BYPASS
GRAFT

บุรุษกร นันทิลก 5136161 SCMA/D

ปร.ด. (คณิตศาสตร์)

คณะกรรมการที่ปรึกษาวิทยานิพนธ์ : เบญจวรรณ วิวัฒน์ปฐพี, Ph.D., JULIAN POULTER, Ph.D.,
I MING TANG, Ph.D., กิตติศักดิ์ ชัยนตราคม, Ph.D., มีโชค ชูดวง, Ph.D.

บทคัดย่อ

ในงานวิจัยนี้ เราตรวจสอบพฤติกรรมของการไหลของเลือดในระบบของหลอดเลือด
หัวใจของมนุษย์ที่ไม่มีการผ่าตัดหลอดเลือดหัวใจบายพาสและมีการผ่าตัด โดยใช้โดเมนเชิงคำนวณ
สามมิติซึ่งประกอบด้วย หลอดเลือดแดงใหญ่ส่วนต้น, หลอดเลือดแดงใหญ่ส่วนกลาง, ส่วนต้นของ
หลอดเลือดหัวใจซ้าย, หลอดเลือดหัวใจขวา, และเส้นเลือดบายพาส โดยที่เลือดนั้นถูกกำหนดให้
เป็นของเหลวอนนิวโตเนียนแบบอัดตัวไม่ได้ (incompressible non-Newtonian fluid) สมการ
ควบคุมการไหลของเลือดคือ สมการความต่อเนื่อง (Continuity equation) และสมการนาเวียร์-
สโตกส์ (Navier-Stokes equations) ที่ใช้เงื่อนไขกวดแกว่งเป็นคาบ (pulsatile) ที่ขอบ และผลเฉลย
หาคำตอบได้โดยใช้วิธีไฟไนต์เอลิเมนต์ (Finite element Method)

ผลเฉลยเชิงตัวเลขแสดงให้เห็นว่า ในบริเวณที่หลอดเลือดที่ตีบตัน ความดันของเลือด
ลดลงอย่างเห็นได้ชัด, แรงเฉือนที่ผนังของหลอดเลือดมีแนวโน้มที่สูงขึ้น และความเร็วของเลือด
ลดลง เมื่อระดับของการตีบของหลอดเลือดเพิ่มขึ้น นอกจากนี้ผลจากการคำนวณยังแสดงให้เห็นว่า
การผ่าตัดหลอดเลือดหัวใจบายพาสสามารถปรับสภาพแรงดันเลือดในบริเวณหลอดเลือดหัวใจตีบ
ตันให้ดีขึ้นได้ และสามารถลดแรงเฉือนและความเร็วของเลือดในบริเวณที่มีการตีบตันได้อีกด้วย

CONTENTS

	Page
ACKNOWLEDGEMENTS	iii
ABSTRACT (ENGLISH)	iv
ABSTRACT (THAI)	v
LIST OF TABLES	ix
LIST OF FIGURES	x
NOMENCLATURE	xix
CHAPTER I INTRODUCTION	1
1.1 Cardiovascular System	1
1.1.1 Human Heart	1
1.1.2 Blood	2
1.1.3 Blood Vessels	3
1.2 Cardiovascular Diseases	4
1.3 Coronary Artery Disease	5
1.4 Treatment of Coronary Artery Disease	6
1.4.1 Medical Treatment.....	6
1.4.2 Coronary Angioplasty and Stent Placement	6
1.4.3 Coronary Artery Bypass Graft	7
1.5 Scope and Objectives	8
1.6 Outline of Thesis	9
CHAPTER II LITERATURE REVIEW	10
2.1 General Overview	10
2.2 Experimental Studies of Blood Flow	11
2.3 Numerical Studies of Blood Flow	13
2.3.1 The Numerical Studies using an Artificial Geometry	14
2.3.2 The Numerical Studies using a Realistic Geometry	16

CONTENTS (cont.)

	Page
2.4 Numerical Studies of Blood Flow in a Stenosed Artery with a Bypass Graft	17
2.4.1 The Numerical Studies using an Artificial Geometry	18
2.4.2 The Numerical Studies using a Realistic Geometry	19
2.5 Concluding Remarks	19
CHAPTER III GEOMETRY CONSTRUCTION	20
3.1 General Overview	20
3.2 Geometry Construction using Mimics Software	20
3.2.1 Importing CT Data Files	21
3.2.2 Specifying a Region of the Domain	23
3.2.3 Extracting and Constructing the 3-D Domain	25
CHAPTER IV MATHEMATICAL MODEL	28
4.1 General Overview	28
4.2 Geometrical Description	28
4.3 Governing Equations	31
4.4 Boundary Equations	33
CHAPTER V FINITE ELEMENT FORMULATION	35
5.1 General Overview	35
5.2 Finite Element Formulation	35
5.3 Numerical Implementation	39
5.3.1 Three-Dimensional Tetrahedral Elements	39
5.3.2 Surface Elements	44
5.4 Numerical Algorithm	46
5.5 Mesh Sensitivity Analysis	47
CHAPTER VI NUMERICAL EXAMPLES	58
6.1 General Overview	58
6.2 The Effect of Branching in a Human Coronary Artery	59

CONTENTS (cont.)

	Page
6.2.1 Pressure	60
6.2.2 Wall Shear Stress	60
6.2.3 Velocity Field	60
6.3 The Effect of the Non-Newtonian Property of Blood	65
6.3.1 Pressure	65
6.3.2 Wall Shear Stress	65
6.3.3 Velocity Field	65
6.4 The Effect of Stenosis in a Human Coronary Artery	71
6.4.1 Pressure	71
6.4.2 Wall Shear Stress	71
6.4.3 Velocity Field	72
6.5 The Effect of Bypass Grafting in a Human Coronary Artery	79
6.5.1 Pressure	79
6.5.2 Wall Shear Stress	79
6.5.3 Velocity Field	80
CHAPTER VII SUMMARY AND CONCLUSIONS	101
7.1 Summary of the Research	101
REFERENCES	103
BIOGRAPHY	117

LIST OF TABLES

Table	Page
4.1 The properties of the computational domain	31
4.2 The parameter values used in Carreau's shear-thinning model	32
4.3 Values of the parameters \bar{p} , \bar{Q} , α_k^Q , β_k^Q , α_k^p and β_k^p	34
5.1 The number of tetrahedral elements (<i>NE</i>) and degrees of freedom (<i>DF</i>) of the computational domains with no graft	48
5.2 The number of tetrahedral elements (<i>NE</i>) and degrees of freedom (<i>DF</i>) of the computational domains with a bypass graft	49

LIST OF FIGURES

Figure	Page
1.1 The cardiovascular system	1
1.2 Structure diagram of the human heart from an anterior view	2
1.3 The proportion of human blood components	3
1.4 Three main types of blood vessels: artery, capillary and vein	3
1.5 Causes of death (2008)	5
1.6 The angiogram of an RCA with stenosis	5
1.7 The coronary angioplasty and stent placement: (a) a coronary artery with stenosis region; (b) inserting the balloon with stent; (c) inflating the balloon with stent; and (d) removing the balloon	6
1.8 The coronary artery bypass graft (CABG)	7
3.1 The three-dimensional domain of the coronary artery system with bypass grafts	27
4.1 The system of coronary arteries with four bypass grafts constructed from Mimics software	29
4.2 Three-dimensional computational domain of coronary artery system with a bypass graft	29
4.3 The computational domains of the coronary artery system with no graft and with a bypass graft having four different degrees of stenosed RCA including 0% (normal), 40%, 63% and 72%	30
4.4 The domain with inflow surface Γ^{aorta} and ten outflow surfaces Γ_1^{aorta} , Γ_2^{aorta} , Γ_3^{aorta} , Γ_4^{aorta} , Γ_1^{RCA} , Γ_2^{RCA} , Γ_3^{RCA} , Γ_4^{RCA} , Γ_1^{LCA} and Γ_2^{LCA}	30
5.1 The tetrahedral elements	40
5.2 The surfaces of tetrahedral element	44
5.3 The investigated point of mesh sensitivity analysis	47
5.4 The element mesh of the domain with no graft	48
5.5 The element mesh of the domain with a bypass graft	49

LIST OF FIGURES (cont.)

Figure	Page
5.6 The mesh sensitivity analysis of the computational domain having 0% stenosed RCA with no graft by comparing the pressures and velocities at point P (Figure 5.3) at the peak of systole: (a) blood pressure; (b) blood velocity	50
5.7 The mesh sensitivity analysis of the computational domain having 40% stenosed RCA with no graft by comparing the pressures and velocities at point P (Figure 5.3) at the peak of systole: (a) blood pressure; (b) blood velocity	51
5.8 The mesh sensitivity analysis of the computational domain having 63% stenosed RCA with no graft by comparing the pressures and velocities at point P (Figure 5.3) at the peak of systole: (a) blood pressure; (b) blood velocity	52
5.9 The mesh sensitivity analysis of the computational domain having 72% stenosed RCA with no graft by comparing the pressures and velocities at point P (Figure 5.3) at the peak of systole: (a) blood pressure; (b) blood velocity	53
5.10 The mesh sensitivity analysis of the computational domain having 0% stenosed RCA with a bypass graft by comparing the pressures and velocities at point P (Figure 5.3) at the peak of systole: (a) blood pressure; (b) blood velocity	54
5.11 The mesh sensitivity analysis of the computational domain having 40% stenosed RCA with a bypass graft by comparing the pressures and velocities at point P (Figure 5.3) at the peak of systole: (a) blood pressure; (b) blood velocity	55

LIST OF FIGURES (cont.)

Figure	Page
5.12 The mesh sensitivity analysis of the computational domain having 63% stenosed RCA with a bypass graft by comparing the pressures and velocities at point P (Figure 5.3) at the peak of systole: (a) blood pressure; (b) blood velocity	56
5.13 The mesh sensitivity analysis of the computational domain having 72% stenosed RCA with a bypass graft by comparing the pressures and velocities at point P (Figure 5.3) at the peak of systole: (a) blood pressure; (b) blood velocity	57
6.1 The pulsatile pressure and flow rate at the inflow surface of the aorta	58
6.2 The computational domains of the coronary artery system (a) with no branch; and (b) with branches	59
6.3 The investigated RCA axis and inlet and outlet of the RCA	59
6.4 The pressure along the RCA axis obtained from the model with no branch (dashed line) and model with branches (solid line) at two different times: (a) at the peak of systole; and (b) at the peak of diastole	61
6.5 The wall shear stress along the RCA axis obtained from the model with no branch (dashed line) and model with branches (solid line) at two different times: (a) at the peak of systole; and (b) at the peak of diastole	62
6.6 The velocity field obtained from the model with no branch (dashed line) and model with branches (solid line) (a) at the entrance of the main artery artery of the RCA; and (b) at the end of the main artery of the RCA during a cardiac cycle	63
6.7 The investigated RCA axis and three investigated planes consisting of plane A, plane B, and plane C	64
6.8 The investigated line a_0a_1 , b_0b_1 , and c_0c_1 in plane A, plane B, and plane C, respectively	64

LIST OF FIGURES (cont.)

Figure	Page
6.9 The pressure along the RCA axis obtained from the Newtonian model (dashed line with circle) and non-Newtonian model (solid line) at two different times: (a) at the peak of systole; and (b) at the peak of diastole . . .	66
6.10 The wall shear stress along the RCA axis obtained from the Newtonian model (dotted line) and non-Newtonian model (solid line) at two different times: (a) at the peak of systole; and (b) at the peak of diastole . . .	67
6.11 The maximal flow at investigated line a_0a_1 in plane A (Figure 6.8) obtained from the Newtonian model (dashed line with circle) and non-Newtonian model (solid line) at two different times: (a) at the peak of systole; and (b) at the peak of diastole	68
6.12 The maximal flow at investigated line b_0b_1 in plane B (Figure 6.8) obtained from the Newtonian model (dashed line with circle) and non-Newtonian model (solid line) at two different times: (a) at the peak of systole; and (b) at the peak of diastole	69
6.13 The maximal flow at investigated line c_0c_1 in plane C (Figure 6.8) obtained from the Newtonian model (dashed line with circle) and non-Newtonian model (solid line) at two different times: (a) at the peak of systole; and (b) at the peak of diastole	70
6.14 The pressure along the RCA axis obtained from the model with stenosed RCA having different degrees of stenosis including 0% (dash-dot line), 40% (dashed line), 63% (dotted line), and 72% (solid line), at two different times: (a) at the peak of systole; and (b) at the peak of diastole . . .	73
6.15 The wall shear stress along 3 cm of the RCA axis obtained from the model with stenosed RCA having different degrees of stenosis including 0% (dash-dot line), 40% (dashed line), 63% (dotted line), and 72% (solid line), at two different times: (a) at the peak of systole; and (b) at the peak of diastole	74

LIST OF FIGURES (cont.)

Figure	Page
6.16 The wall shear stress along 10 cm of the RCA axis obtained from the model with stenosed RCA having different degrees of stenosis including 0% (dash-dot line), 40% (dashed line), 63% (dotted line), and 72% (solid line), at two different times: (a) at the peak of systole; and (b) at the peak of diastole	75
6.17 The maximal flow at investigated line a_0a_1 in plane A (Figure 6.8) obtained from the model with stenosed RCA having different degrees of stenosis including 0% (dash-dot line), 40% (dashed line), 63% (dotted line), and 72% (solid line), at two different times: (a) at the peak of systole; and (b) at the peak of diastole	76
6.18 The maximal flow at investigated line b_0b_1 in plane B (Figure 6.8) obtained from the model with stenosed RCA having different degrees of stenosis including 0% (dash-dot line), 40% (dashed line), 63% (dotted line), and 72% (solid line), at two different times: (a) at the peak of systole; and (b) at the peak of diastole	77
6.19 The maximal flow at investigated line c_0c_1 in plane C (Figure 6.8) obtained from the model with stenosed RCA having different degrees of stenosis including 0% (dash-dot line), 40% (dashed line), 63% (dotted line), and 72% (solid line), at two different times: (a) at the peak of systole; and (b) at the peak of diastole	78
6.20 The pressure along the RCA axis obtained from the model having 0% stenosed RCA with no graft (dash-dot line) and with a bypass graft (dash-dot line with star), at two different times: (a) at the peak of systole; and (b) at the peak of diastole	81

LIST OF FIGURES (cont.)

Figure	Page
6.21 The pressure along the RCA axis obtained from the model having 40% stenosed RCA with no graft (dashed line) and with a bypass graft (dashed line with triangle), at two different times: (a) at the peak of systole; and (b) at the peak of diastole	82
6.22 The pressure along the RCA axis obtained from the model having 63% stenosed RCA with no graft (dotted line) and with a bypass graft (dotted line with square), at two different times: (a) at the peak of systole; and (b) at the peak of diastole	83
6.23 The pressure along the RCA axis obtained from the model having 72% stenosed RCA with no graft (solid line) and with a bypass graft (solid line with circle), at two different times: (a) at the peak of systole; and (b) at the peak of diastole	84
6.24 The wall shear stress along 10 cm of the RCA axis obtained from the model having 0% stenosed RCA with no graft (dash-dot line) and with a bypass graft (dash-dot line with star), at two different times: (a) at the peak of systole; and (b) at the peak of diastole	85
6.25 The wall shear stress along 10 cm of the RCA axis obtained from the model having 40% stenosed RCA with no graft (dashed line) and with a bypass graft (dashed line with triangle), at two different times: (a) at the peak of systole; and (b) at the peak of diastole	86
6.26 The wall shear stress along 10 cm of the RCA axis obtained from the model having 63% stenosed RCA with no graft (dotted line) and with a bypass graft (dotted line with square), at two different times: (a) at the peak of systole; and (b) at the peak of diastole	87

LIST OF FIGURES (cont.)

Figure	Page
6.27 The wall shear stress along 10 cm of the RCA axis obtained from the model having 72% stenosed RCA with no graft (solid line) and with a bypass graft (solid line with circle), at two different times: (a) at the peak of systole; and (b) at the peak of diastole	88
6.28 The maximal flow at investigated line a_0a_1 in plane A (Figure 6.8) obtained from the model having 0% stenosed RCA with no graft (dash-dot line) and with a bypass graft (dash-dot line with star), at two different times: (a) at the peak of systole; and (b) at the peak of diastole	89
6.29 The maximal flow at investigated line a_0a_1 in plane A (Figure 6.8) obtained from the model having 40% stenosed RCA with no graft (dashed line) and with a bypass graft (dashed line with triangle), at two different times: (a) at the peak of systole; and (b) at the peak of diastole . . .	90
6.30 The maximal flow at investigated line a_0a_1 in plane A (Figure 6.8) obtained from the model having 63% stenosed RCA with no graft (dotted line) and with a bypass graft (dotted line with square), at two different times: (a) at the peak of systole; and (b) at the peak of diastole . . .	91
6.31 The maximal flow at investigated line a_0a_1 in plane A (Figure 6.8) obtained from the model having 72% stenosed RCA with no graft (solid line) and with a bypass graft (solid line with circle), at two different times: (a) at the peak of systole; and (b) at the peak of diastole . . .	92
6.32 The maximal flow at investigated line b_0b_1 in plane B (Figure 6.8) obtained from the model having 0% stenosed RCA with no graft (dash-dot line) and with a bypass graft (dash-dot line with star), at two different times: (a) at the peak of systole; and (b) at the peak of diastole	93

LIST OF FIGURES (cont.)

Figure	Page
6.33 The maximal flow at investigated line b_0b_1 in plane B (Figure 6.8) obtained from the model having 40% stenosed RCA with no graft (dashed line) and with a bypass graft (dashed line with triangle), at two different times: (a) at the peak of systole; and (b) at the peak of diastole . . .	94
6.34 The maximal flow at investigated line b_0b_1 in plane B (Figure 6.8) obtained from the model having 63% stenosed RCA with no graft (dotted line) and with a bypass graft (dotted line with square), at two different times: (a) at the peak of systole; and (b) at the peak of diastole . . .	95
6.35 The maximal flow at investigated line b_0b_1 in plane B (Figure 6.8) obtained from the model having 72% stenosed RCA with no graft (solid line) and with a bypass graft (solid line with circle), at two different times: (a) at the peak of systole; and (b) at the peak of diastole . . .	96
6.36 The maximal flow at investigated line c_0c_1 in plane C (Figure 6.8) obtained from the model having 0% stenosed RCA with no graft (dash-dot line) and with a bypass graft (dash-dot line with star), at two different times: (a) at the peak of systole; and (b) at the peak of diastole	97
6.37 The maximal flow at investigated line c_0c_1 in plane C (Figure 6.8) obtained from the model having 40% stenosed RCA with no graft (dashed line) and with a bypass graft (dashed line with triangle), at two different times: (a) at the peak of systole; and (b) at the peak of diastole . . .	98
6.38 The maximal flow at investigated line c_0c_1 in plane C (Figure 6.8) obtained from the model having 63% stenosed RCA with no graft (dotted line) and with a bypass graft (dotted line with square), at two different times: (a) at the peak of systole; and (b) at the peak of diastole . . .	99

LIST OF FIGURES (cont.)

Figure	Page
6.39 The maximal flow at investigated line c_0c_1 in plane C (Figure 6.8) obtained from the model having 72% stenosed RCA with no graft (solid line) and with a bypass graft (solid line with circle), at two different times: (a) at the peak of systole; and (b) at the peak of diastole . . .	100

NOMENCLATURE

\mathbf{u}	velocity field of blood
p	pressure of blood
ρ	density of blood
t	time
σ	total stress tensor
I	3×3 identity matrix
η	viscosity of blood
$\dot{\gamma}$	shear rate
\mathbf{D}	rate of deformation tensor
η_0	zero shear viscosity
η_∞	infinite shear viscosity
λ	time constant
n	consistency index

CHAPTER I

INTRODUCTION

1.1 Cardiovascular System

The cardiovascular system is an organ system that transports oxygen and nutrients from the heart throughout the body and returns waste back to the heart. This system has three main components which are the heart, the blood and the blood vessels, as shown in Figure 1.1.

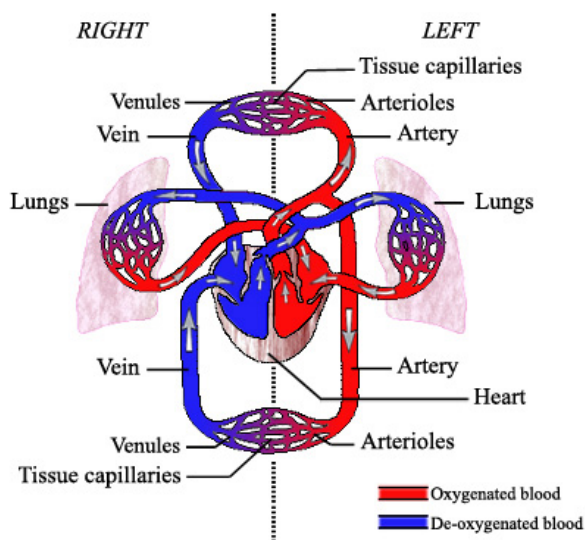


Figure 1.1: The cardiovascular system.

1.1.1 Human Heart

The human heart is the most important organ of the human body. It pumps blood through the blood vessels to all parts of the body. If the heart does not work properly, it can be a cause of human death. The human heart consists of four chambers: two superior atria and two inferior ventricles. The left and the right atria are the receiving chambers and the left and the right ventricles are the discharging chambers. The path of the blood through the heart consists of two

circuits: a pulmonary and a systemic circuit. From all parts of the human body, deoxygenated blood flows through the superior and inferior vena cava into the right atrium (upper right chamber of the heart). This chamber then pumps blood through the tricuspid valve into the right ventricle (lower right part of the heart) before blood being pumped out through the left and right pulmonary arteries to the lungs. Left atrium (upper left chamber of the heart) receives oxygenated blood from the lungs via the left and the right pulmonary veins and then pumps blood through the mitral valve into the left ventricle (lower left part of the heart) before blood being pumped out through the aortic valve to the entire body via the aorta. Typically, the size of the human heart is about the size of a fist [87], or about 250 to 350 grams. Figure 1.2 shows a diagram of the human heart.

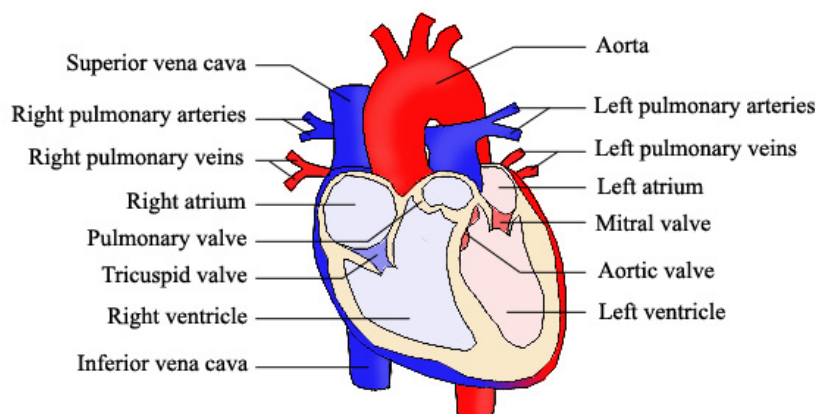


Figure 1.2: Structure diagram of the human heart from an anterior view.

1.1.2 Blood

Blood is a fluid that delivers necessary materials such as oxygen and nutrients to cells and transports the metabolic waste products such as carbon dioxide away from those cells. In addition to transporting substances around the body, blood also helps to fight disease, heal wounds, and control the body temperature. Blood consists of red blood cells, white blood cells and platelets which are floating in a yellow liquid called plasma. Figure 1.3 shows the proportions of blood components.

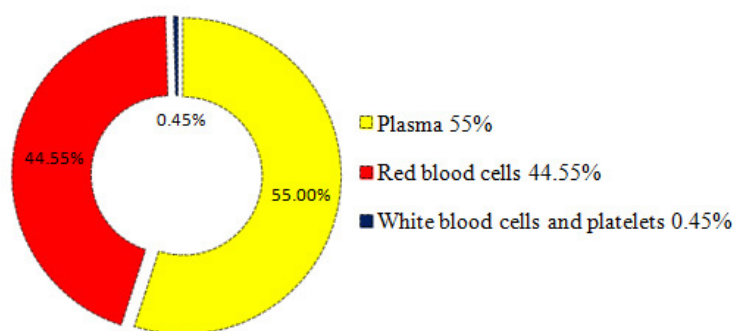


Figure 1.3: The proportions of human blood components.

1.1.3 Blood Vessels

Blood vessels are the part of the circulatory system which transports blood throughout the body. There are three main types of blood vessels: arteries, capillaries, and veins, as shown in Figure 1.4. The arteries are very strong vessels that carry the blood away from the heart. The capillaries are the smallest vessels and have a wall which is a single cell thick. Therefore, the essential substances such as oxygen and nutrients can be exchanged between the blood and the tissue through the capillary wall. The veins are vessels that bring blood from the capillaries back to the heart and they have valves which prevent blood flowing back to the capillaries.

The most important arteries are coronary arteries, the vessels which supply blood to the heart muscle. If there is something that blocks the flow of blood in a coronary artery and causes the heart muscle to not get enough blood, the heart may not work properly. This can cause an angina pectoris or heart attack. Having such a blockage is called coronary artery disease (CAD), one of the cardiovascular diseases.

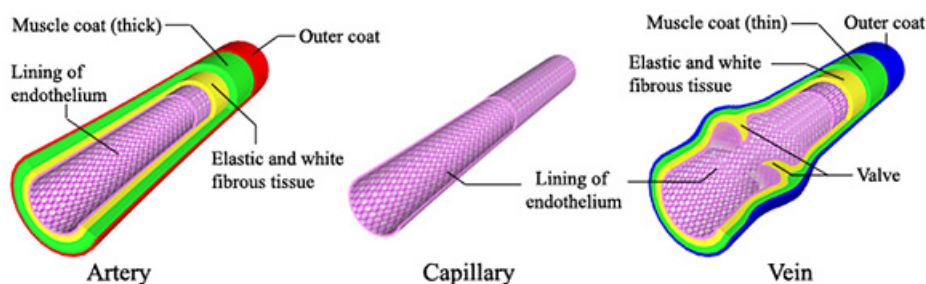


Figure 1.4: Three main types of blood vessels: artery, capillary and vein.

1.2 Cardiovascular Diseases

Cardiovascular diseases (CVDs) are a group of disorders of the heart and blood vessels [91]. These are

- coronary artery disease (CAD) or coronary heart disease (CHD) is a disease of the blood vessels supplying the heart muscle. CAD is sometimes called ischaemic heart disease (IHD);
- cerebrovascular disease is a disease of the blood vessels supplying the human brain;
- peripheral arterial disease is a disease of blood vessels supplying the arms and legs;
- rheumatic heart disease is a disease where the heart muscle and heart valves have been damaged from rheumatic fever caused by streptococcal bacteria;
- congenital heart disease is a disease in which malformations of the heart structure exist at birth;
- deep vein thrombosis and pulmonary embolism are caused by the blood clots which occurs in the leg veins and can dislodge and move to the lungs and heart.

At present, CVDs are the number one of the causes of human deaths in the world. People die annually from CVDs more than from other causes. In 2008, an estimated 17.3 million people died because of CVDs [91], representing 30% of deaths in the world. However, WHO predicted that, in 2030, nearly 23.6 million people will die from these diseases [91]. Therefore, CVDs will continue to be a major cause of human death in the world. Of these deaths, in 2008, about 7.25 million were due to coronary artery disease (CAD) which is 12.8% [92], the highest percentage of the global deaths, as shown in Figure 1.5.

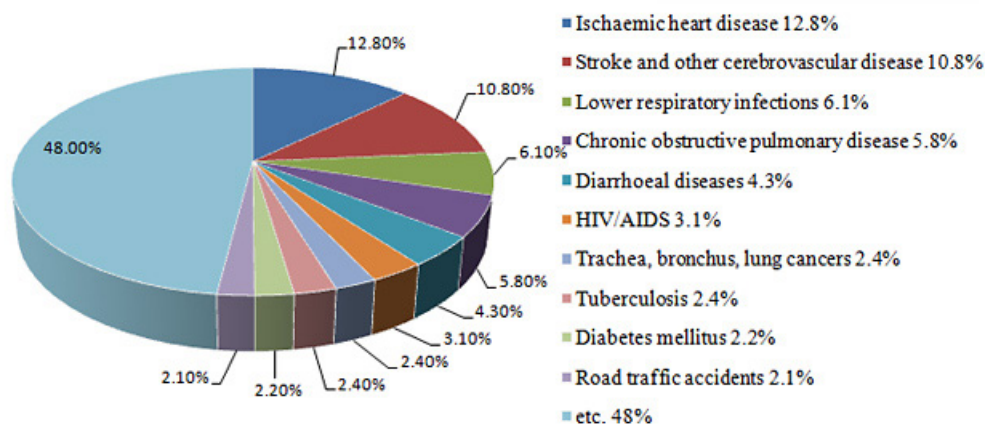


Figure 1.5: Causes of death (2008).

1.3 Coronary Artery Disease

Coronary artery disease (CAD) is the result of the accumulation of plaque in the inner walls of the coronary arteries. The accumulation of plaque causes a blockage which prevents blood flow to the heart. As a result of reducing blood flow to the heart, the heart muscle will not get enough oxygen to work normally and this sometimes causes angina symptoms. Most individuals with coronary artery disease do not have any sign of disease for decades. The disease progresses before the first onset of symptoms, often a sudden heart attack, which can cause death. Figure 1.6 shows a conventional angiogram of a stenosed coronary artery with an arrow pointing to the stenosis at the proximal part of the right coronary artery (RCA). To deal with this problem, there are many ways used to treat CAD such as drugs, stent placement and coronary artery bypass grafting.

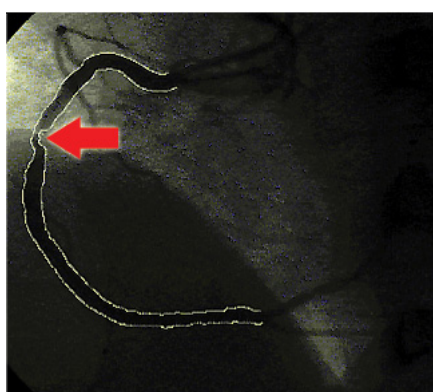


Figure 1.6: The angiogram of an RCA with stenosis.

1.4 Treatment of Coronary Artery Disease

In order to deal with the stenosed coronary arteries, there are many ways used to treat this disease including medical treatment, coronary angioplasty and stent placement, and coronary artery bypass graft surgery.

1.4.1 Medical Treatment

Medical treatment is a method which aims to control symptoms and slow or stop the progression of a disease by using drugs. The doctor may use this method for the first line of treatment if the blockage of blood is less than 70 percent and not severely limiting the blood flow [77]. Medications can help the heart work more efficiently and receive more oxygen-rich blood.

1.4.2 Coronary Angioplasty and Stent Placement

The coronary angioplasty and stent placement is a process where the doctor inserts a thin tube (a catheter) through the artery and inflates a small balloon at the end of the catheter inside the stenosis area. This balloon can help reduce the narrowing in the artery and allow blood to flow better. To permanently open the vessel, the doctor will insert a stent, a small metal wire tube, in the coronary artery. Sometimes the stent may be coated with drugs to reduce the chance of clot recurring. The patient who is considered to be a too high risk for open-heart surgery may have a stent placement instead. Figure 1.7 shows the coronary angioplasty and stent placement.

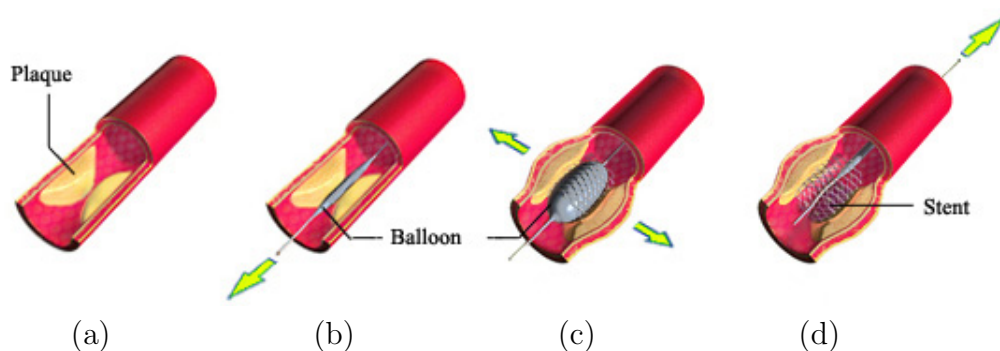


Figure 1.7: The coronary angioplasty and stent placement: (a) a coronary artery with stenosis region; (b) inserting the balloon with stent; (c) inflating the balloon with stent; and (d) removing the balloon.

1.4.3 Coronary Artery Bypass Graft

The coronary artery bypass graft (CABG) surgery is a treatment which creates new routes around the stenosis area or blocked artery to provide adequate blood flow to the heart muscle. The doctor uses new vessels, grafts, from the patient's own veins and arteries to form new paths for the blood supply to the heart. Figure 1.8 shows the coronary artery system with bypass grafts.

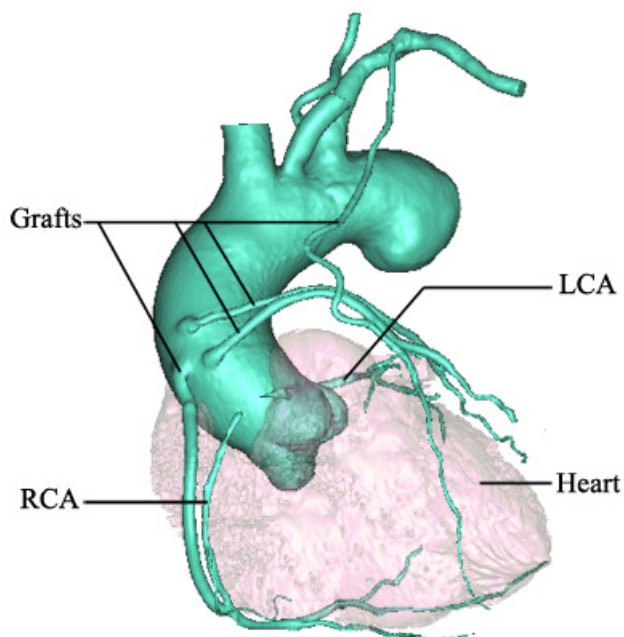


Figure 1.8: The coronary artery bypass graft (CABG).

In order to find ways to prevent, treat, and understand the pathogenesis of CAD, a number of in-vivo and in-vitro experiments have been conducted. To understand behavior of blood flow in a stenosed artery, many researchers have used mathematical models and numerical techniques as a tool for the study of the blood flow problem.

1.5 Scope and Objectives

A numerical simulation of the blood flow through the system of coronary arteries can provide important information to improve our understanding of coronary artery disease and coronary artery bypass graft (CABG) surgery.

The aim of this thesis is to apply mathematical models and numerical methods to study the behavior of blood flow in the coronary artery system with stenosis and a bypass graft. The computational domain of this study consists of the ascending aorta, arch of aorta, right coronary artery (RCA), left coronary artery (LCA) and a graft. The motion of blood flow is governed by the Navier-Stokes equations and the continuity equation. The numerical simulations are based on the Bubnov-Galerkin finite element method using the COMSOL Multiphysics package. The effects of the motion of a vessel wall and a variation of each cardiac cycle are ignored.

The main objectives of this study are to

- investigate the effect of branching in the human right coronary artery;
- compare the effect of Newtonian and non-Newtonian properties of blood;
- investigate the effect of stenosis in the human right coronary artery;
- investigate the effect of bypass grafting in the human right coronary artery with stenosis.

The computational domain of the human coronary artery system, mathematical model of blood flow, and boundary conditions are very close to realistic situations. The results of this research can improve the understanding of CAD and CABG, and lead to the development of clinical diagnosis.

1.6 Outline of Thesis

This thesis is organized into seven chapters as follows.

Chapter one presents the introduction of this study. The information of the cardiovascular system, the cardiovascular diseases, the coronary artery disease and the treatment of coronary artery disease are described in sections 1.1 - 1.4 respectively. The scope and objectives of this study are given in section 1.5.

Chapter two concerns the literature review of work related to our study. The experimental studies of blood flow are reviewed in section 2.2. The numerical simulation of blood flow is presented in section 2.3 and numerical simulation of blood flow in stenosed artery with a bypass graft is proposed in section 2.4.

Chapter three shows the processes of geometry construction. Section 3.2 shows the procedure of constructing a three-dimensional computational domain by using Mimic software.

Chapter four provides the mathematical model and boundary conditions for studying a three-dimensional blood flow through the system of stenosed coronary arteries with no graft and with a bypass graft. Section 4.2 shows the three-dimension computational domain used in this thesis. The governing equations and boundary conditions are presented in sections 4.3 and 4.4.

Chapter five presents the finite element method for the blood flow problem. Sections 5.2 and 5.3 show the finite element formulation and numerical implementation of blood flow. The numerical algorithm is given in section 5.4. The mesh sensitivity of the computational domains is analyzed in section 5.5.

Chapter six presents the numerical studies of blood flow in the coronary artery system. The effects of branching are shown in section 6.2 and the effects of the non-Newtonian property are investigated in section 6.3. In sections 6.4 and 6.5, the effects of different stenosis degrees in the system of coronary arteries with no graft and with a bypass graft are presented.

Finally, the summary and conclusions are given in Chapter seven.

CHAPTER II

LITERATURE REVIEW

2.1 General Overview

Coronary heart disease (CHD) or coronary artery disease (CAD) is the main cause of human death in the world [92], especially in developing and developed countries. CAD occurs when the coronary arteries (LCA and RCA) supplying blood to the heart are narrowed or blocked by fat and plaque. When the coronary arteries cannot get enough blood to serve the heart muscle, the patient will have chest pain or heart attack that lead to the death of human. To treat CAD, the understanding of blood flow behavior in the stenosed coronary arteries is important information for helping a doctor to diagnose or choose a method of treatment.

In the present day, there are many ways used to treat CAD such as using drugs to reduce fat in blood, using a balloon and stent to enlarge the blood vessel in the stenosis region, and using coronary artery bypass grafting (CABG) to make a new pathway for blood flow. However, in the last two decades, the number of human deaths because of CAD has not decreased. Therefore, much experimental and numerical research on blood flow have been proposed and rapidly developed [2, 27, 37, 40, 43, 62, 63, 73].

The experimental studies of blood flow have been performed in both vivo and vitro models [16, 44, 59, 79]. The experiments have used animals or have setup an experimental system to study the flow of blood in a stenosed region. In the numerical studies [33, 72, 81, 95], the researchers have been using a computer to simulate blood flow using software based on the finite element, finite volume or finite difference methods. Most of the numerical studies have considered blood as an incompressible non-Newtonian fluid. The motion of blood flow is governed by the Navier-Stokes equations and the continuity equation. The geometries of the

computational domain, such as straight tube, curved tube, single realistic vessel, and realistic system of coronary arteries, have been constructed for simulating the flow of blood. Furthermore, there are comparisons of blood flow characteristics between experimental measurements and numerical results.

2.2 Experimental Studies of Blood Flow

For the actual understanding of the pathogenesis of coronary artery disease, many in-vivo and in-vitro experiments in blood flow have been done [1, 4, 7, 13, 28, 31, 53, 54, 59, 96].

Laustsen et al. (1995, [45]) developed the technique of nuclear magnetic resonance phase velocity encoding for evaluation of three-dimensional blood flow patterns and regional flows of blood in infrarenal aortic aneurysms in vivo. They found that the blood flow patterns in infrarenal aortic aneurysms were much more complicated than previously studied. The main characteristics of the flow pattern were simultaneous breakdown of the antegrade flow and creation of the retrograde flow components. The frictional forces which were generated by abnormal blood flow patterns in the lumen may be transformed to the aneurysms wall and contributed to the thrombus formation, the aneurysm growth and the risk of rupture. Staalsen et al. (1995, [70, 71]) developed an in-vivo model to study the anastomotic flow patterns. Different anastomosis angles (15, 45 and 90 degrees) were used to investigate the effect of anastomotic geometry. They concluded that their model was an appropriate tool for the study of anastomotic geometry effects on local flow fields in vivo and the 15 degree anastomosis was preferable from the hemodynamic point of view. Deplano and Siouffi (1999, [26]) proposed the experimental and numerical study of pulsatile blood flows through a 75% stenosed tube. In the experimental model, two-dimensional velocity measurements were operated by using a pulsed Doppler ultrasonic velocimeter. A finite element package was used for the transient numerical simulations. They concluded that there was a good agreement between the experimental and numerical results. There were high wall shear stress values at the throat and low wall shear stress values downstream

from the stenosis site. Tang et al. (2001, [75]) presented an experiment-based three-dimensional thick-wall model with fluid-wall interactions for simulating blood flow in stenotic carotid arteries. The experimental measurement of the nonlinear stress-strain relationship was achieved by using an incremental linear elasticity approach. The Navier-Stokes equations were used to describe the motion of blood flow. The results indicated that severe stenosis was the cause of critical flow conditions which were negative pressure, high shear stress, and separation of flow. The stress distribution occurred inside the stenotic region. The numerical results and experimental measurements were compared and reasonable agreement was found. Beratlis et al. (2005, [8]) presented a numerical and experimental investigation of the pulsatile blood flow in a stenotic vessel. They used detailed laser doppler velocimetry measurements to guide the specification of the boundary conditions of the velocity at the inlet. The results presented a borderline turbulent flow which sequentially undergoes transition to turbulence and relaminarization. Kang et al. (2008, [42]) investigated the hemodynamic behavior and red blood cells (RBCs) movement through a micro-stenosis. An in-vitro experiment was performed by using a high speed visualization technique. The transportation of RBCs through the micro-stenosis and flow characteristics were investigated at varying flow rate. At the stenotic region, the results indicated that the RBCs show deformation, twisting, rolling and tumbling motion due to the flow choking characteristics. Shaik et al. (2008, [64]) studied the pulsatile non-Newtonian blood flow in an end-to-side anastomosis model. Computational fluid dynamics was used to explore the role of hemodynamics and compare the numerical results with the experimental data for both steady and pulsatile flow. The results showed good agreement in the velocity profiles but some differences were found in the wall shear stress. They concluded that the distal intimal hyperplasia which is observed in end-to-side artery-graft model might be caused by the oscillations in shear stress along the wall. McCommis et al. (2010, [48]) proposed the experimental study of blood flow through the coronary artery with stenosis. The myocardial blood volume (MBV) and myocardial blood flow (MBF) were examined in a group of twenty-seven mongrel dogs (ten dogs in control group and seventeen dogs with severe coronary stenosis). The

assessment of change in both MBV and MBF might support a more extensive evaluation of myocardial ischemia in the setting of significant coronary artery stenosis. Anastasiou et al. (2012, [5]) studied the pulsatile blood flow in a model of the bifurcated small artery. A solution of aqueous glycerol with small amounts of xanthan gum was used to simulate the viscoelastic properties of blood. The velocity of local flow was measured by using the micro particle image velocimetry (μ -PIV) technique. They concluded that the common hypothesis that blood acted as a Newtonian fluid was not appropriate for blood flow in small arteries.

In 2010, Cheung et al. [21] presented an experimental and numerical model of the hemodynamics of stenosed carotid bifurcation. The numerical simulation indicated that the hemodynamic properties were significant factors for the development of vascular pathology. To validate the reliability of the computational approach, the experimental measurements were carried out by using the PIV technique. Realistic stenosed carotid bifurcation geometry was reconstructed from the medical imaging. The results indicated that the numerical simulation of the realistic computational domain was performed and validated against the experimental measurements.

Because of the difficulty of determining critical flow conditions in experiments, the phenomenon of blood flow is not well understood. On the other hand, numerical studies of blood flow through the stenosed artery can easily lead to a better understanding of the mechanism involving the flow of blood in a stenotic region.

2.3 Numerical Studies of Blood Flow

Over the last two decades, a number of numerical studies of blood flow have been proposed to study the behaviour of blood flow through stenosed arteries. For more understanding of the critical blood flow in a stenotic region, realistic boundary and initial conditions were used to study the flow of blood by using unrealistic or realistic geometry of human blood vessels.

2.3.1 The Numerical Studies using an Artificial Geometry

Due to the difficulty of constructing realistic geometry, unrealistic domains such as a straight tube and curved tube were used to study the behavior of the flow [3, 6, 25, 35, 36, 41, 46, 47, 51, 56, 66, 68, 76, 80].

In 1996, Tu and Deville [78] studied the phenomena of blood flow in rigid circular straight tubes with 25% and 75% stenosis. Blood was assumed to be an incompressible fluid in four cases: Newtonian fluid, Bingham fluid, Herschel-Bulkley and power-law fluid. Hemodynamic simulations were performed by solving the Navier-Stokes equations. The results showed that the stenotic flow of the non-Newtonian model recovered to its undisturbed state slower than the Newtonian model. Ishikawa et al. (1998, [34]) studied the effect of non-Newtonian blood flow in a stenosed straight tube under pulsatile conditions. Blood was assumed to be a homogeneous and incompressible fluid. They concluded that the non-Newtonian flow was more stable than Newtonian flow and the non-Newtonian property had a considerable influence on blood flow. Shalman et al. (2002, [65]) presented a numerical model of the flow in a stenosed coronary artery. The domain of this study was a rigid circular straight tube 4 mm in diameter. The motion of blood flow was governed by the Navier-Stokes equations. The hemodynamically based parameters, the fractional flow reserve (FFR), coronary flow reserve (CFR) and relative coronary flow velocity reserve (CVR) were investigated by using the finite element method based on the FLUENT package. The results showed that FFR and CFR were useful parameters in the clinical assessment. Chen and Lu (2004, [18]) presented the non-Newtonian properties of blood in a bifurcation tube with a non-planar branch. The finite element method was used to solve the Navier-Stokes equations with the shear thinning behavior of the Carreau-Yasuda model. The wall shear stress and blood flow phenomena were investigated in the bifurcation model. They concluded that the non-Newtonian properties of blood and the non-planarity of blood vessels were an important factor in the numerical simulation of blood flow and might play a significant role in vascular biology and pathophysiology. In 2006, Chen and Lu [19] studied the pulsatile blood flow in a non-planar branch of a bifurcation model by using a numerical simulation model. The influences

of the non-Newtonian properties of blood and the out-of-plane curvature in the daughter vessel on the wall shear stress, oscillatory shear index and phenomena of blood flow were investigated during the pulse cycle. The results showed that the pulsatile properties advocated the view that the non-Newtonian properties of blood and the non-planarity of vessels were an important factor and played a significant part in vascular biology and pathophysiology. In 2008, Wiwatanapataphee [89] developed a mathematical model to simulate the pulsatile blood flow through a stenosed curved tube with arterial wall deformation. The motion of blood flow in the lumen region was governed by the Navier-Stokes equations and the continuity equation while the Brinkman equation was used to describe the flow through poroelastic wall. The computational domains were constructed in four different types: a normal tube and 25%, 50%, and 75% stenosed tubes. The influences of the different stenosis degrees on the flow and the wall shear stresses were investigated. The results indicated that blood pressure dropped dramatically at the stenosis region and jet-flow occurred at the stenosis site. Furthermore, the higher degree of stenosis gave a higher drop in the pressure, higher blood speed and higher wall shear stress around the stenosis site. Siddiqui et al. (2009, [67]) studied the effects of pulsatile non-Newtonian blood flow through a stenosed artery using a straight tube with a stenosis. They found that when the yield stress increased, the mean and steady flow rates decreased. In 2010, Mustapha et al. [50] presented a mathematical model to study the characteristics of blood flow through straight tubes with multi-cosine and multi-irregular stenoses. The unsteady flow of blood was governed by the Navier-Stokes equations and continuity equation. The finite difference method was used to solve the governing equations numerically. The results showed that the excess pressure dropped more across the cosine stenoses than the irregular ones. In 2010, Chaniotis et al. [17]) presented a computational study of blood flow in two prototype vessel geometries of coronary segments, curved pipes with different curvatures and bifurcated pipes with different branching angles and flow division. Wall shear stress (WSS) was investigated by using the finite volume method. The results indicated that low WSS was found at the region after the bifurcation and at the outer-entry and inner-exit flow regions of the curved

pipe.

2.3.2 The Numerical Studies using a Realistic Geometry

The simulation of blood flow using artificial geometries may give inaccurate and unusable results for clinical diagnosis. Thus, for better information about blood flow behavior, realistic domains were used for studying the blood flow problem. [15, 23, 30, 32, 38, 39, 49, 57, 69, 74, 85].

In 2002, Berthier et al.[11] studied the patterns of blood flow in three different realistic coronary arteries. The results showed that the pressures, velocity profiles and wall shear rates were greatly affected by the geometrical modifications. They recommended that geometries such as straight and curved tubes should be avoided because they give results far from the reality. Boutsianis et al. (2004, [14]) studied the computational simulation of intracoronary blood flow in the realistic coronary system to verify the validity of numerical prediction. The computational domain was constructed from high resolution computerized tomography (CT) scans of fresh pig heart. The transient momentum and mass conservation equations were numerically solved by applying computational fluid dynamics. The static pressure drop, velocity profiles, wall shear stress, intracoronary flow stream lines and bifurcation mass flow ratios were investigated. They concluded that the realistic simulation could help in accurate surgical planning. Sadeghian et al. (2007, [58]) presented the numerical blood flow analysis in a realistic model of the human coronary artery. The continuity equation and Navier-Stokes equations were solved by FLUENT software to describe the fluid flow. They concluded that the Newtonian model was sufficient to analyse the wall shear stress on vessels but for more more validity the non-Newtonian model should be considered. In 2009, Yin et al. [93] developed a physiologically three-dimensional computational fluid dynamics (CFD) model of the realistic left coronary artery to estimate shear stress. They then used the computed shear stress in the stimulation of vascular endothelial cells in vitro. The effects of different stenosis including 0%, 30%, 60% and 80% were investigated. A K-omega turbulence model was used to solve the blood flow velocity and shear stress. They concluded that the combination of CFD and in vitro

studies provided an efficient way for investigating the blood flow mechanism. In 2010, Wellnhofer et al. [86] studied the impact of side-branches on local wall WSS in the simulation of blood flow through the right coronary artery (RCA) trees. Seventeen computational domains of RCA were reconstructed and studied. From the results, the side-branches had a significant impact on blood flow profile and WSS in RCA. They concluded that the side-branches might not be neglected in the numerical simulation of blood flow. Chuchard et al. (2011, [24]) studied the behavior of blood flow through the system of coronary arteries with stenosis of left anterior descending by using a realistic computational geometry. Their simulation results showed a high speed of blood flow and high pressure drop in the stenosis area. Wiwatanapataphee et al. (2012, [90]) studied the effect of branching on blood flow in the system of coronary arteries using the pulsatile flow condition on the boundary and a realistic geometry of human coronary arteries. The results indicated that blood pressure in the coronary system with branching vessels was lower than the one in the coronary system with no branch, and the wall shear stress at bifurcation was higher than at a nearby region.

2.4 Numerical Studies of Blood Flow in a Stenosed Artery with a Bypass Graft

Over the last two decades, a large number of bypass grafts have been implanted worldwide. However, after surgery, up to 25% of grafts fail within one year and up to 50% fail within ten years [53]. Today, it has been recognized that some of the most important factors in a successful bypass operation is the information about the rheological behavior of blood, the pressure distribution, the flow speed, the wall shear stress and the wall deformation in the cardiac cycles [94]. Thus, some research has been carried out to study the blood flow behavior in the stenosed coronary artery with a graft by using unrealistic and realistic geometries.

2.4.1 The Numerical Studies using an Artificial Geometry

Due to the complexity of the structure of a real stenosed blood vessel with a graft, unrealistic geometries were constructed and used to study the blood flow behavior [9, 10, 82, 61, 88].

In 2000, Bertolotti and Deplano [12] studied the patterns of blood flow at the anastomosis of a stenosed coronary bypass. The simulation of blood flow was performed in the stenosed straight tube with a graft by using a finite element method. They concluded that the distance of the anastomosis from the stenosis site was an important factor for the coronary artery bypass graft surgery. Poltem et al. (2006, [55]) studied the behavior of pulsatile blood flow in a stenosed coronary artery with a graft. They used realistic boundary conditions whilst the domain was unreal. The influence of different angles of a graft on the flow pattern was investigated in a domain having 75% stenosis. The results showed that the domain having a 45 degree graft angle performed better than the ones with 60 and 90 degrees. The pressure of blood in the stenosed artery dropped rapidly in the stenosis region and the high shear stress on wall occurred around the stenosis site. Chen et al. (2006, [20]) investigated the effects of non-Newtonian blood flow in a 75% stenosed straight tube with a bypass graft. The different flow rates and different positions of the bypass graft relative to the stenosis are studied. The results of this study supported the view that the residual flow from the stenosed vessel interacted with the flow from the graft and supported the velocity and wall shear stress distribution near the joint. The non-Newtonian property of blood was a key factor in the simulation of blood flow in the artery with bypass grafts. Vimmr and Jonasova (2010, [83]) studied the effect of non-Newtonian blood flow in a blocked tube with a bypass graft. The numerical simulations of the flow were operated by using incompressible Navier-Stokes equations and solved by the pseudo-compressibility approach. The velocity profile and wall shear stress were investigated in the proximal and distal artery and the connected end-to-side bypass graft. They concluded that the non-Newtonian model had significance on the distribution of wall shear stress.

2.4.2 The Numerical Studies using a Realistic Geometry

For the clinical diagnosis, a realistic domain was used to simulate and study the characteristic of blood flow [29, 84]. However, there is not much research on blood flow using realistic geometry of stenosed artery with a graft because of the difficulty of geometry construction and the limitation of computer in blood flow simulation.

In 2009, Nipawan et al.[52] studied the effect of a bypass graft on the flow of blood in a stenosed right coronary artery (RCA). The computed tomography (CT) images were used to reconstruct the computational domain. The distribution of velocity and wall shear stress were investigated. The numerical results showed that the bypass grafting can improve blood flow in the far distal part of the stenosed RCA. Sankaran et al. (2012, [60]) presented a computational design for multiscale modeling and blood flow simulation in a coronary artery bypass graft (CABG) patient. Different graft angles and shapes were investigated. They concluded that the shape of bypass graft had a strong influence on wall shear stress and all shear stress gradients. The 70 degrees graft angle was the best choice for their patient.

2.5 Concluding Remarks

Much research has been carried out to study the complex behavior of blood flow in a stenosed coronary artery with no graft and with a bypass. However, almost computational domains used in those works should not be used in a medical diagnosis for the patient because the domains are not completed realistic domains, such as a straight pipe, curved pipe, bifurcated pipe and realistic geometry of stenosed single vessel with no branches. In this work, we construct the realistic system of human coronary arteries with no graft and with a bypass graft to study the behavior of blood flow, and look at the effect of branching and bypass graft by using mathematical modeling and numerical methods. The computational domain used in this thesis consists of the ascending aorta, the arch of aorta, the proximal left coronary artery, the right coronary artery (RCA) with branches, and a graft.

CHAPTER III

GEOMETRY CONSTRUCTION

3.1 General Overview

In this thesis, we construct the realistic three-dimensional computational domain of the coronary artery system consisting of the ascending aorta, the arch of aorta, the proximal LCA, the RCA with stenosis region, and a graft. Eight domains are constructed to investigate the behavior of blood flow. The four different degrees of RCA stenosis including 0%, 40%, 63%, and 72% are used to investigate the effect of the stenosis degree. Four models having 0%, 40%, 63%, and 72% RCA stenosis with a graft are used to study the effect of bypass grafting. The motion of blood flow is simulated by using the COMSOL multiphysics package. The construction of a three-dimensional domain using Mimics software is presented in section 3.2.

3.2 Geometry Construction using Mimics Software

To construct the domain of the three-dimensional coronary artery system, we use information based on over 300 computed tomography (CT) data files which are contributed by Thanongchai Siriapisith, a medical doctor of Siriraj hospital, Bangkok, Thailand. In this thesis, CT scan data files are converted to stereo-lithography (STL) format and saved in a file by Mimics software version 10.01.

To construct the domain of the coronary artery system by using Mimics software, the user should understand the structure of the system of coronary arteries very well. The constructing method is shown in the following subsections.

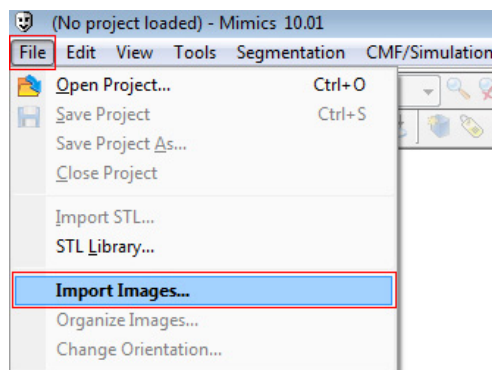
3.2.1 Importing CT Data Files

The first step of domain construction is importing and converting CT data files to a mimics file (*.mcs). The process is shown as follows.

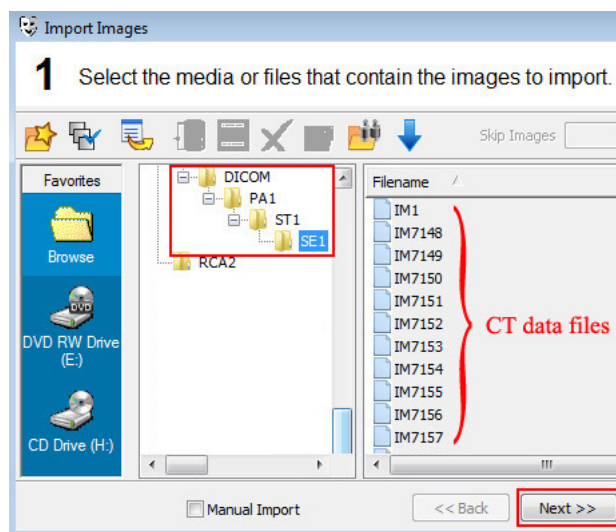
- Open Mimic software by double clicking on Mimic icon.



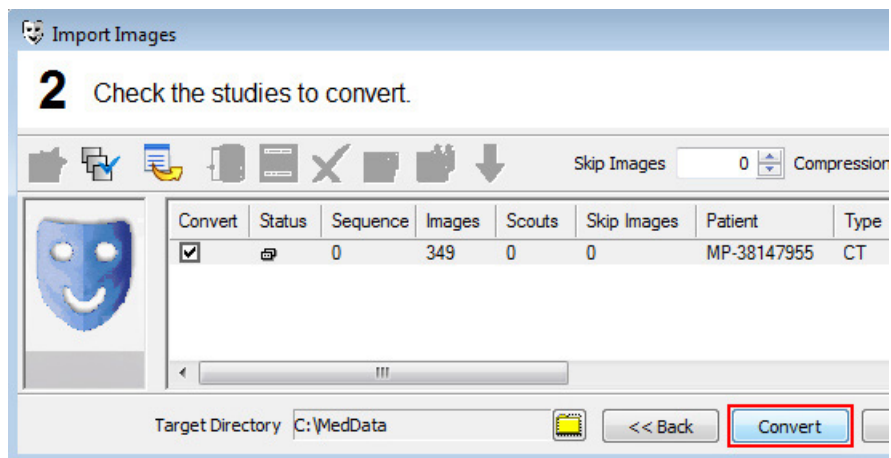
- Import CT Data files by clicking on “File\Import Images...”.



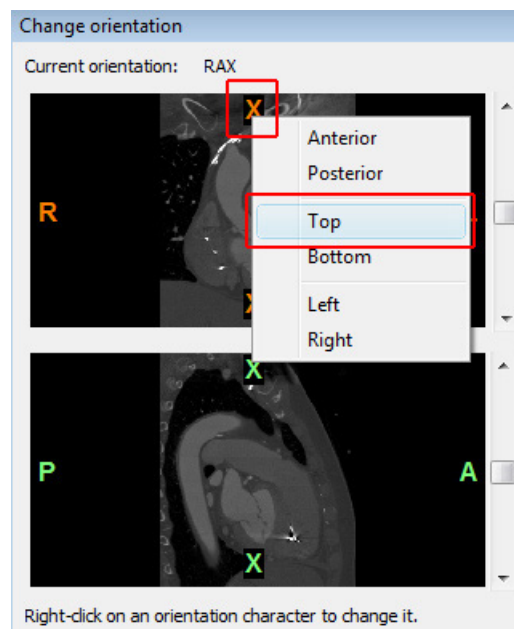
- Click on a folder containing CT data files to select all files in that folder and then click “Next >>” button. In this work, the CT data files are contained in the folder “SE1”.



- Click “Convert” button to convert the files to a Mimics file.



- Before start working in Mimics work space, the orientation of the domain must be specified. Right-click on the orientation character “X” (in the picture) to change it to “Top” and then click the “OK” button.

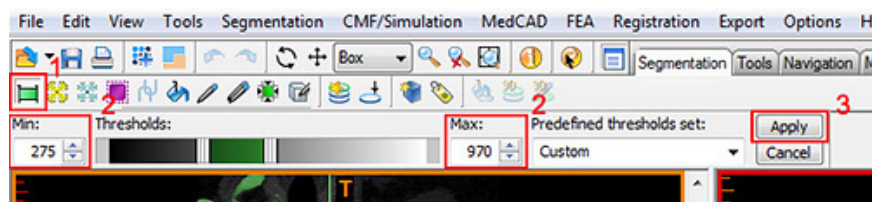


In the next step, the user must use the understanding of coronary artery system structure to specify the region of the domain.

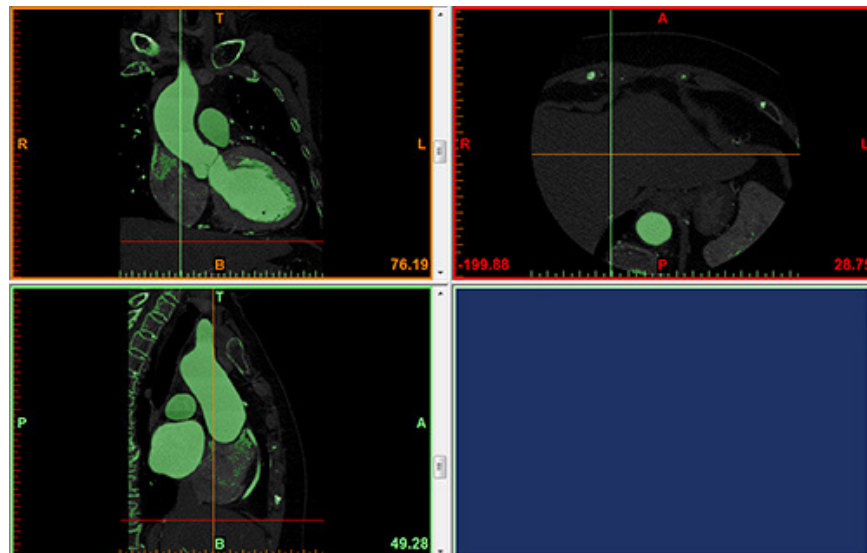
3.2.2 Specifying a Region of the Domain

This process will help us to automatically specify the domain by choosing a range of domain density.

- Click the “Segmentation\Thresholding” or “thresholding” button, specify Min/Max values and then click the “Apply” button. In this case, we choose Min/Max values of about 275/970.

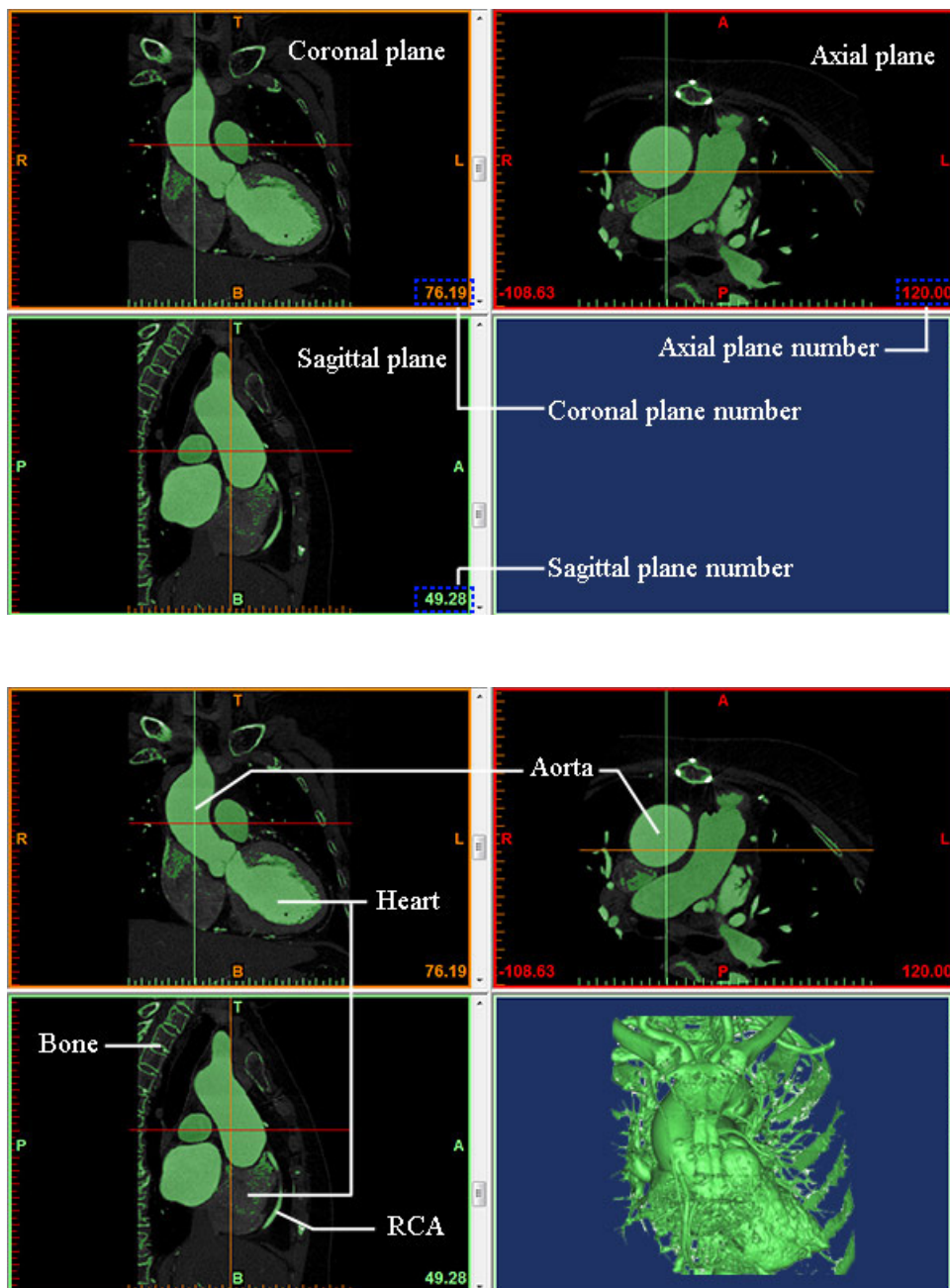


- The domain which is colored by the above process is in the green area.



However, the domain from this process cannot be used for simulation because there are not only the coronary arteries and a graft but also heart, bone, tissue, and other blood vessels. Thus, we need to separate it manually.

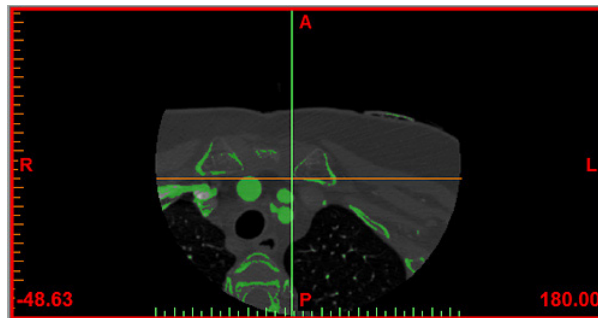
Before we extract and construct the three-dimensional domain, the work space of Mimic software consisting of four separate windows is described. The window with orange edge, red edge, and green edge show the domain in the coronal plane, axial plane, and sagittal plane, respectively. The blue window shows the 3-D domain obtained from the constructing process.



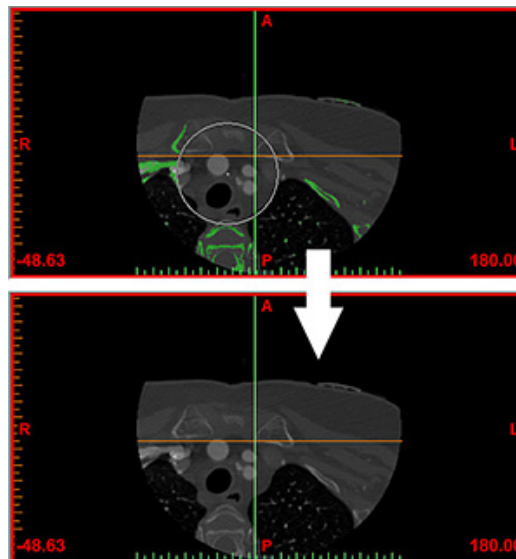
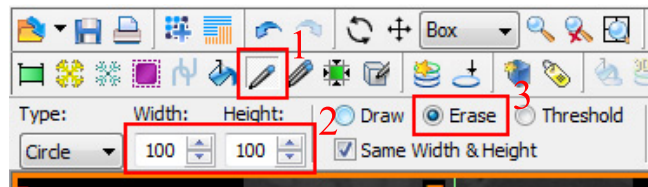
3.2.3 Extracting and Constructing the 3-D Domain

This process shows the method of extracting the three-dimension domain by using the “Edit Masks” button, and then the constructing of the domain.

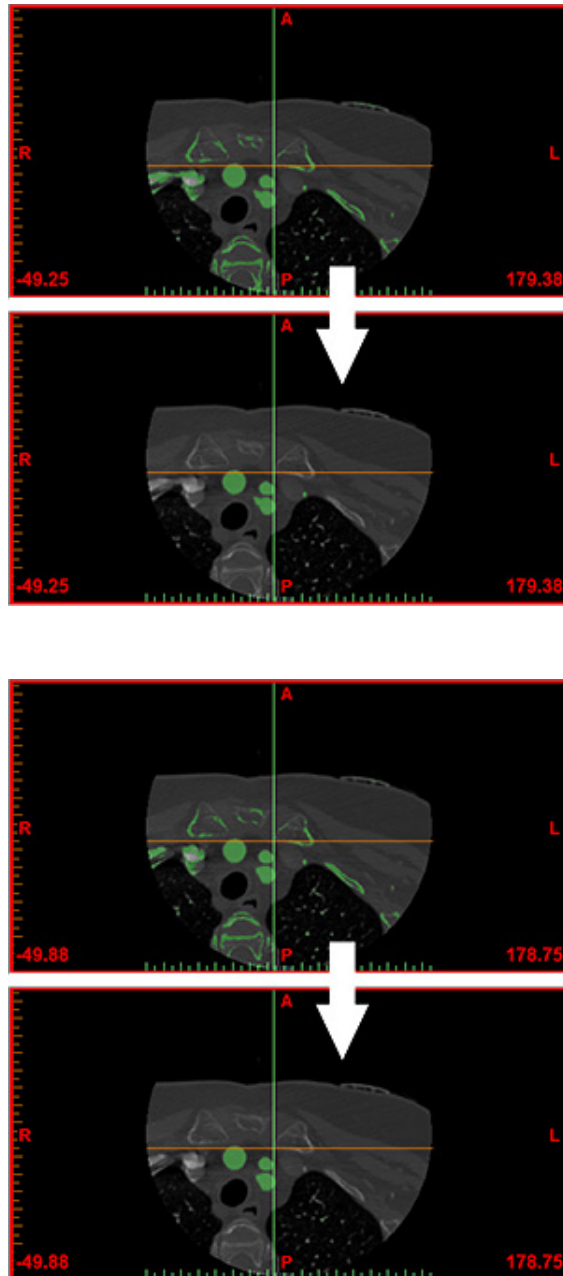
- The axial-plane number is chosen to specify the upper limit of the domain. In this case, we choose an axial-plane number of 180.00.



- Select the “Edit Masks” button, specify the radius of brush, choose “Erase” and then erase all the area in the axial plane.

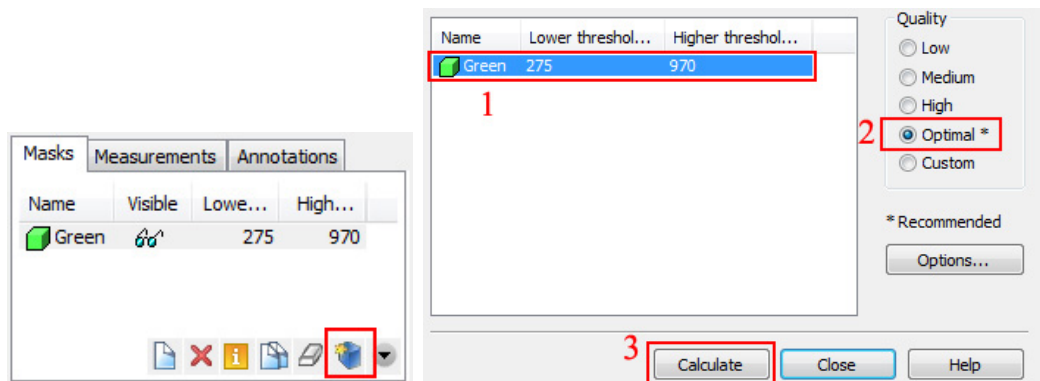


- In the axial plane, scroll down to the plane numbers 179.38, 178.75, ..., and erase the areas which are not used for constructing the domain.



- Repeat the above step until we obtain the complete domain.

- To construct the three-dimensional domain, click the “Calculate 3D from Mask” button in the “Masks” tab. Choose the green domain, choose “Optimal” in the Quality box, and then click calculate.



The three-dimensional domain of the coronary artery system is then generated as shown in Figure 3.1.



Figure 3.1: The three-dimensional domain of the coronary artery system with bypass grafts.

CHAPTER IV

MATHEMATICAL MODEL

4.1 General Overview

Over the last two decades, many studies have been proposed to describe the phenomena of blood flow involved in the treatment of coronary artery disease. The mathematical model and numerical technique with the computational domain of real/unreal structure are used to investigate the blood flow behavior. However, for medical diagnosis, a realistic domain should provide more reliable results.

The continuity equation and Navier-Stokes equations are used to govern the motion of blood flow. Blood is assumed to be an incompressible non-Newtonian fluid. The equations are solved by using a finite element method based on the COMSOL Multiphysics package.

In this chapter, the mathematical model and the computational domains are presented. Firstly, the geometry of the computational domain is shown in section 3.2. The governing equations and boundary conditions are presented in sections 3.3. and 3.4.

4.2 Geometrical Description

The computational domains are firstly constructed from computed tomography (CT) scan images by using Mimics software. The real system of coronary arteries is shown in Figure 4.1.

In this thesis, we choose the system of coronary arteries with a graft number 1 (in Figure 4.1) to study the effect of a bypass grafting. However, the domains created from the Mimics program are impractical for computational fluid dynamics, because of their complexity and rough surface. A cubic B-spline inter-

polation is used to smooth the surface. The computational domain used in this study is shown in Figure 4.2.

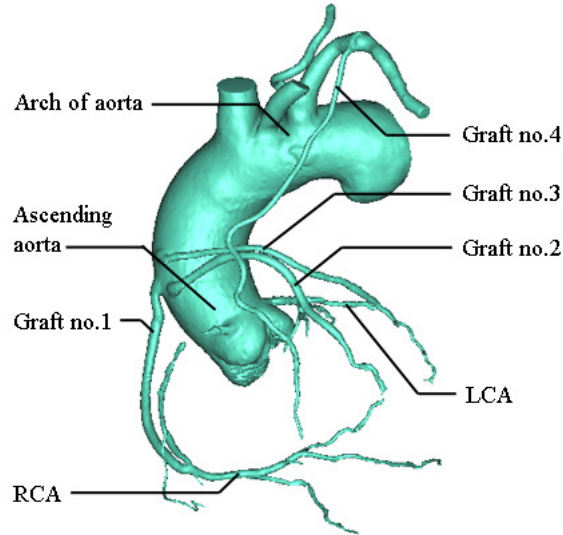


Figure 4.1: The system of coronary arteries with four bypass grafts constructed from Mimics software.

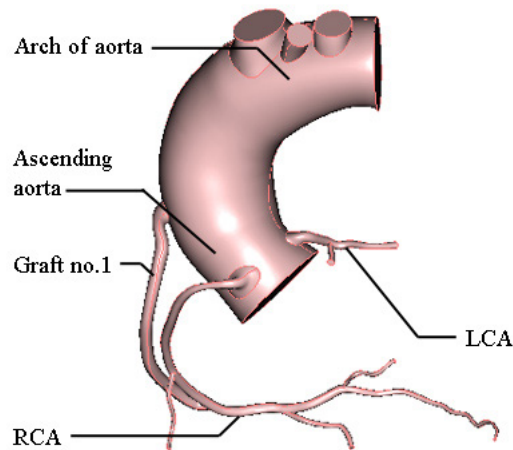


Figure 4.2: Three-dimensional computational domain of the coronary artery system with a bypass graft.

Eight computational domains are used to study the blood flow problem. Four domains of different RCA stenosis with no graft and four domains of different RCA stenosis with a bypass graft are shown in Figure 4.3. Figure 4.4 presents the computational domain with inflow and outflow surfaces. The properties of the domain used in this study are given in Table 4.1.

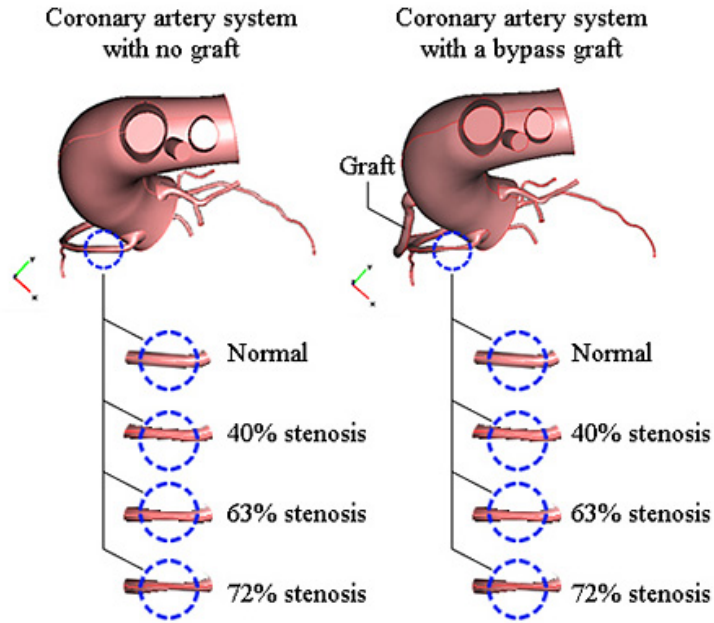


Figure 4.3: The computational domains of the coronary artery system with no graft and with a bypass graft having four different degrees of stenosed RCA including 0% (normal), 40%, 63% and 72%.

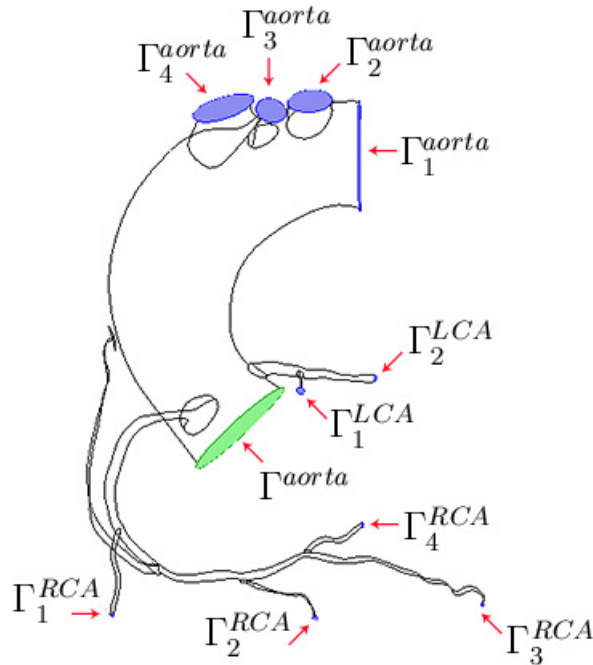


Figure 4.4: The domain with inflow surface Γ^{aorta} and ten outflow surfaces Γ_1^{aorta} , Γ_2^{aorta} , Γ_3^{aorta} , Γ_4^{aorta} , Γ_1^{RCA} , Γ_2^{RCA} , Γ_3^{RCA} , Γ_4^{RCA} , Γ_1^{LCA} and Γ_2^{LCA} .

Table 4.1: The properties of the computational domain.

	Volume	Surface area	Perimeter	Length
	cm ³	cm ³	cm ²	cm ²
The domain with no graft	82.774	—	—	—
The domain with a bypass graft	83.765	—	—	—
Graft	0.991	10.013	—	8.101
Main RCA	—	—	—	18.699
Γ^{aorta}	—	6.882	9.318	—
Γ_1^{aorta}	—	6.025	8.708	—
Γ_2^{aorta}	—	0.978	3.510	—
Γ_3^{aorta}	—	0.439	2.531	—
Γ_4^{aorta}	—	1.857	4.836	—
Γ_1^{RCA}	—	0.008	0.310	—
Γ_2^{RCA}	—	0.020	0.506	—
Γ_3^{RCA}	—	0.006	0.270	—
Γ_4^{RCA}	—	0.013	0.412	—
Γ_1^{LCA}	—	0.029	0.606	—
Γ_2^{LCA}	—	0.029	0.607	—

4.3 Governing Equations

In this study, we assume that blood is an incompressible non-Newtonian fluid. The motion of blood flow is governed by the continuity equation (4.1) and Navier-Stokes equations (4.2):

$$\nabla \cdot \mathbf{u} = 0, \tag{4.1}$$

$$\rho \left[\frac{\partial \mathbf{u}}{\partial t} + (\mathbf{u} \cdot \nabla) \mathbf{u} \right] = \nabla \cdot \sigma, \tag{4.2}$$

where $\mathbf{u} = (u_1, u_2, u_3)^T$ is the blood velocity vector in the lumen region, $\rho = 1.06$ g/cm³ is density of blood and σ is the total stress tensor which is defined by

$$\sigma = -pI + 2\eta(\dot{\gamma})\mathbf{D}, \tag{4.3}$$

where here p is the blood pressure, I denotes a 3×3 identity matrix, η is the viscosity of blood, $\dot{\gamma}$ is the shear rate and \mathbf{D} is the rate of deformation tensor defined by

$$\mathbf{D} = \frac{1}{2}(\nabla \mathbf{u} + (\nabla \mathbf{u})^T). \quad (4.4)$$

For the Newtonian model, the viscosity of blood is assumed to be a constant $\eta = 0.0345$ dyne/(cm² s) [83]. For the non-Newtonian model, we assume that the viscosity of blood is a function of shear rate ($\dot{\gamma}$) based on Carreau's shear-thinning model [19]:

$$\eta(\dot{\gamma}) = \eta_\infty + (\eta_0 - \eta_\infty) [1 + (\lambda \dot{\gamma})^2]^{(n-1)/2}, \quad (4.5)$$

where η_0 , η_∞ , λ , and n are parameters which are shown in Table 4.2 [22] and the shear rate $\dot{\gamma}$ is defined by

$$\dot{\gamma} = \sqrt{2tr[\frac{1}{2}(\nabla \mathbf{u} + (\nabla \mathbf{u})^T)]^2}. \quad (4.6)$$

Table 4.2: The parameter values used in Carreau's shear-thinning model.

Parameter	Symbol	Value	Unit
Zero shear viscosity	η_0	0.56	g cm ⁻¹ s ⁻¹
Infinite shear viscosity	η_∞	0.0345	g cm ⁻¹ s ⁻¹
Time constant	λ	3.313	s
Consistency index	n	0.3568	—

From equations (4.1)-(4.4), the governing equations of blood flow can be written in Einstein notation as follows:

$$\frac{\partial u_j}{\partial x_j} = 0, \quad (4.7)$$

$$\rho \left(\frac{\partial u_i}{\partial t} + u_j \frac{\partial u_i}{\partial x_j} \right) = -\frac{\partial p}{\partial x_i} + \eta \left[\frac{\partial}{\partial x_j} \left(\frac{\partial u_i}{\partial x_j} + \frac{\partial u_j}{\partial x_i} \right) \right], \quad (4.8)$$

where index j denotes the summation notation $a_j = \sum_{j=1}^3 a_j$ and index i denotes the vector component b_i of $\mathbf{b} = (b_1, b_2, b_3)^T$ for $i = 1, 2, 3$.

4.4 Boundary Equations

For the solution of the velocity field and pressure in the computational domain as shown in Figure 4.4, the pulsatile pressure and flow rate are specified. In this study, we set the behavior of blood flow as the pulsatile conditions with no difference in time variation of the cardiac cycle. Therefore, the pulsatile pressure and flow rate can be expressed by the periodic function $p(t) = p(t + kT)$ and $Q(t) = Q(t + kT)$ for $k = 0, 1, 2, \dots$ and the cardiac period T is 0.8 s. Mathematically, the pulsatile pressure $p(t)$ and the flow rate can be expressed by the following truncated Fourier series [88]:

$$p(t) = \bar{p} + \sum_{k=1}^4 \alpha_k^p \cos(k\omega t) + \beta_k^p \sin(k\omega t), \quad (4.9)$$

$$Q(t) = \bar{Q} + \sum_{k=1}^4 \alpha_k^Q \cos(k\omega t) + \beta_k^Q \sin(k\omega t), \quad (4.10)$$

where \bar{p} is the mean pressure, \bar{Q} is the mean flow rate, and $\omega = \frac{2\pi}{T}$ is an angular frequency with period T . The values of \bar{p} , \bar{Q} , α_k^Q , β_k^Q , α_k^p , and β_k^p are shown in Table 4.3.

On the inlet surface of aorta Γ^{aorta} , we set the pulsatile velocity:

$$\mathbf{u}_{in}(t) = \frac{Q(t)}{A}, \quad (4.11)$$

where $A = 6.88 \text{ cm}^2$ is the cross-sectional area of the inlet boundary. On the outlet surfaces including Γ_1^{aorta} , Γ_2^{aorta} , Γ_3^{aorta} , Γ_4^{aorta} , Γ_1^{RCA} , Γ_2^{RCA} , Γ_3^{RCA} , Γ_4^{RCA} , Γ_1^{LCA} , and Γ_2^{LCA} , we impose the corresponding pulsatile pressure conditions:

$$p = p_0(t), \quad \eta(\nabla \mathbf{u} + (\nabla \mathbf{u})^T) \cdot \mathbf{n} = 0, \quad (4.12)$$

where \mathbf{n} is the unit normal vector at the boundary. The no-slip condition is applied to the wall of the coronary artery system:

$$\mathbf{u} = 0. \quad (4.13)$$

In summary, the blood flow in the system of coronary arteries is governed by the following boundary value problem (BVP).

BVP: Find \mathbf{u} and p such that equations (4.7), (4.8), and all boundary conditions are satisfied.

Table 4.3: Values of the parameters \bar{p} , \bar{Q} , α_k^Q , β_k^Q , α_k^p and β_k^p .

Vessel	k	α_k^Q	β_k^Q	α_k^p	β_k^p
Aorta	1	1.7048	-7.5836	8.1269	-12.4156
$\bar{Q} = 5.7222$	2	-6.7035	-2.1714	-6.1510	-1.1072
$\bar{p} = 97.2222$	3	-2.6389	2.6462	-1.333	-0.3849
$A = 6.87976$	4	0.7198	0.2687	-2.9473	1.1603
LCA	1	0.1007	0.0764	-3.3107	-2.2932
$\bar{Q} = 0.1589$	2	-0.0034	-0.0092	-9.8639	8.0487
$\bar{p} = 65.9722$	3	0.0294	0.0337	3.0278	3.8009
	4	0.0195	-0.0129	2.2476	-3.2564
RCA	1	0.0393	0.0241	5.9369	3.6334
$\bar{Q} = 0.0896$	2	-0.0360	0.0342	-11.199	2.1255
$\bar{p} = 65.3333$	3	-0.0131	0.0026	-2.2778	-3.7528
	4	-0.0035	-0.0041	2.7333	-0.6375

CHAPTER V

FINITE ELEMENT FORMULATION

5.1 General Overview

The finite element method (FEM) is a numerical technique used to find approximated solutions of partial differential equations and integral equations. A real object is divided into a large number of small finite elements such as cubes or tetrahedral elements. The governing equations in section 4.3 are used to describe the behavior of complex phenomena in each element. The numerical solution is earned out using the COMSOL multiphysics package.

Section 5.2 shows the derivation of the finite element formulation based on the Bubnov-Galerkin finite element method. The numerical implementation of the FEM is demonstrated in section 5.3. In section 5.4, the numerical algorithm for the solutions are presented. Finally, we give a convergence analysis of the mesh sensitivity in section 5.5.

5.2 Finite Element Formulation

The finite element technique based on the weak formulation of the governing equations is shown in this section. Beginning with the total weighted residual method to the system of equations (4.7) and (4.8), we then get the variational statement corresponding to the boundary value problem.

Find u_i for $i = 1, 2, 3$ and $p \in H^1(\Omega)$ such that for all w^i for $i = 1, 2, 3$ and $w^p \in H_0^1(\Omega)$, all boundary conditions are satisfied and

$$\int_{\Omega} w^p \frac{\partial u_j}{\partial x_j} d\Omega = 0,$$

$$\begin{aligned} & \rho \int_{\Omega} w^i \frac{\partial u_i}{\partial t} d\Omega + \rho \int_{\Omega} w^i (u_j \frac{\partial u_i}{\partial x_j}) d\Omega + \int_{\Omega} w^i \frac{\partial p}{\partial x_i} d\Omega \\ & - \int_{\Omega} w^i \eta [\frac{\partial}{\partial x_j} (\frac{\partial u_i}{\partial x_j} + \frac{\partial u_j}{\partial x_i})] d\Omega = 0, \end{aligned} \quad (5.1)$$

where

$$\begin{aligned} H^1(\Omega) &= \{v \in L^2(\Omega) \mid \frac{\partial v}{\partial x_i} \in L^2(\Omega)\} \text{ is the Sobolev space } W^{1,2}(\Omega), \\ H_0^1(\Omega) &= \{v \in H^1(\Omega) \mid v = 0 \text{ on the Dirichlet type boundary}\}, \end{aligned}$$

with norm $\|\cdot\|_{1,2,\Omega}$, and $L^2(\Omega)$ is the space of integrable functions.

By using Green's formula on the Navier-Stokes equations, we have

$$\begin{aligned} & \int_{\Omega} w^p \frac{\partial u_j}{\partial x_j} d\Omega = 0, \\ & \rho \int_{\Omega} w^i \frac{\partial u_i}{\partial t} d\Omega + \rho \int_{\Omega} w^i (u_j \frac{\partial u_i}{\partial x_j}) d\Omega + \int_{\Gamma} w^i p d\Gamma - \int_{\Omega} \frac{\partial w^i}{\partial x_i} p d\Omega \\ & - \int_{\Gamma} \eta w^i (\frac{\partial u_i}{\partial x_j} + \frac{\partial u_j}{\partial x_i}) d\Gamma + \int_{\Omega} \eta \frac{\partial w^i}{\partial x_j} (\frac{\partial u_i}{\partial x_j} + \frac{\partial u_j}{\partial x_i}) d\Omega = 0. \end{aligned} \quad (5.2)$$

By applying the boundary conditions in section 4.4 and w^i based on the Dirichlet type boundary condition, we then obtain the following system of equations:

$$\begin{aligned} & \int_{\Omega} w^p \frac{\partial u_j}{\partial x_j} d\Omega = 0, \\ & \rho \int_{\Omega} w^i \frac{\partial u_i}{\partial t} d\Omega + \rho \int_{\Omega} w^i (u_j \frac{\partial u_i}{\partial x_j}) d\Omega - \int_{\Omega} \frac{\partial w^i}{\partial x_i} p d\Omega \\ & + \int_{\Omega} \eta \frac{\partial w^i}{\partial x_j} \frac{\partial u_i}{\partial x_j} d\Omega + \int_{\Omega} \eta \frac{\partial w^i}{\partial x_j} \frac{\partial u_j}{\partial x_i} d\Omega = 0. \end{aligned} \quad (5.3)$$

To find the Galerkin finite element approximation, we choose K -dimensional subspace H_K of $H^1(\Omega)$ with the basis functions $\{\phi_i\}_{i=1}^K$ for u_i and w^i , and

L -dimensional subspace H_L of $H^1(\Omega)$ with the basis functions $\{\psi_i\}_{i=1}^L$ for p and w^p . We then have

$$\begin{aligned} u_i(x, t) &\approx (u_i)_K = \sum_{\alpha=1}^K \phi_\alpha(x) u_{i\alpha}(t), \\ w^i &\approx (w^i)_K = \sum_{\beta=1}^K \phi_\beta(x) w_\beta^i(t), \\ p(x, t) &\approx (p)_L = \sum_{\gamma=1}^L \psi_\gamma(x) p_\gamma(t), \\ w^p &\approx (w^p)_L = \sum_{\delta=1}^L \psi_\delta(x) w_\delta^p(t). \end{aligned} \tag{5.4}$$

By substituting u_i , w^i , p , and w^p from equations (5.4) into the system of equations (5.3) and considering the values of w^i and w^p to be arbitrary, we obtain

$$\begin{aligned} &\sum_{\delta=1}^L \sum_{\alpha=1}^K [(\psi_\delta, \frac{\partial \phi_\alpha}{\partial x_j}) u_{j\alpha}] = 0, \\ &\sum_{\beta=1}^K \sum_{\alpha=1}^K [\rho(\phi_\beta, \phi_\alpha) \dot{u}_{i\alpha}] + \sum_{\beta=1}^K \sum_{\alpha=1}^K [\rho(\phi_\beta, u_j \frac{\partial \phi_\alpha}{\partial x_j}) u_{i\alpha}] - \sum_{\beta=1}^K \sum_{\gamma=1}^L [(\frac{\partial \phi_\beta}{\partial x_i}, \psi_\gamma) p_\gamma] \\ &+ \sum_{\beta=1}^K \sum_{\alpha=1}^K [(\frac{\partial \phi_\beta}{\partial x_j}, \eta \frac{\partial \phi_\alpha}{\partial x_j}) u_{i\alpha}] + \sum_{\beta=1}^K \sum_{\alpha=1}^K [(\frac{\partial \phi_\beta}{\partial x_j}, \eta \frac{\partial \phi_\alpha}{\partial x_i}) u_{j\alpha}] = 0, \end{aligned} \tag{5.5}$$

where (\cdot, \cdot) denotes the inner product defined by $(u, v) = \int_\Omega u \cdot v \, d\Omega$.

The system of equations (5.5) can be rewritten as follows:

$$\begin{aligned} &\sum_{\delta=1}^L \sum_{\alpha=1}^K [(\psi_\delta, \frac{\partial \phi_\alpha}{\partial x_1}) u_{1\alpha} + (\psi_\delta, \frac{\partial \phi_\alpha}{\partial x_2}) u_{2\alpha} + (\psi_\delta, \frac{\partial \phi_\alpha}{\partial x_3}) u_{3\alpha}] = 0, \\ &\sum_{\beta=1}^K \sum_{\alpha=1}^K [\rho(\phi_\beta, \phi_\alpha) \dot{u}_{i\alpha}] + \sum_{\beta=1}^K \sum_{\alpha=1}^K [\rho(\phi_\beta, u_1 \frac{\partial \phi_\alpha}{\partial x_1} + u_2 \frac{\partial \phi_\alpha}{\partial x_2} + u_3 \frac{\partial \phi_\alpha}{\partial x_3}) u_{i\alpha}] \\ &+ \sum_{\beta=1}^K \sum_{\alpha=1}^K [(\frac{\partial \phi_\beta}{\partial x_1}, \eta \frac{\partial \phi_\alpha}{\partial x_1}) u_{i\alpha} + (\frac{\partial \phi_\beta}{\partial x_2}, \eta \frac{\partial \phi_\alpha}{\partial x_2}) u_{i\alpha} + (\frac{\partial \phi_\beta}{\partial x_3}, \eta \frac{\partial \phi_\alpha}{\partial x_3}) u_{i\alpha}] \\ &+ \sum_{\beta=1}^K \sum_{\alpha=1}^K [(\frac{\partial \phi_\beta}{\partial x_1}, \eta \frac{\partial \phi_\alpha}{\partial x_i}) u_{1\alpha} + (\frac{\partial \phi_\beta}{\partial x_2}, \eta \frac{\partial \phi_\alpha}{\partial x_i}) u_{2\alpha} + (\frac{\partial \phi_\beta}{\partial x_3}, \eta \frac{\partial \phi_\alpha}{\partial x_i}) u_{3\alpha}] \end{aligned}$$

$$-\sum_{\beta=1}^K \sum_{\gamma=1}^L \left[\left(\frac{\partial \phi_\beta}{\partial x_i}, \psi_\gamma \right) p_\gamma \right] = 0 \quad \text{for } i = 1, 2, 3. \quad (5.6)$$

The system of equations (5.6) can be written in matrix form as

$$\begin{aligned} C^T \mathbf{U} &= \mathbf{0}, \\ M \dot{\mathbf{U}} + (A(u) + B) \mathbf{U} + \hat{C} \mathbf{P} &= \mathbf{0}, \end{aligned} \quad (5.7)$$

where \mathbf{U} , $\dot{\mathbf{U}}$ and \mathbf{P} are vectors representing the values of the corresponding unknowns at nodes of the finite element mesh:

$$\mathbf{U} = \begin{bmatrix} u_{1\alpha} \\ u_{2\alpha} \\ u_{3\alpha} \end{bmatrix}_{3K \times 1} \quad \text{with } u_{i\alpha} = (u_{i1}, u_{i2}, u_{i3}, \dots, u_{iK})^T,$$

$$\dot{\mathbf{U}} = \begin{bmatrix} \dot{u}_{1\alpha} \\ \dot{u}_{2\alpha} \\ \dot{u}_{3\alpha} \end{bmatrix}_{3K \times 1} \quad \text{with } \dot{u}_{i\alpha} = (\dot{u}_{i1}, \dot{u}_{i2}, \dot{u}_{i3}, \dots, \dot{u}_{iK})^T, \text{ and}$$

$$\mathbf{P} = [p_\gamma]_{L \times 1} \quad \text{with } p_\gamma = (p_1, p_2, p_3, \dots, p_L)^T. \quad (5.8)$$

The coefficient matrices and load vector are given by

$$M = \begin{bmatrix} m_{\beta\alpha} & 0 & 0 \\ 0 & m_{\beta\alpha} & 0 \\ 0 & 0 & m_{\beta\alpha} \end{bmatrix}_{3K \times 3K} \quad \text{with } m_{\beta\alpha} = (\phi_\beta, \rho \phi_\alpha),$$

$$A(u) = \begin{bmatrix} a(u)_{\beta\alpha} & 0 & 0 \\ 0 & a(u)_{\beta\alpha} & 0 \\ 0 & 0 & a(u)_{\beta\alpha} \end{bmatrix}_{3K \times 3K}$$

$$\text{with } a(u)_{\beta\alpha} = \left(\phi_\beta, \rho \left(u_1 \frac{\partial \phi_\alpha}{\partial x_1} + u_2 \frac{\partial \phi_\alpha}{\partial x_2} + u_3 \frac{\partial \phi_\alpha}{\partial x_3} \right) \right),$$

$$B = \begin{bmatrix} 2b_{11} + b_{22} + b_{33} & b_{12} & b_{13} \\ b_{21} & b_{11} + 2b_{22} + b_{33} & b_{23} \\ b_{31} & b_{32} & b_{11} + b_{22} + 2b_{33} \end{bmatrix}_{3K \times 3K}$$

$$\begin{aligned}
 &\text{with } b_{mn} = (b_{mn})_{\beta\alpha} = \left(\frac{\partial\phi_\beta}{\partial x_n}, \eta \frac{\partial\phi_\alpha}{\partial x_m} \right), \\
 &C = \begin{bmatrix} c_{\delta\alpha}^1 \\ c_{\delta\alpha}^2 \\ c_{\delta\alpha}^3 \end{bmatrix}_{3K \times L} \quad \text{with } c_{\delta\alpha}^i = \left(\psi_\delta, \frac{\partial\phi_\alpha}{\partial x_i} \right), \\
 &\hat{C} = \begin{bmatrix} c_{\beta\gamma}^1 \\ c_{\beta\gamma}^2 \\ c_{\beta\gamma}^3 \end{bmatrix}_{3K \times L} \quad \text{with } c_{\beta\gamma}^i = -\left(\frac{\partial\phi_\beta}{\partial x_i}, \psi_\gamma \right). \tag{5.9}
 \end{aligned}$$

5.3 Numerical Implementation

5.3.1 Three-Dimensional Tetrahedral Elements

The integrals in (5.9) are defined in terms of the coordinates (x_1, x_2, x_3) or (x, y, z) . The calculation of the coefficient matrices and load vectors for an element Ω is difficult if performed directly, because the limit of integration changes from element to element. For performing the convenient calculation, we use an invertible transformation T_e between a master element $\bar{\Omega}_e$ with a simple shape and an arbitrary element Ω_e . Let

$$\begin{aligned}
 x &= x(\chi, \xi, \zeta) \\
 T_e : \quad y &= y(\chi, \xi, \zeta) \\
 z &= z(\chi, \xi, \zeta)
 \end{aligned} \tag{5.10}$$

be the transformation which maps the master element $\bar{\Omega}_e$ in the system of (χ, ξ, ζ) to an element Ω_e in the system of (x, y, z) . As the transformation is invertible, there exists an inverse transformation:

$$\begin{aligned}
 \chi &= \chi(x, y, z) \\
 T_e^{-1} : \quad \xi &= \xi(x, y, z) \\
 \zeta &= \zeta(x, y, z)
 \end{aligned} \tag{5.11}$$

which maps Ω_e to $\bar{\Omega}_e$. Therefore, the integral domain for every element is the same in terms of the new integral variables, $\bar{\Omega}_e$.

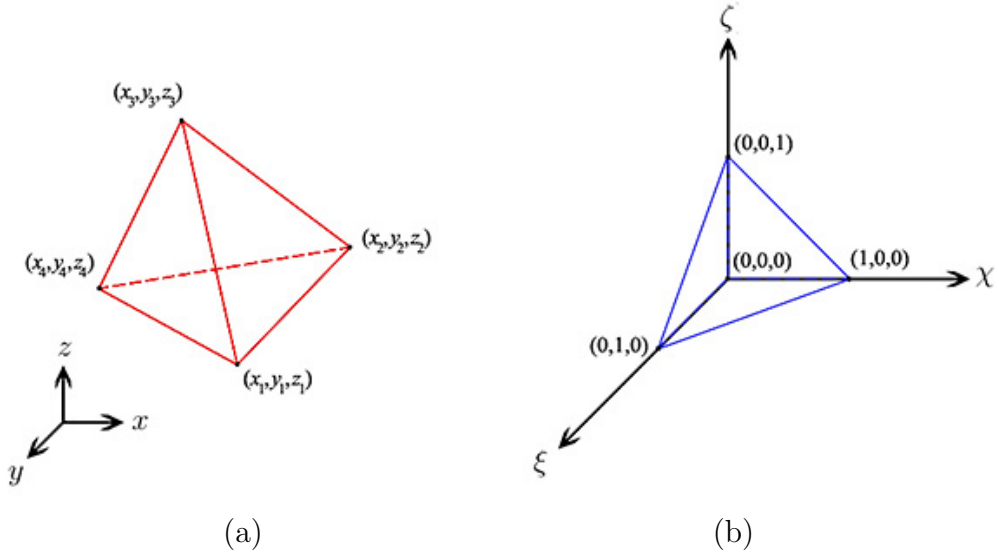


Figure 5.1: The tetrahedral elements.

In this thesis, the computational domain is discretized by using a tetrahedral shape $\{(x_i, y_i, z_i)\}_{i=1}^4$, as shown in Figure 5.1 (a). For the implementation, we choose the right tetrahedral element which has four corner points and straight edges given by $\{(\chi_i, \xi_i, \zeta_i)\}_{i=1}^4 = \{(0, 0, 0), (1, 0, 0), (0, 1, 0), (0, 0, 1)\}$, as shown in Figure 5.1 (b).

By assuming that Ω is divided into N tetrahedral elements, we can express the geometry of such elements using the nodal coordinates x_i , y_i and z_i with the shape function $S_i^e(\chi, \xi, \zeta)$. Thus, the coordinates x, y, z can be obtained from the transformation:

$$\begin{aligned}
 x &= \sum_{i=1}^4 S_i^e(\chi, \xi, \zeta) x_i \\
 T_e : \quad y &= \sum_{i=1}^4 S_i^e(\chi, \xi, \zeta) y_i \\
 z &= \sum_{i=1}^4 S_i^e(\chi, \xi, \zeta) z_i
 \end{aligned} \tag{5.12}$$

where $S_i^e(\chi, \xi, \zeta)$ is defined by

$$\begin{aligned}
 S_i^e(\chi, \xi, \zeta) &= 1 - (\chi_i + \xi_i + \zeta_i) + (-1 + 2\chi_i + \xi_i + \zeta_i)\chi \\
 &\quad + (-1 + \chi_i + 2\xi_i + \zeta_i)\xi + (-1 + \chi_i + \xi_i + 2\zeta_i)\zeta.
 \end{aligned} \tag{5.13}$$

For $i = 1, 2, 3, 4$, we can see that

$$\begin{aligned} S_1^e(\chi, \xi, \zeta) &= 1 - \chi - \xi - \zeta, \\ S_2^e(\chi, \xi, \zeta) &= \chi, \\ S_3^e(\chi, \xi, \zeta) &= \xi, \\ S_4^e(\chi, \xi, \zeta) &= \zeta, \end{aligned} \tag{5.14}$$

and the partial derivatives of the shape functions are

$$\begin{aligned} \frac{\partial S_i^e}{\partial \chi} &= -1 + 2\chi_i + \xi_i + \zeta_i, \\ \frac{\partial S_i^e}{\partial \xi} &= -1 + \chi_i + 2\xi_i + \zeta_i, \\ \frac{\partial S_i^e}{\partial \zeta} &= -1 + \chi_i + \xi_i + 2\zeta_i. \end{aligned} \tag{5.15}$$

To approximate the unknown variables of the problem, we choose four nodes of a tetrahedral element in Ω_e for interpolation. Let $\{f_i\}_{i=1}^4$ be the values of an unknown function f at node i of the master element $\bar{\Omega}_e$. We interpolate $f(\chi, \xi, \zeta)$ within $\bar{\Omega}_e$ by

$$f(\chi, \xi, \zeta) = \sum_{i=1}^4 S_i^e(\chi, \xi, \zeta) f_i. \tag{5.16}$$

However, for the pressure p , we choose the center of Ω_e as the node and the pressure $p = p^e \varrho_i^e$ with $\varrho_i^e = 1$ to ensure the convergence of the solution. As T_e is invertible, the element shape function for Ω_e in the coordinates (x, y, z) is ϕ_i^e , given by

$$\phi_i^e(x, y, z) = \psi_i^e(x, y, z) = S_i^e(\chi(x, y, z), \xi(x, y, z), \zeta(x, y, z)), \tag{5.17}$$

which means that $S_i^e(\chi, \xi, \zeta)$ can be considered as the transformation of ϕ_i^e and ψ_i^e of the system (x, y, z) to the system (χ, ξ, ζ) .

From the transformation T_e in equation (5.10), we can derive the Jacobian matrix J as follows

$$\begin{aligned}
dx &= \frac{\partial x}{\partial \chi} d\chi + \frac{\partial x}{\partial \xi} d\xi + \frac{\partial x}{\partial \zeta} d\zeta, \\
dy &= \frac{\partial y}{\partial \chi} d\chi + \frac{\partial y}{\partial \xi} d\xi + \frac{\partial y}{\partial \zeta} d\zeta, \\
dz &= \frac{\partial z}{\partial \chi} d\chi + \frac{\partial z}{\partial \xi} d\xi + \frac{\partial z}{\partial \zeta} d\zeta,
\end{aligned} \tag{5.18}$$

which can be written as

$$\begin{bmatrix} dx \\ dy \\ dz \end{bmatrix} = \begin{bmatrix} \frac{\partial x}{\partial \chi} & \frac{\partial x}{\partial \xi} & \frac{\partial x}{\partial \zeta} \\ \frac{\partial y}{\partial \chi} & \frac{\partial y}{\partial \xi} & \frac{\partial y}{\partial \zeta} \\ \frac{\partial z}{\partial \chi} & \frac{\partial z}{\partial \xi} & \frac{\partial z}{\partial \zeta} \end{bmatrix} \begin{bmatrix} d\chi \\ d\xi \\ d\zeta \end{bmatrix} = J \begin{bmatrix} d\chi \\ d\xi \\ d\zeta \end{bmatrix}. \tag{5.19}$$

From the inverse transformation in equation (5.11), we get

$$\begin{bmatrix} d\chi \\ d\xi \\ d\zeta \end{bmatrix} = J^{-1} \begin{bmatrix} dx \\ dy \\ dz \end{bmatrix}, \tag{5.20}$$

where J^{-1} is the inverse of Jacobian matrix J , given by

$$\begin{aligned}
J^{-1} &= \begin{bmatrix} \frac{\partial \chi}{\partial x} & \frac{\partial \chi}{\partial y} & \frac{\partial \chi}{\partial z} \\ \frac{\partial \xi}{\partial x} & \frac{\partial \xi}{\partial y} & \frac{\partial \xi}{\partial z} \\ \frac{\partial \zeta}{\partial x} & \frac{\partial \zeta}{\partial y} & \frac{\partial \zeta}{\partial z} \end{bmatrix} = \begin{bmatrix} \frac{\partial x}{\partial \chi} & \frac{\partial x}{\partial \xi} & \frac{\partial x}{\partial \zeta} \\ \frac{\partial y}{\partial \chi} & \frac{\partial y}{\partial \xi} & \frac{\partial y}{\partial \zeta} \\ \frac{\partial z}{\partial \chi} & \frac{\partial z}{\partial \xi} & \frac{\partial z}{\partial \zeta} \end{bmatrix}^{-1} \\
&= \frac{1}{\det(J)} \begin{bmatrix} C_{11} & C_{12} & C_{13} \\ C_{21} & C_{22} & C_{23} \\ C_{31} & C_{32} & C_{33} \end{bmatrix}^T, \tag{5.21}
\end{aligned}$$

where $\det(J)$ is the determinant of the following Jacobian matrix, and

$$\begin{aligned}
C_{11} &= J_{22}J_{33} - J_{23}J_{32}, & C_{21} &= J_{23}J_{31} - J_{21}J_{33}, & C_{31} &= J_{21}J_{32} - J_{22}J_{31}, \\
C_{12} &= J_{13}J_{32} - J_{12}J_{33}, & C_{22} &= J_{11}J_{33} - J_{13}J_{31}, & C_{32} &= J_{12}J_{31} - J_{11}J_{32}, \\
C_{13} &= J_{12}J_{23} - J_{13}J_{22}, & C_{23} &= J_{13}J_{21} - J_{11}J_{23}, & C_{33} &= J_{11}J_{22} - J_{12}J_{21}.
\end{aligned}$$

From equation (5.21), we can obtain

$$\frac{\partial \chi}{\partial x} = \frac{1}{\det(J)} C_{11}, \quad \frac{\partial \chi}{\partial y} = \frac{1}{\det(J)} C_{21}, \quad \frac{\partial \chi}{\partial z} = \frac{1}{\det(J)} C_{31},$$

$$\frac{\partial \xi}{\partial x} = \frac{1}{\det(J)} C_{12}, \quad \frac{\partial \xi}{\partial y} = \frac{1}{\det(J)} C_{22}, \quad \frac{\partial \xi}{\partial z} = \frac{1}{\det(J)} C_{32},$$

$$\frac{\partial \zeta}{\partial x} = \frac{1}{\det(J)} C_{13}, \quad \frac{\partial \zeta}{\partial y} = \frac{1}{\det(J)} C_{23}, \quad \frac{\partial \zeta}{\partial z} = \frac{1}{\det(J)} C_{33}.$$

Therefore, by using the composite rule for differentiation with the shape function $\phi_k^e = S_k$; $k = 1, 2, 3, 4$, we have

$$\frac{\partial \phi_k}{\partial x} = \frac{\partial S_k}{\partial \chi} \frac{\partial \chi}{\partial x} + \frac{\partial S_k}{\partial \xi} \frac{\partial \xi}{\partial x} + \frac{\partial S_k}{\partial \zeta} \frac{\partial \zeta}{\partial x},$$

$$\frac{\partial \phi_k}{\partial y} = \frac{\partial S_k}{\partial \chi} \frac{\partial \chi}{\partial y} + \frac{\partial S_k}{\partial \xi} \frac{\partial \xi}{\partial y} + \frac{\partial S_k}{\partial \zeta} \frac{\partial \zeta}{\partial y},$$

$$\frac{\partial \phi_k}{\partial z} = \frac{\partial S_k}{\partial \chi} \frac{\partial \chi}{\partial z} + \frac{\partial S_k}{\partial \xi} \frac{\partial \xi}{\partial z} + \frac{\partial S_k}{\partial \zeta} \frac{\partial \zeta}{\partial z}.$$

The transformation of integrals for any function $f(x, y, z)$ on each tetrahedral element in the (x, y, z) system into a right tetrahedral element in the (χ, ξ, ζ) system is

$$\int_{\Omega_e} f(x, y, z) dx dy dz = \int_{\Omega_e} f(\chi, \xi, \zeta) \det(J) d\chi d\xi d\zeta. \quad (5.22)$$

By denoting

$$B_i^j(\chi, \xi, \zeta) = \frac{\partial \phi_j}{\partial x_i}, \quad i = 1, 2, 3 \quad \text{and} \quad j = 1, 2, 3, 4, \quad (5.23)$$

the element matrices corresponding to the global matrices and load vectors defined in (5.9) can be computed from

$$\begin{aligned} (m_{\beta\alpha})_e &= \int_0^1 \int_0^{1-\zeta} \int_0^{1-\xi-\zeta} \rho S_\beta^e S_\alpha^e \det(J) d\chi d\xi d\zeta, \\ (a(u)_{\beta\alpha})_e &= \int_0^1 \int_0^{1-\zeta} \int_0^{1-\xi-\zeta} \rho S_\beta^e (u_1 B_1^\alpha + u_2 B_2^\alpha + u_3 B_3^\alpha) \det(J) d\chi d\xi d\zeta, \\ ((b_{mn})_{\beta\alpha})_e &= \int_0^1 \int_0^{1-\zeta} \int_0^{1-\xi-\zeta} \eta B_n^\beta B_m^\alpha \det(J) d\chi d\xi d\zeta, \\ (\hat{c}_{\delta\alpha}^i)_e &= \int_0^1 \int_0^{1-\zeta} \int_0^{1-\xi-\zeta} B_i^\alpha \det(J) d\chi d\xi d\zeta, \\ (\hat{c}_{\beta\gamma}^i)_e &= - \int_0^1 \int_0^{1-\zeta} \int_0^{1-\xi-\zeta} B_i^\beta \det(J) d\chi d\xi d\zeta. \end{aligned} \quad (5.24)$$

5.3.2 Surface Elements

On the boundary, we denote the surface integrals by

$$\int_{\Gamma} f(x, y, z) d\Gamma. \quad (5.25)$$

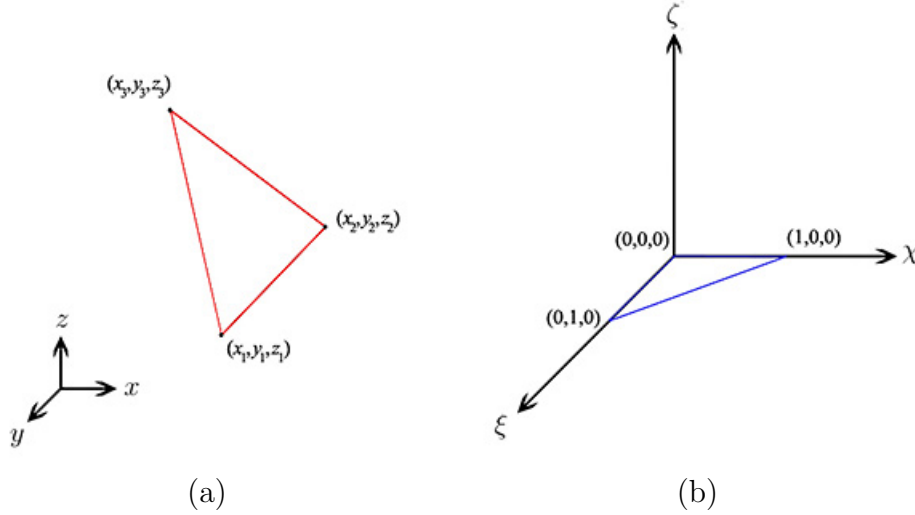


Figure 5.2: The surfaces of tetrahedral element.

To evaluate the integrals on the surface of Ω_e , we need to find the transformation for the surface integrals which map the surface of element $\bar{\Omega}_e$ to Ω_e . In three-dimensional space, a surface element can be described by

$$R(\chi, \xi, 0) = (x(\chi, \xi, 0), y(\chi, \xi, 0), z(\chi, \xi, 0)), \quad \text{for } 0 \leq \chi \leq 1 - \xi, 0 \leq \xi \leq 1.$$

Therefore, the surface integral of any function $f(x, y, z)$ defined on the boundary Γ can be calculated from

$$\int_{\Gamma} f(x, y, z) d\Gamma = \int_{\Gamma(\chi, \xi)} f(x(\chi, \xi, 0), y(\chi, \xi, 0), z(\chi, \xi, 0)) \left| \frac{\partial R}{\partial \chi} \times \frac{\partial R}{\partial \xi} \right| d\chi d\xi,$$

where $R = R(\chi, \xi, 0)$ and

$$\begin{aligned} x(\chi, \xi, 0) &= \sum_{i=1}^3 S_i^e(\chi, \xi) x_i, \\ y(\chi, \xi, 0) &= \sum_{i=1}^3 S_i^e(\chi, \xi) y_i, \\ z(\chi, \xi, 0) &= \sum_{i=1}^3 S_i^e(\chi, \xi) z_i. \end{aligned}$$

The shape functions S_i^e for the right triangular element are given by

$$S_1^e(\chi, \xi) = 1 - \chi - \xi,$$

$$S_2^e(\chi, \xi) = \chi,$$

$$S_3^e(\chi, \xi) = \xi,$$

or S_i^e can be written in the form

$$S_i^e(\chi, \xi) = 1 - (\chi_i + \xi_i) + (-1 + 2\chi_i + \xi_i)\chi + (-1 + \chi + 2\xi_i)\xi. \quad (5.26)$$

From

$$\begin{aligned} \frac{\partial R}{\partial \chi} &= \left(\frac{\partial x}{\partial \chi}, \frac{\partial y}{\partial \chi}, \frac{\partial z}{\partial \chi} \right) \\ &= \left(\sum_{i=1}^3 \frac{\partial S_i^e}{\partial \chi} x_i, \sum_{i=1}^3 \frac{\partial S_i^e}{\partial \chi} y_i, \sum_{i=1}^3 \frac{\partial S_i^e}{\partial \chi} z_i \right) \text{ and} \end{aligned}$$

$$\begin{aligned} \frac{\partial R}{\partial \xi} &= \left(\frac{\partial x}{\partial \xi}, \frac{\partial y}{\partial \xi}, \frac{\partial z}{\partial \xi} \right) \\ &= \left(\sum_{i=1}^3 \frac{\partial S_i^e}{\partial \xi} x_i, \sum_{i=1}^3 \frac{\partial S_i^e}{\partial \xi} y_i, \sum_{i=1}^3 \frac{\partial S_i^e}{\partial \xi} z_i \right), \end{aligned}$$

we have

$$\frac{\partial R}{\partial \chi} \times \frac{\partial R}{\partial \xi} = \left(\left(\frac{\partial y}{\partial \chi} \frac{\partial z}{\partial \xi} - \frac{\partial z}{\partial \chi} \frac{\partial y}{\partial \xi} \right), \left(\frac{\partial x}{\partial \chi} \frac{\partial z}{\partial \xi} - \frac{\partial z}{\partial \chi} \frac{\partial x}{\partial \xi} \right), \left(\frac{\partial x}{\partial \chi} \frac{\partial y}{\partial \xi} - \frac{\partial y}{\partial \chi} \frac{\partial x}{\partial \xi} \right) \right).$$

Thus,

$$\begin{aligned} \det(J) &= \left| \frac{\partial R}{\partial \chi} \times \frac{\partial R}{\partial \xi} \right| \\ &= \sqrt{\left(\frac{\partial y}{\partial \chi} \frac{\partial z}{\partial \xi} - \frac{\partial z}{\partial \chi} \frac{\partial y}{\partial \xi} \right)^2 + \left(\frac{\partial x}{\partial \chi} \frac{\partial z}{\partial \xi} - \frac{\partial z}{\partial \chi} \frac{\partial x}{\partial \xi} \right)^2 + \left(\frac{\partial x}{\partial \chi} \frac{\partial y}{\partial \xi} - \frac{\partial y}{\partial \chi} \frac{\partial x}{\partial \xi} \right)^2}. \end{aligned}$$

5.4 Numerical Algorithm

In this section, we find the finite element solutions of the system of equations (5.7) by using the backward Euler difference scheme with a typical time step $\Delta t_n = t_{n+1} - t_n$. We then have

$$\dot{\mathbf{U}} = \frac{\mathbf{U}_{n+1} - \mathbf{U}_n}{\Delta t_n},$$

and

$$\begin{aligned} C^T \mathbf{U}_{n+1} &= \mathbf{0}, \\ \left(\frac{M}{\Delta t_n} + A(u) + B \right) \mathbf{U}_{n+1} + \hat{C} \mathbf{P}_{n+1} &= \frac{M}{\Delta t_n} \mathbf{U}_n, \end{aligned} \quad (5.27)$$

which is a nonlinear system because $A(u)$ depends on \mathbf{U}_{n+1} . To deal with the non-linearity for an iterative solution of equation (5.27), we use the iterative updating as follows:

$$\begin{aligned} C^T \mathbf{U}_{n+1}^{i+1} &= \mathbf{0}, \\ \left(\frac{M}{\Delta t_n} + A^i(u) + B^i \right) \mathbf{U}_{n+1}^{i+1} + \hat{C} \mathbf{P}_{n+1}^{i+1} &= \frac{M}{\Delta t_n} \mathbf{U}_n^i, \end{aligned} \quad (5.28)$$

where superscript i denotes an evaluation at the i th iteration step. By starting with $\mathbf{U}_{n+1}^0 = \mathbf{U}_n$ and $\mathbf{P}_{n+1}^0 = \mathbf{P}_n$, we can determine \mathbf{U}_{n+1}^{i+1} and \mathbf{P}_{n+1}^{i+1} by repeatedly solving the system of equations (5.28) until $\|\mathbf{U}_{n+1}^{i+1} - \mathbf{U}_{n+1}^i\| \leq 0.001$ and $\|\mathbf{P}_{n+1}^{i+1} - \mathbf{P}_{n+1}^i\| \leq 0.001$.

We can determine the state \mathbf{U} and \mathbf{P} by repeatedly using the above procedure for $n = 1, 2, 3, \dots$. If $\|\mathbf{U}_{n+1} - \mathbf{U}_n\|$ and $\|\mathbf{P}_{n+1} - \mathbf{P}_n\|$ are sufficiently small, the system approaches the so-called steady state.

5.5 Mesh Sensitivity Analysis

The domains of the coronary arteries system with four different stenosis degrees with no graft and with no graft and with a bypass graft are discretized into many elements for analyzing the mesh sensitivity. Figures 5.4 and 5.5 show the element mesh of the computational domains. Tables 5.1 and 5.2 show the number of tetrahedral elements and degrees of freedom of the computational domains. Figure 5.3 shows the investigated point of mesh sensitivity.

Figures 5.6 to 5.13 present the mesh sensitivity of the computational domain having four different stenosed RCA including 0%, 40%, 63%, and 72% with no graft and with a bypass graft. The results indicate that convergence tends to be achieved when the number of mesh element is higher than 60,000.

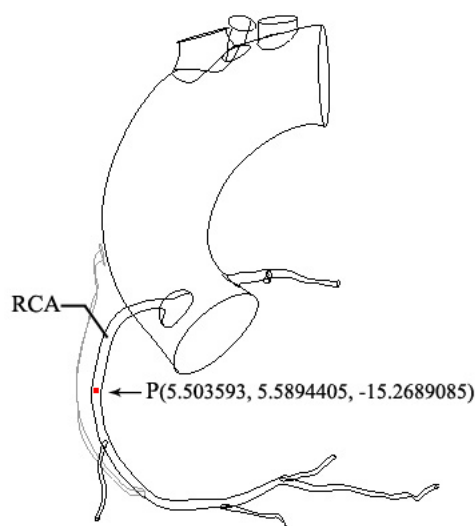


Figure 5.3: The investigated point of mesh sensitivity analysis.

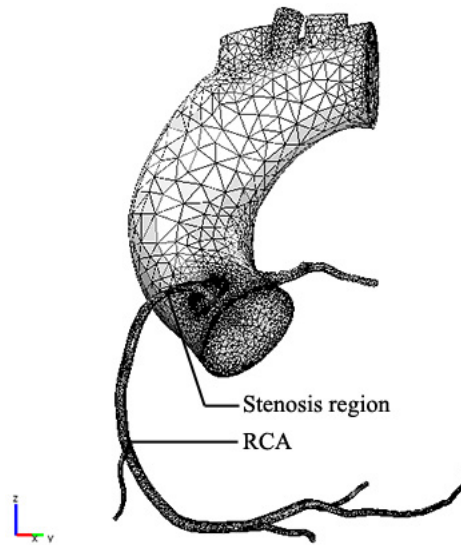


Figure 5.4: The element mesh of the domain with no graft.

Table 5.1: The number of tetrahedral elements (NE) and degrees of freedom (DF) of the computational domains with no graft.

Mesh		Degree of RCA stenosis			
		0%	40%	63%	72%
Coarse	NE	16155	20425	20270	20747
	DF	137829	110609	109775	110049
Normal	NE	25197	29538	28422	28739
	DF	137829	155750	150090	151472
Fine	NE	33347	37002	36209	36709
	DF	180606	194740	190756	192372
Finer	NE	40984	45197	43821	44758
	DF	219384	235867	229104	232777
Extra fine	NE	49300	55279	53679	53596
	DF	260775	285533	277713	276448
Extremely fine	NE	57553	63652	61911	62701
	DF	301738	325281	317912	321088

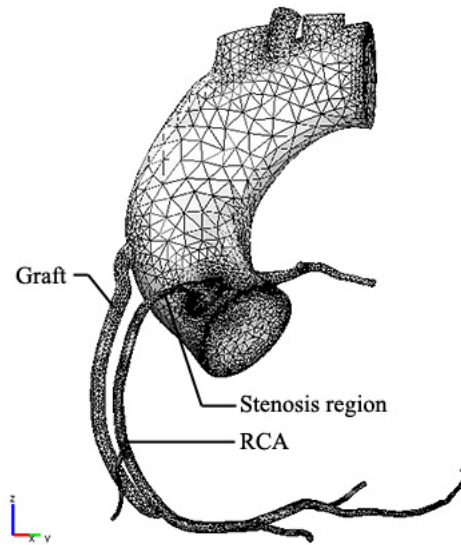
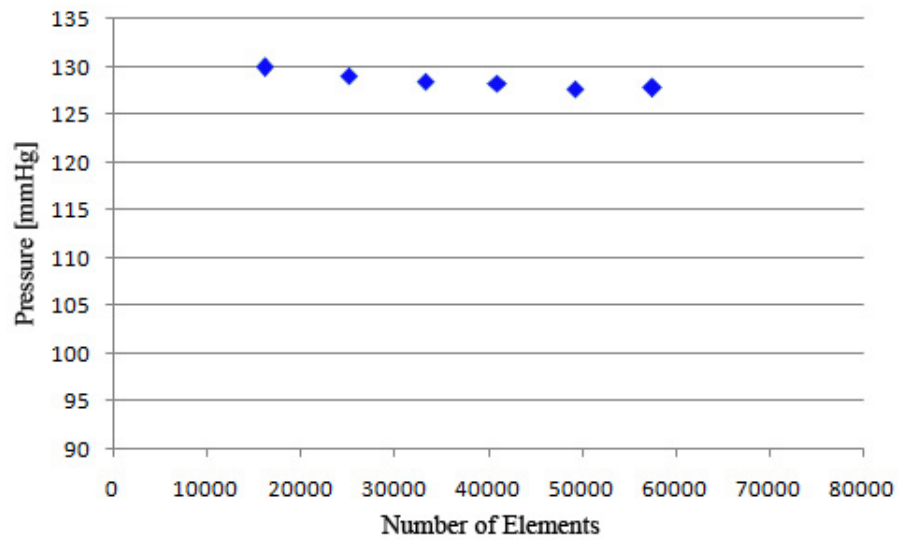


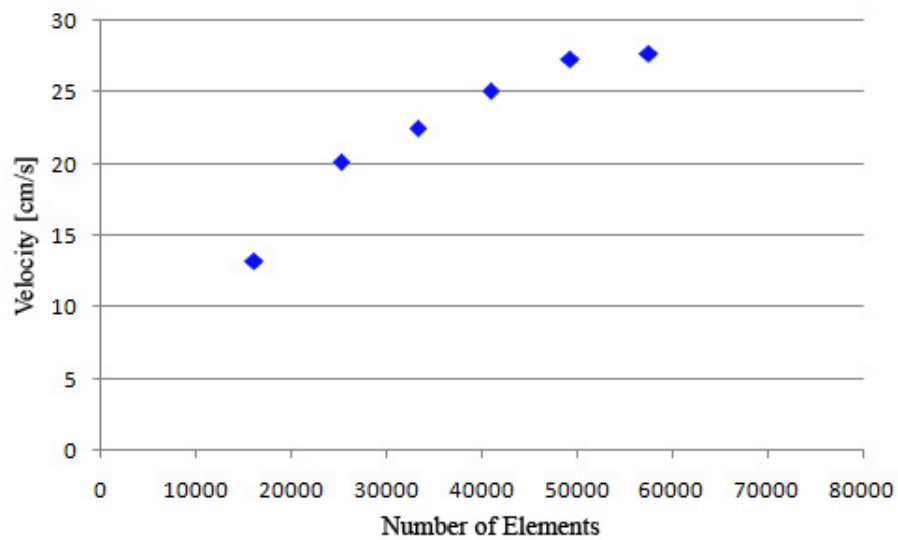
Figure 5.5: The element mesh of the domain with a bypass graft.

Table 5.2: The number of tetrahedral elements (NE) and degrees of freedom (DF) of the computational domains with a bypass graft.

Mesh		Degree of RCA stenosis			
		0%	40%	63%	72%
Coarse	NE	27987	28695	26086	31172
	DF	149739	153001	140815	164499
Normal	NE	36727	36717	36403	39916
	DF	192782	191771	192268	207264
Fine	NE	44644	44011	44284	46349
	DF	234173	229008	233413	240886
Finer	NE	52090	52209	51844	55344
	DF	271705	269019	270979	285568
Extra fine	NE	60796	61190	59920	62955
	DF	313943	315229	311531	323931
Extremely fine	NE	67856	69138	68851	71619
	DF	348780	354132	354166	366748

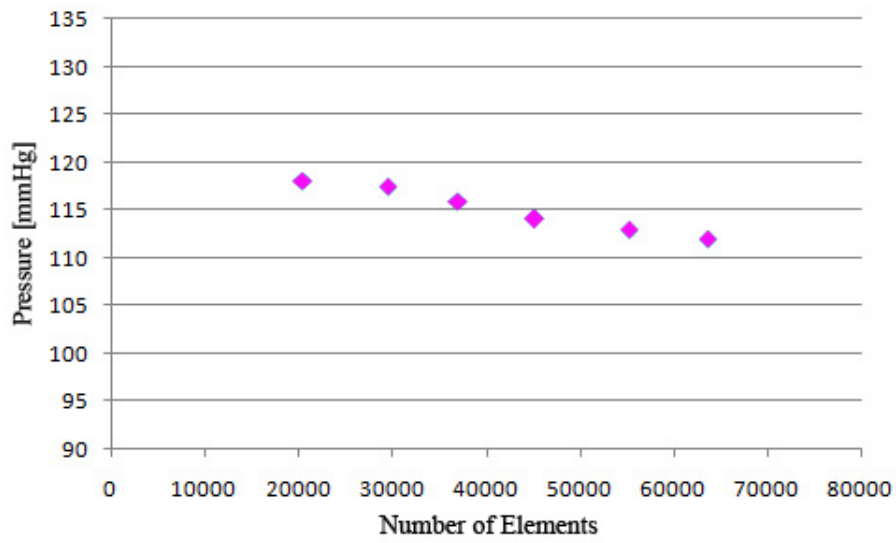


(a)

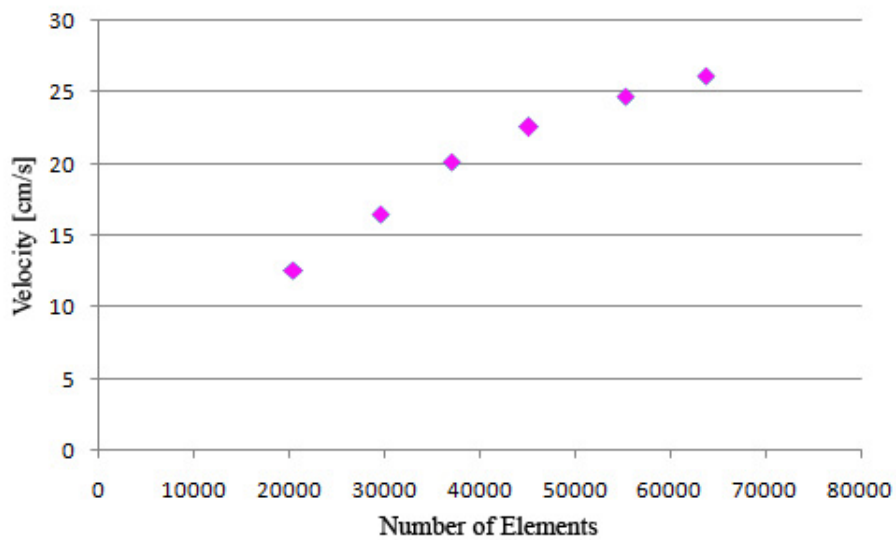


(b)

Figure 5.6: The mesh sensitivity analysis of the computational domain having 0% stenosed RCA with no graft by comparing the pressures and velocities at point P (Figure 5.3) at the peak of systole: (a) blood pressure; (b) blood velocity.

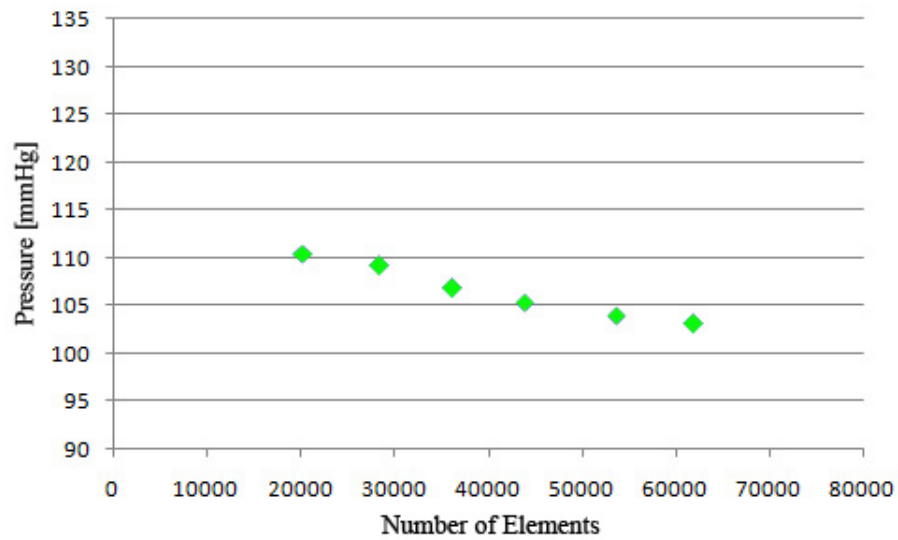


(a)

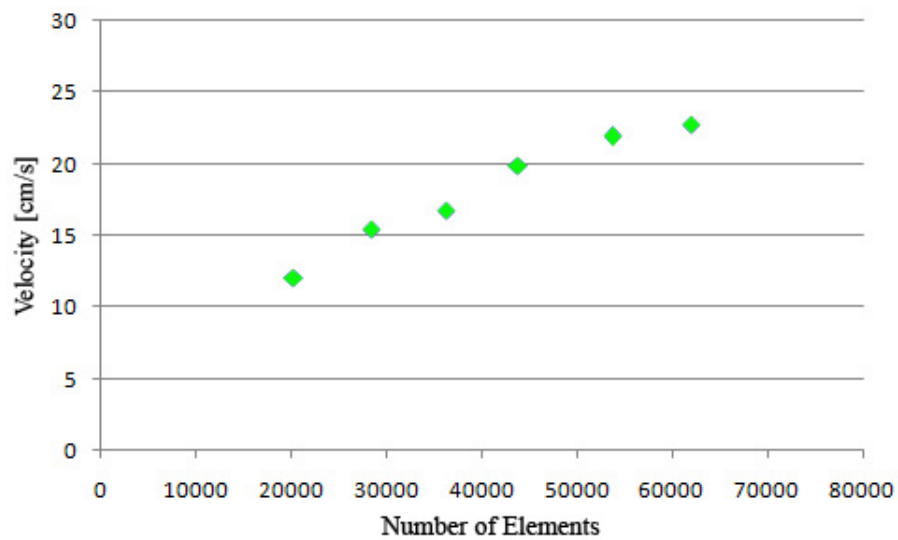


(b)

Figure 5.7: The mesh sensitivity analysis of the computational domain having 40% stenosed RCA with no graft by comparing the pressures and velocities at point P (Figure 5.3) at the peak of systole: (a) blood pressure; (b) blood velocity.

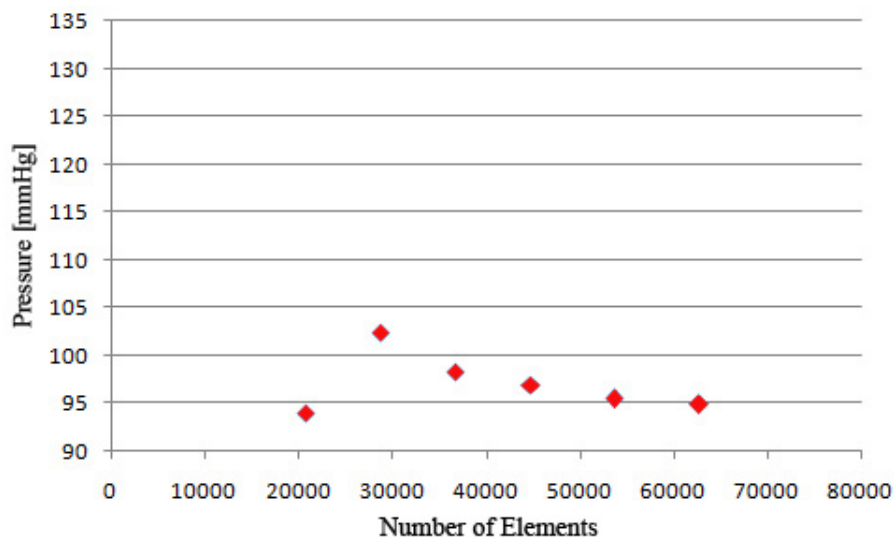


(a)

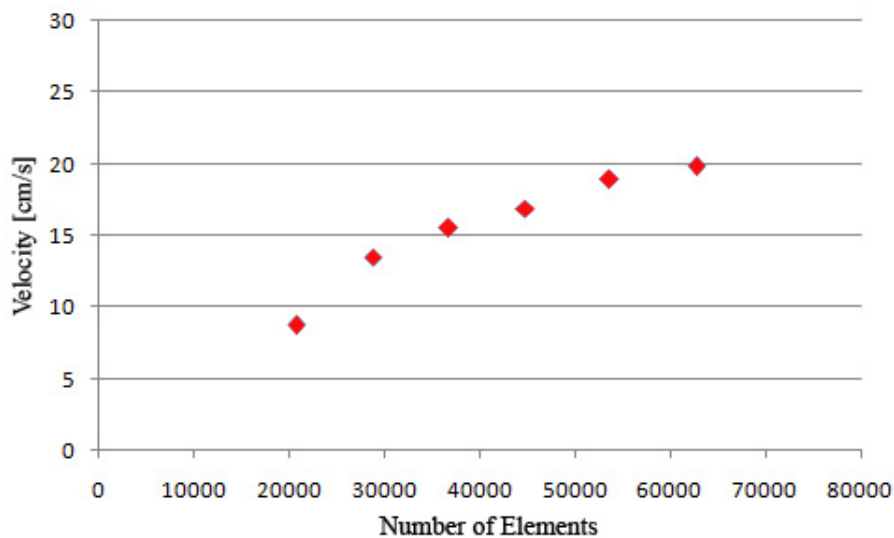


(b)

Figure 5.8: The mesh sensitivity analysis of the computational domain having 63% stenosed RCA with no graft by comparing the pressures and velocities at point P (Figure 5.3) at the peak of systole: (a) blood pressure; (b) blood velocity.

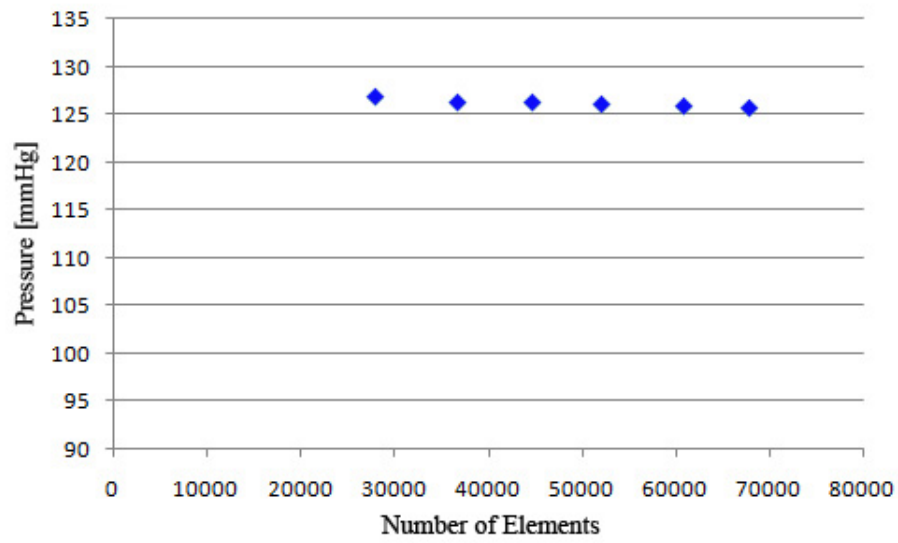


(a)

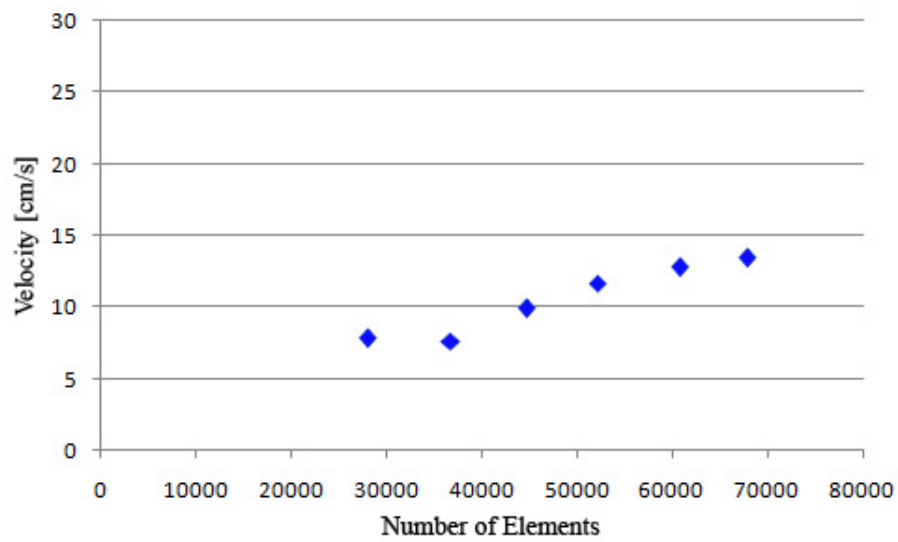


(b)

Figure 5.9: The mesh sensitivity analysis of the computational domain having 72% stenosed RCA with no graft by comparing the pressures and velocities at point P (Figure 5.3) at the peak of systole: (a) blood pressure; (b) blood velocity.

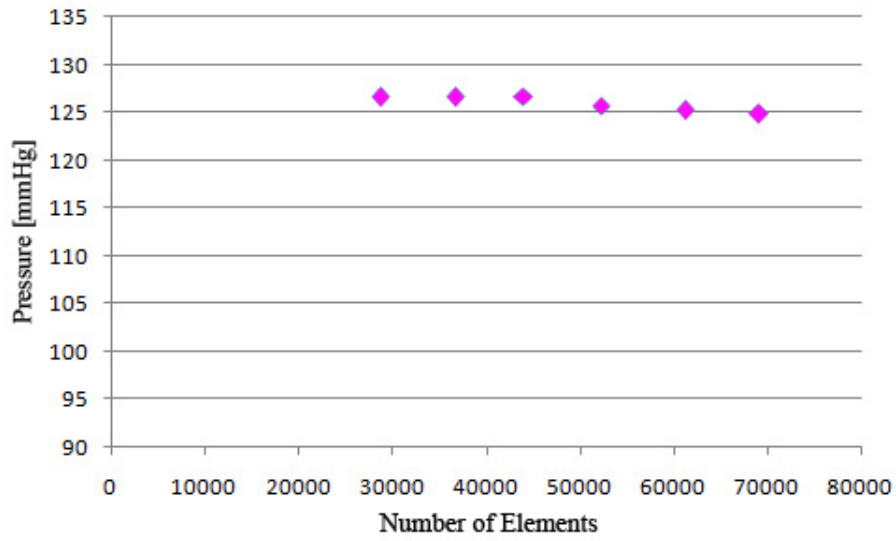


(a)

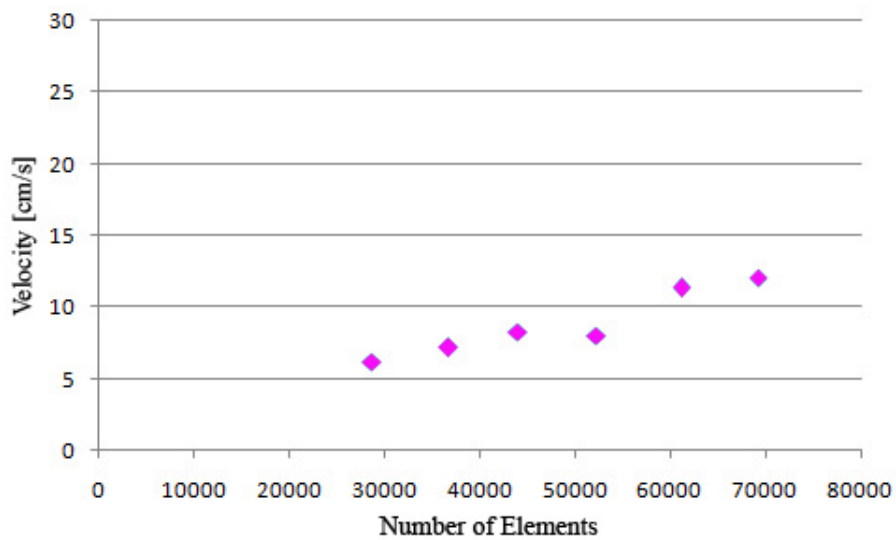


(b)

Figure 5.10: The mesh sensitivity analysis of the computational domain having 0% stenosed RCA with a bypass graft by comparing the pressures and velocities at point P (Figure 5.3) at the peak of systole: (a) blood pressure; (b) blood velocity.

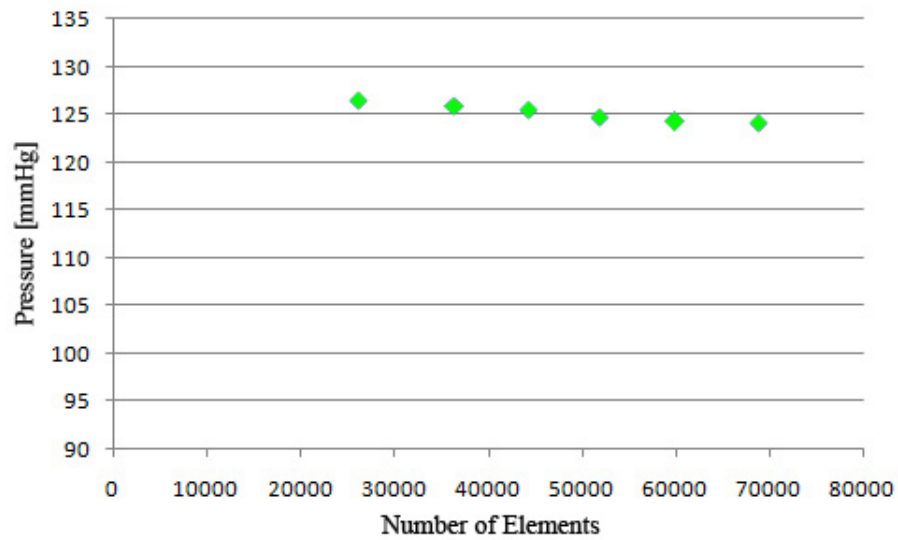


(a)

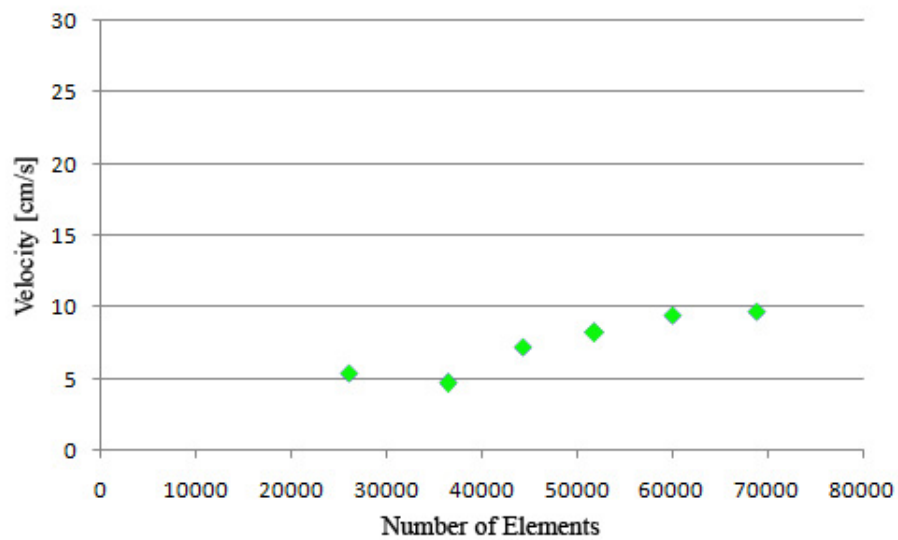


(b)

Figure 5.11: The mesh sensitivity analysis of the computational domain having 40% stenosed RCA with a bypass graft by comparing the pressures and velocities at point P (Figure 5.3) at the peak of systole: (a) blood pressure; (b) blood velocity.

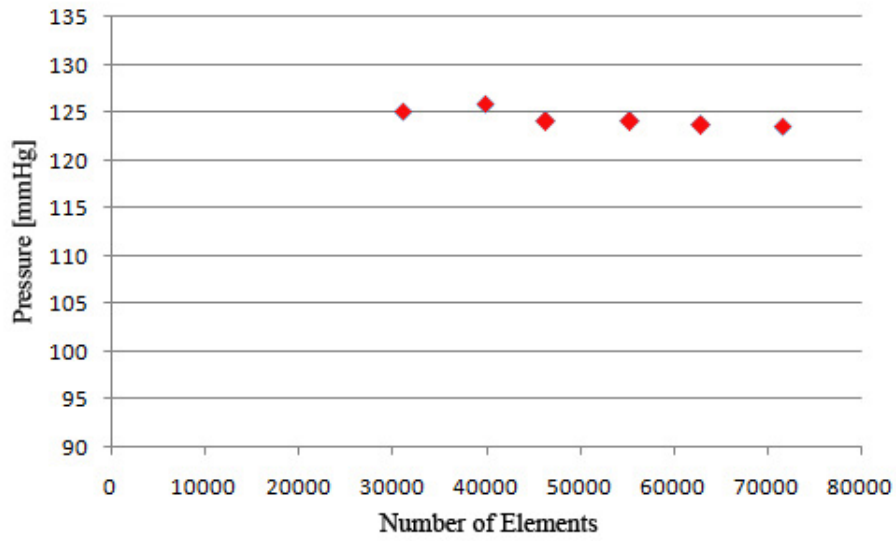


(a)

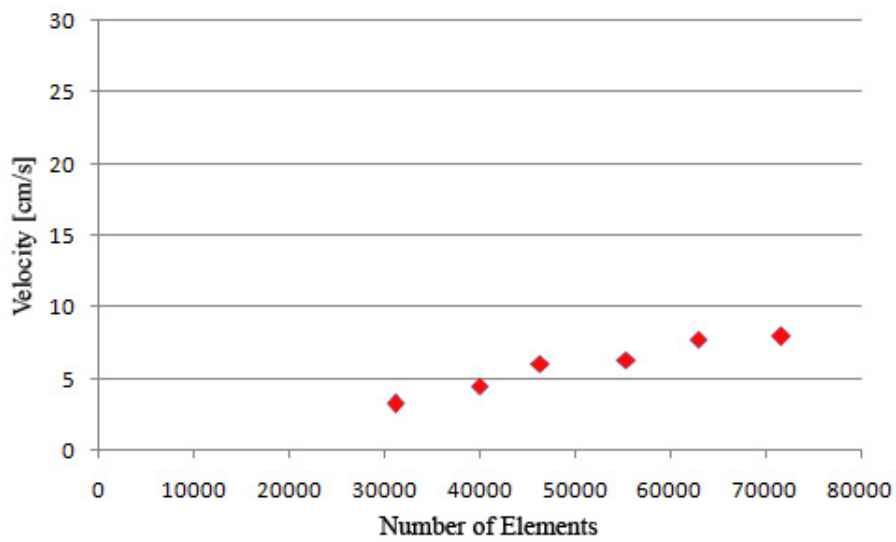


(b)

Figure 5.12: The mesh sensitivity analysis of the computational domain having 63% stenosed RCA with a bypass graft by comparing the pressures and velocities at point P (Figure 5.3) at the peak of systole: (a) blood pressure; (b) blood velocity.



(a)



(b)

Figure 5.13: The mesh sensitivity analysis of the computational domain having 72% stenosed RCA with a bypass graft by comparing the pressures and velocities at point P (Figure 5.3) at the peak of systole: (a) blood pressure; (b) blood velocity.

CHAPTER VI

NUMERICAL EXAMPLES

6.1 General Overview

This chapter concerns the computational results for the three-dimensional blood flow problem presented in Chapter V. The behavior of blood pressure, wall shear stress and blood velocity are investigated in sections 6.2 - 6.5. The pulsatile pressure and flow rate at the inlet surface of the aorta are shown in Figure 6.1.

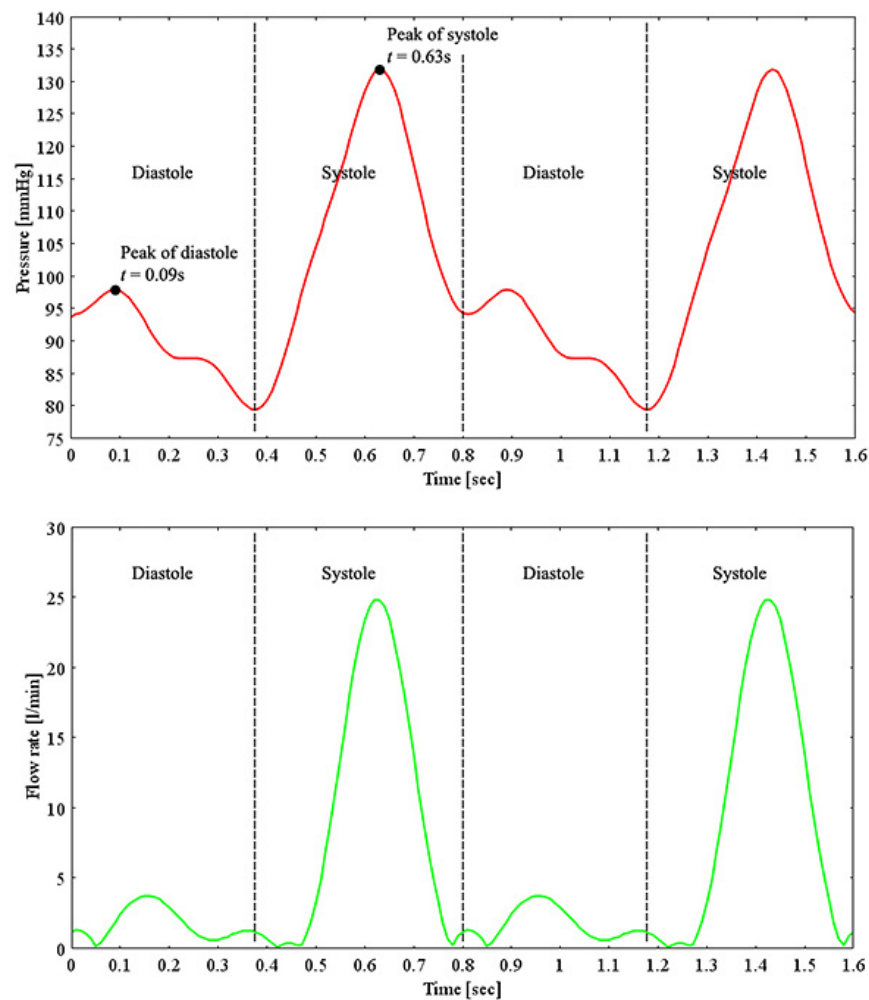


Figure 6.1: The pulsatile pressure and flow rate at the inflow surface of the aorta.

6.2 The Effect of Branching in a Human Coronary Artery

To study the effect of branching in the system of coronary arteries, we construct two domains of the coronary system with no branch and with branches, as shown in Figure 6.2. The investigated RCA axis is shown in figure 6.3. The numerical results and discussion are in following subsections.

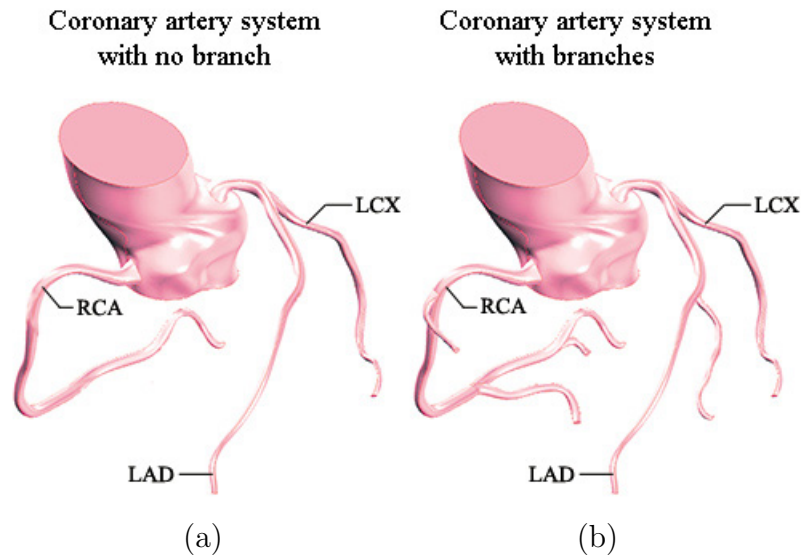


Figure 6.2: The computational domains of the coronary artery system (a) with no branch; and (b) with branches.

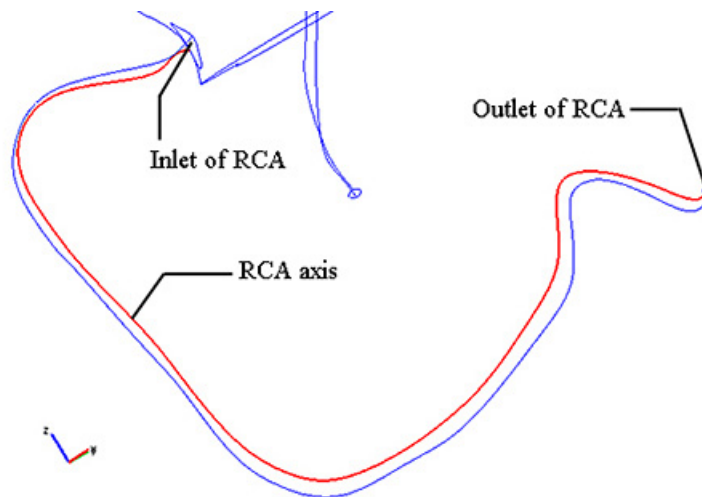


Figure 6.3: The investigated RCA axis and inlet and outlet of the RCA.

6.2.1 Pressure

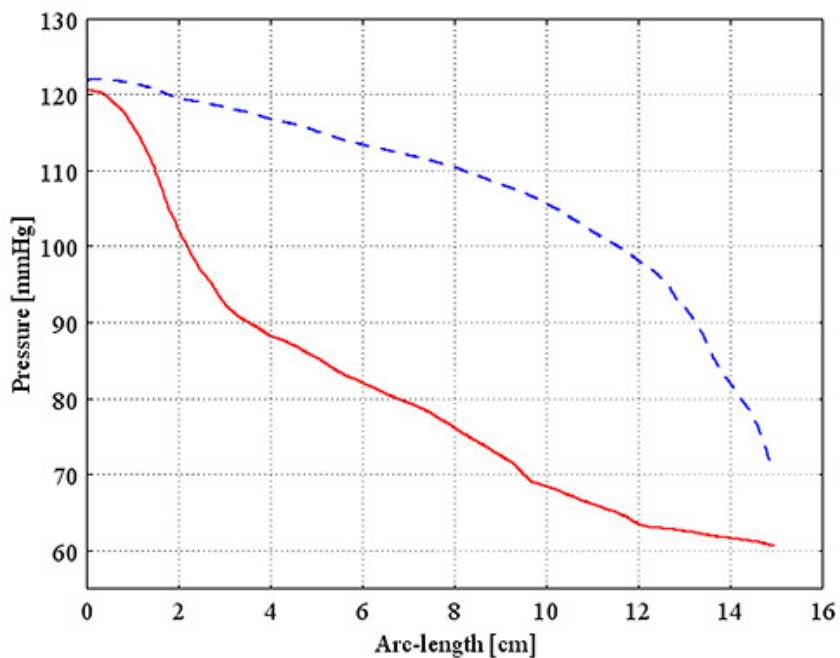
The pressures along the main artery of the RCA obtained from the model with no branch and with branches are shown in Figure 6.4. The results indicate that blood pressures in the system with branches are significantly less than the ones in the system with no branch along the RCA axis.

6.2.2 Wall Shear Stress

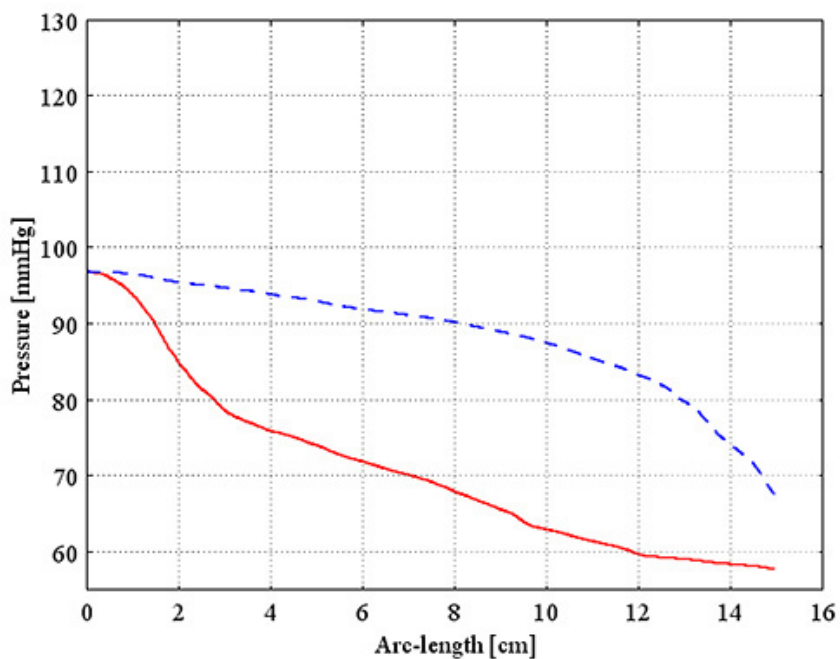
Figure 6.5 shows the wall shear stresses along the main arteries of the RCA at the peak of systole and the peak of diastole. We can see that the wall shear stress obtained from model with branches tends to increase along the RCA axis compared with the one with no branch.

6.2.3 Velocity Field

Figure 6.6 shows the comparison of blood speed of the coronary artery system with no branch and with branches at the RCA inlet (Figure 6.6 (a)) and RCA outlet (Figure 6.6 (b)). The results indicate that the blood velocity of the domain with no branch is higher than the one with branches.

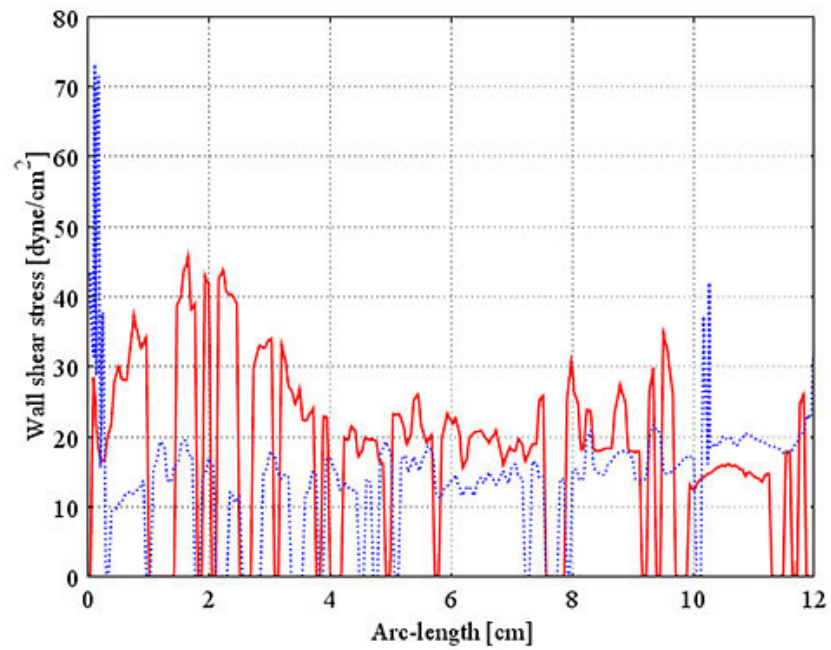


(a)

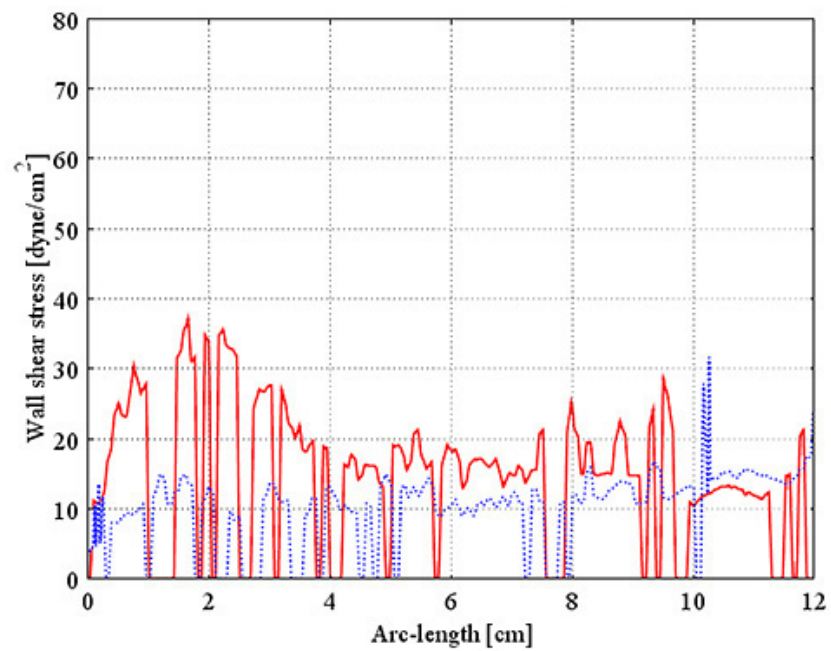


(b)

Figure 6.4: The pressure along the RCA axis obtained from the model with no branch (dashed line) and model with branches (solid line) at two different times: (a) at the peak of systole; and (b) at the peak of diastole.

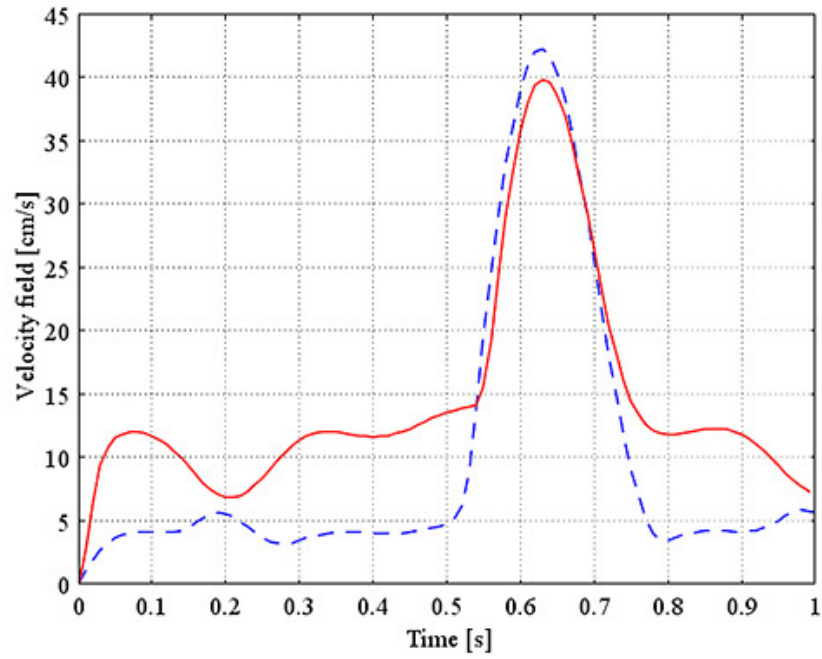


(a)

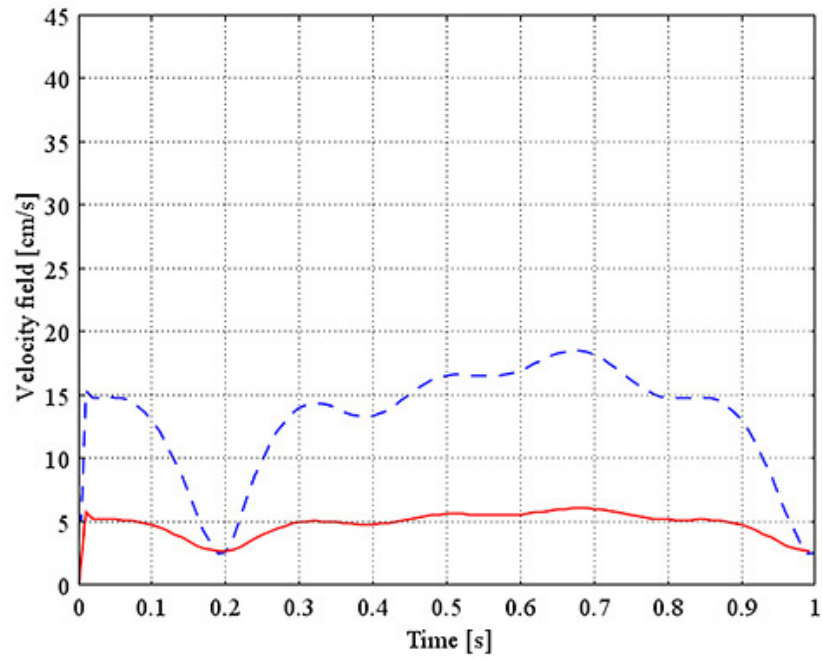


(b)

Figure 6.5: The wall shear stress along the RCA axis obtained from the model with no branch (dashed line) and model with branches (solid line) at two different times: (a) at the peak of systole; and (b) at the peak of diastole.



(a)



(b)

Figure 6.6: The velocity field obtained from the model with no branch (dashed line) and model with branches (solid line) (a) at the entrance of the main artery of the RCA; and (b) at the end of the main artery of the RCA during a cardiac cycle.

To investigate the effect of the non-Newtonian property, stenosis and bypass grafting, the computational domains shown in Chapter 4 (Figure 4.3) are used to simulate the blood flow. In Figure 6.7, the blood pressure and the wall shear stress are investigated along the RCA axis. The velocity field is investigated in three planes, plane A, plane B, and plane C as shown in Figure 6.8.

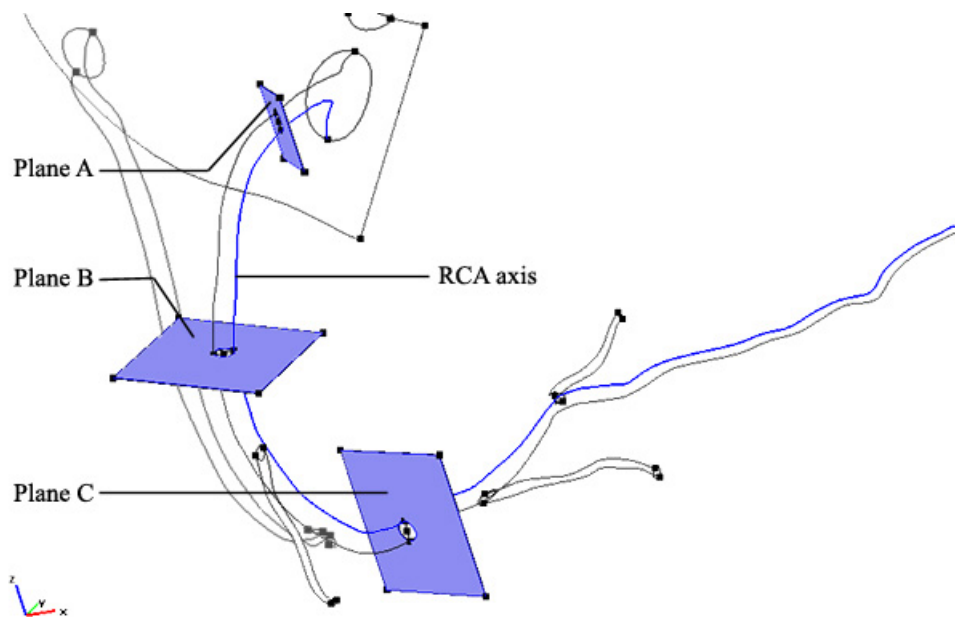


Figure 6.7: The investigated RCA axis and three investigated planes consisting of plane A, plane B, and plane C.

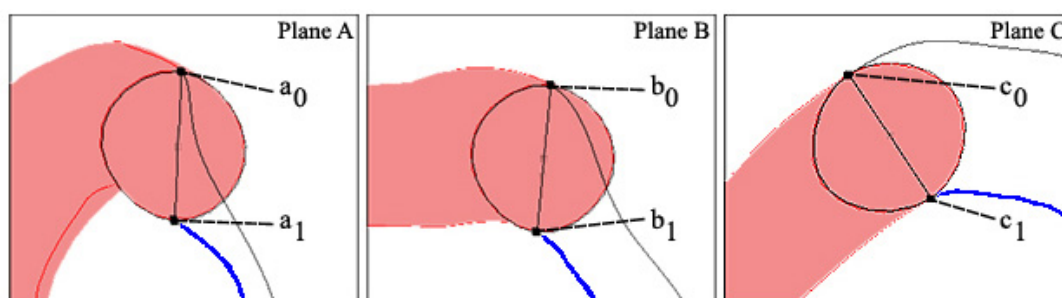


Figure 6.8: The investigated line a_0a_1 , b_0b_1 , and c_0c_1 in plane A, plane B, and plane C, respectively.

6.3 The Effect of the Non-Newtonian Property of Blood

In this section, we compare the blood flow behavior of the Newtonian model and non-Newtonian model. In the case of Newtonian flow, the viscosity of blood is set to $\eta = 0.0345 \text{ g} \cdot \text{cm}^{-1} \cdot \text{s}^{-1}$ [83]. For non-Newtonian flow, we assume the blood viscosity is a function of shear rate based on Carreau's shear-thinning model [22]. The characteristics of blood flow are investigated in the normal RCA of the coronary artery system. The numerical results and discussion are presented in following subsections.

6.3.1 Pressure

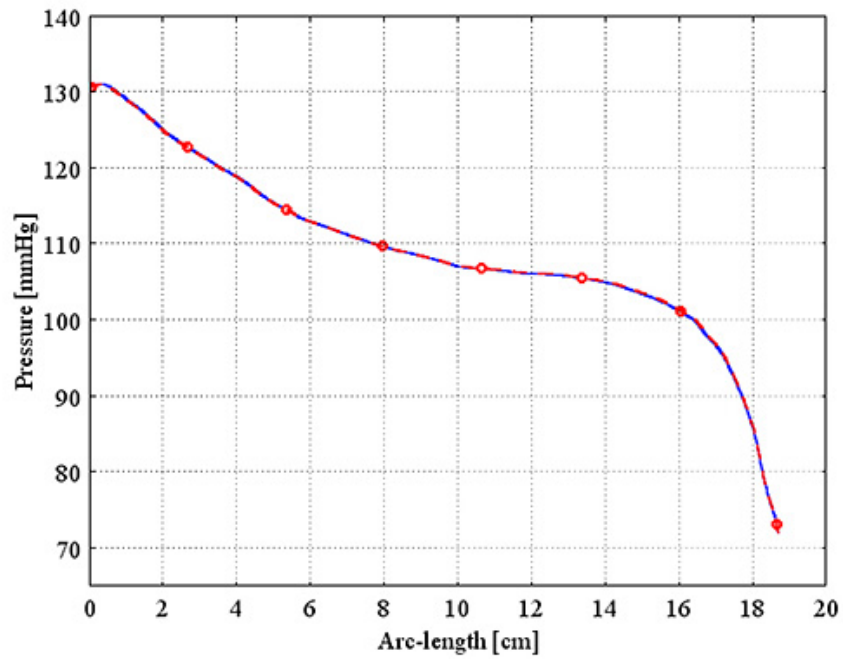
The pressures along the RCA axis obtained from the Newtonian and non-Newtonian models are shown in Figure 6.9. The results indicate that there is no significant difference in the pressure between the Newtonian and non-Newtonian blood flow.

6.3.2 Wall Shear Stress

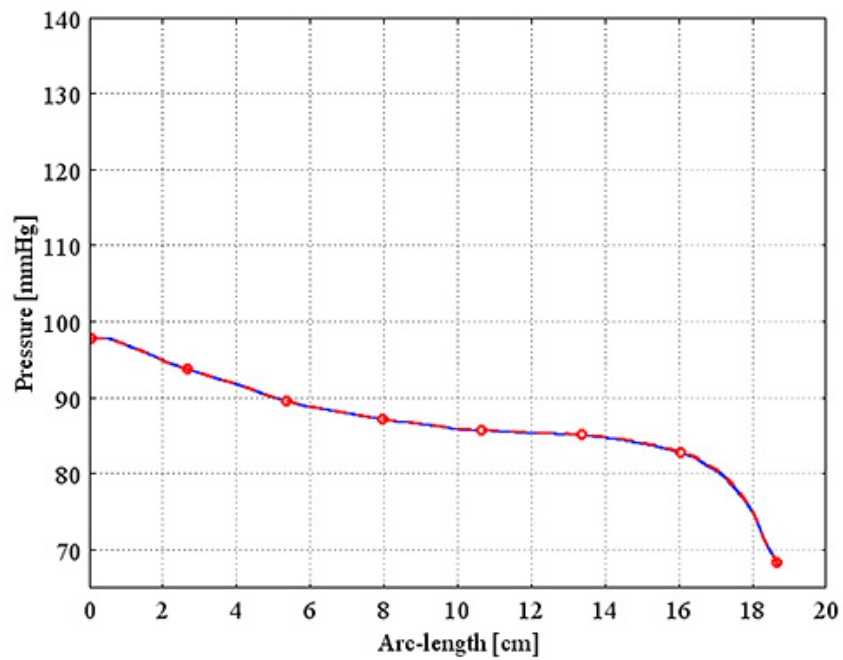
The comparison of wall shear stress on the RCA axis between the Newtonian and non-Newtonian models are presented in Figure 6.10. The results show that the wall shear stress of non-Newtonian model is about $1.4 - 3.3 \text{ dyne/cm}^2$ higher than the one of Newtonian model at the peak of systole. At the peak of diastole, the wall shear stress of non-Newtonian model is about $0.8 - 2.8 \text{ dyne/cm}^2$ higher than the one of Newtonian model. These results show the significance of non-Newtonian property of blood on the wall shear stress in the blood flow simulation.

6.3.3 Velocity Field

Figures 6.11, 6.12, and 6.13 show the comparison of velocity fields of the Newtonian and non-Newtonian models along the three investigated lines a_0a_1 , b_0b_1 , and c_0c_1 , respectively. The results show that at the three investigated lines, the non-Newtonian model has no significant effect on the velocity compared with the Newtonian model.

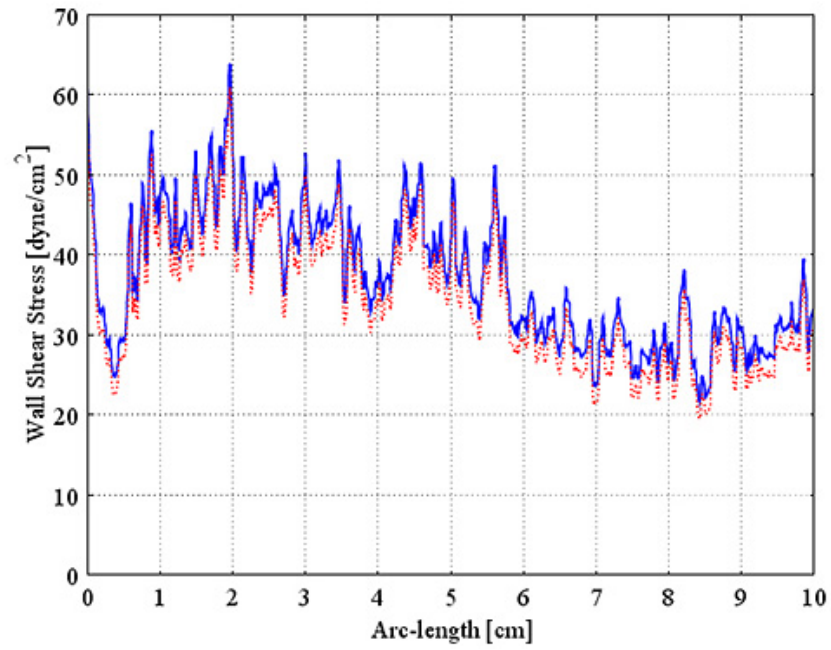


(a)

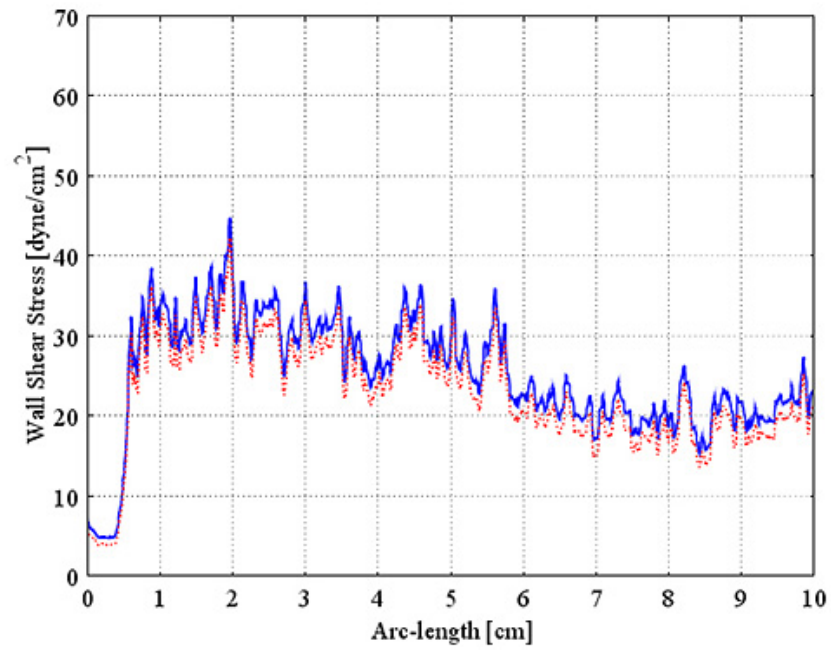


(b)

Figure 6.9: The pressure along the RCA axis obtained from the Newtonian model (dashed line with circle) and non-Newtonian model (solid line) at two different times: (a) at the peak of systole; and (b) at the peak of diastole.

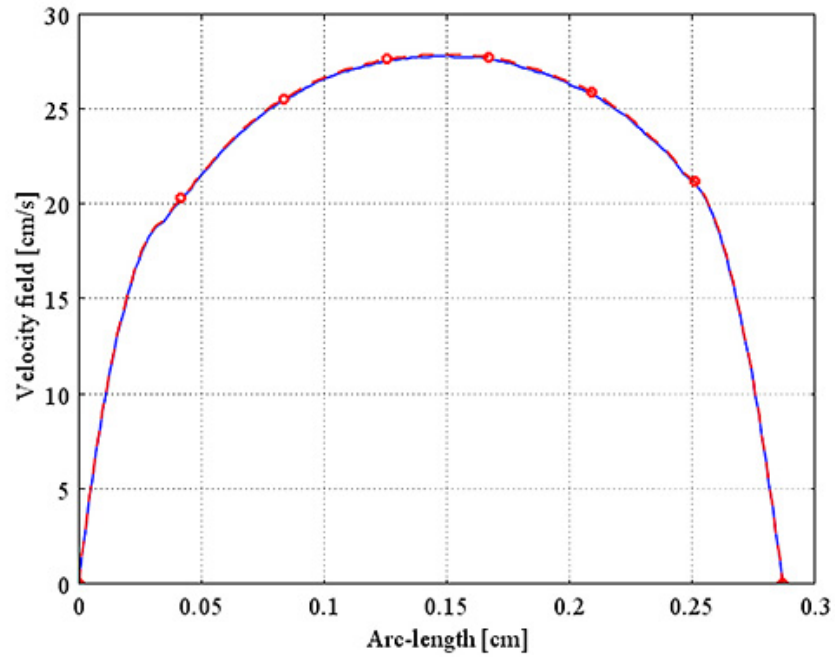


(a)

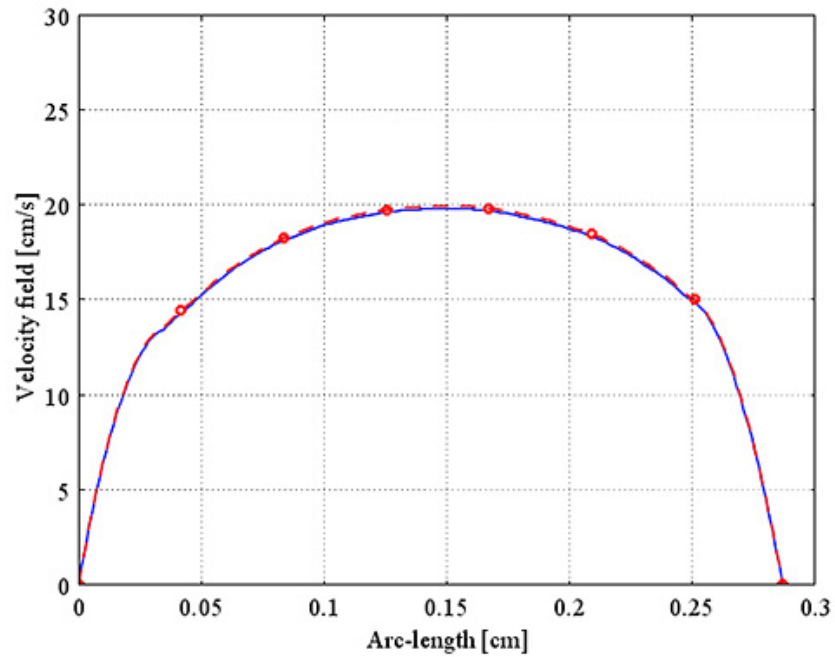


(b)

Figure 6.10: The wall shear stress along the RCA axis obtained from the Newtonian model (dotted line) and non-Newtonian model (solid line) at two different times: (a) at the peak of systole; and (b) at the peak of diastole.

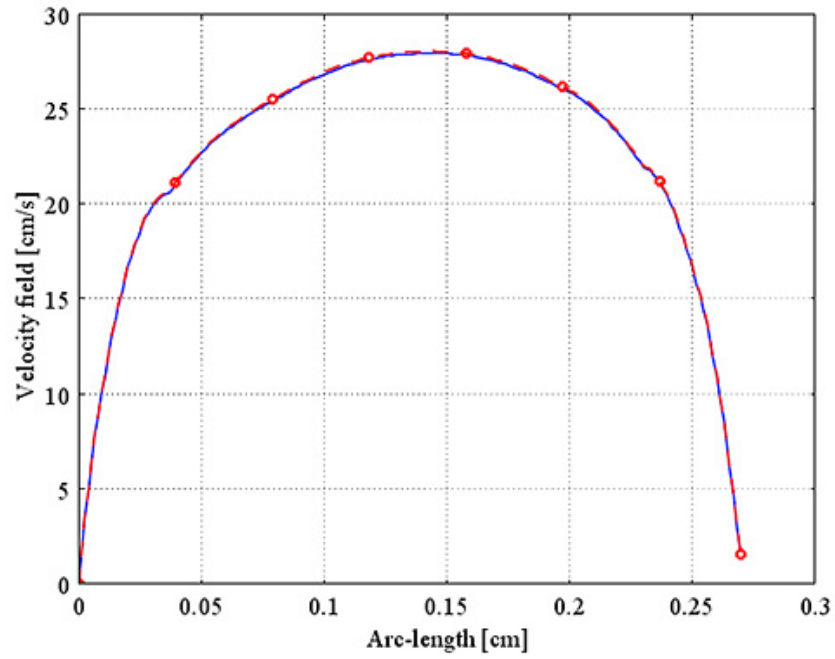


(a)

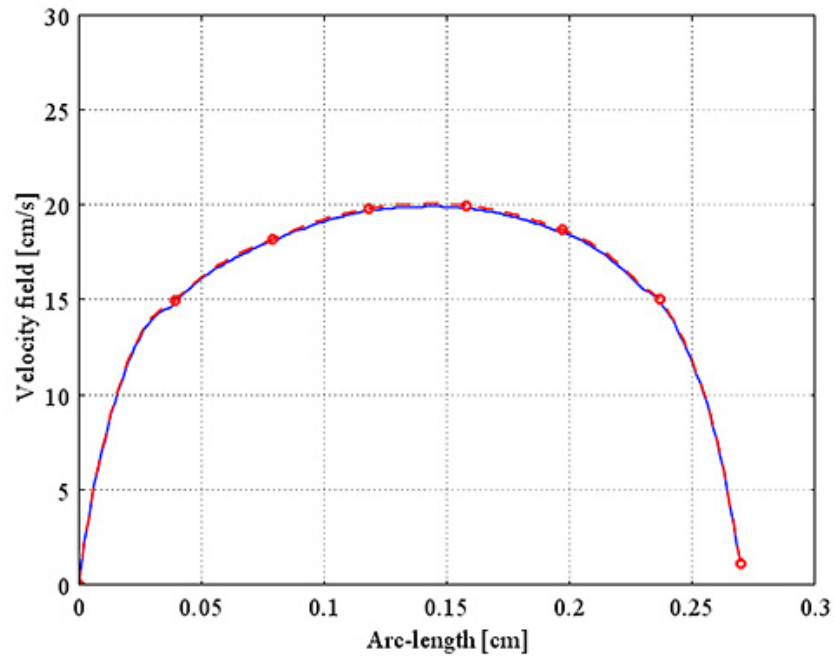


(b)

Figure 6.11: The maximal flow at investigated line a_0a_1 in plane A (Figure 6.8) obtained from the Newtonian model (dashed line with circle) and non-Newtonian model (solid line) at two different times: (a) at the peak of systole; and (b) at the peak of diastole.

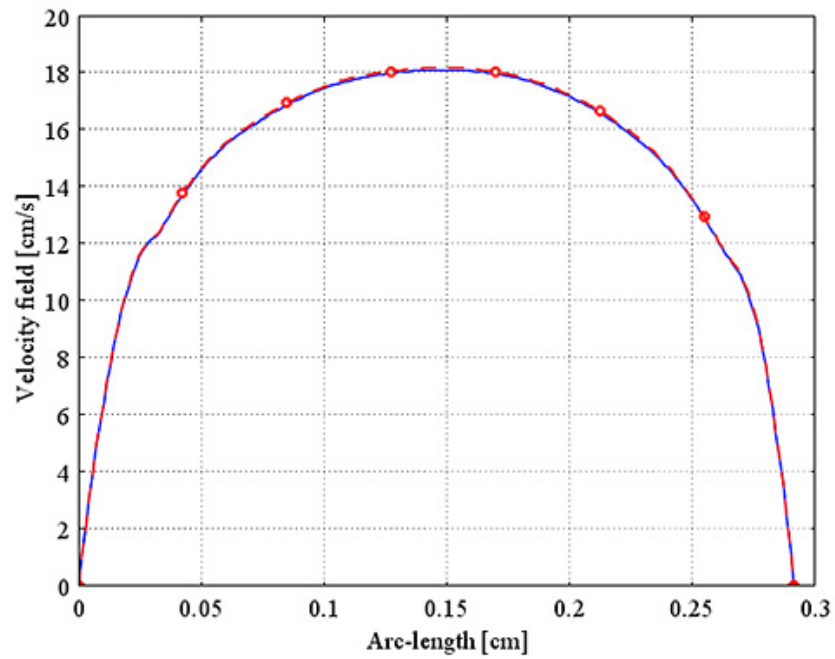


(a)

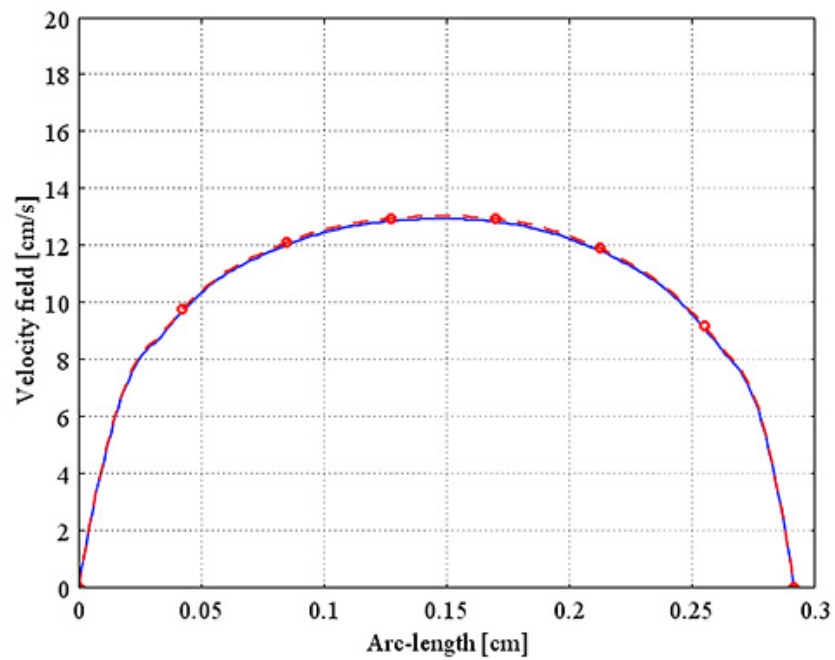


(b)

Figure 6.12: The maximal flow at investigated line b_0b_1 in plane B (Figure 6.8) obtained from the Newtonian model (dashed line with circle) and non-Newtonian model (solid line) at two different times: (a) at the peak of systole; and (b) at the peak of diastole.



(a)



(b)

Figure 6.13: The maximal flow at investigated line c_0c_1 in plane C (Figure 6.8) obtained from the Newtonian model (dashed line with circle) and non-Newtonian model (solid line) at two different times: (a) at the peak of systole; and (b) at the peak of diastole.

6.4 The Effect of Stenosis in a Human Coronary Artery

To investigate the effect of stenosis degree in the human coronary artery system, the three-dimension computational domains are used to simulate the flow of blood in the coronary artery system with 0%, 40%, 63%, and 72% stenosed RCA. The stenosis region is about 0.75 – 1.75 cm from the RCA inlet connected to the base of the aorta. Blood is assumed to be an incompressible non-Newtonian fluid based on Carreau's shear-thinning model. The numerical results and discussion are demonstrated in following subsections.

6.4.1 Pressure

The pressure along the RCA axis obtained from the domain with stenosed RCA having four different degrees of stenosis are presented in Figure 6.14. The numerical results, compared with the domain with 0% stenosed RCA, show that the blood pressure slightly drops around the stenosis region in the domain with 40% stenosed RCA and dramatically drops in the domain with 63% and 72% stenosed RCA. These can indicate that, at the stenosis region, the pressure drop is higher when the degree of stenosis is increased.

6.4.2 Wall Shear Stress

To determine the cause of critical flow in the system of coronary arteries, the shear stress on the wall of stenosed blood vessel is studied. The comparison of different stenosis degrees is investigated in shear stress on the blood wall. Figures 6.15 and 6.16 show the wall shear stress along the investigated RCA axis which is obtained from the domain with stenosed RCA having four different degrees of stenosis including 0%, 40%, 63%, and 72%. In the stenosis region, the results show that the wall shear stress increases when the stenosis degree increases (Figure 6.15). However, when we consider the flow of blood in the RCA after the blockage region, we can see that higher stenosis degree gives lower wall shear stress (Figure 6.16).

6.4.3 Velocity Field

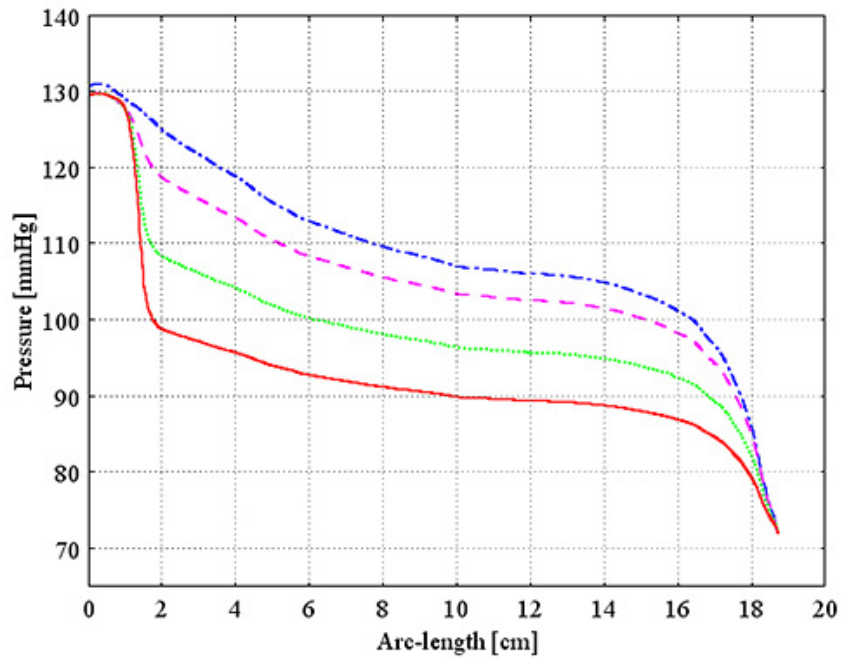
To look into the velocity profile of blood flow in the domain with stenosed RCA, the velocity field on three investigated lines (Figure 6.8) are investigated.

Figure 6.17 (a) and (b) show the velocity field at the peak of systole and the peak of diastole on the investigated line a_0a_2 in plane A of the domain with stenosed RCA having different degrees of stenosis: 0%, 40%, 63%, and 72%. At the peak of systole, the maximal velocities obtained from the domain with RCA stenosis including 0%, 40%, 63%, and 72%, are 28 cm/s, 42 cm/s, 59 cm/s, and 69 cm/s, respectively. Similarly, at the peak of diastole, the maximal velocities obtained from the domain with RCA stenosis: 0%, 40%, 63%, and 72%, are 20 cm/s, 30 cm/s, 43 cm/s, and 50 cm/s, respectively. The results obtained from the investigated line a_0a_2 indicate that the higher stenosis degree increases the velocity of blood in the stenosis region.

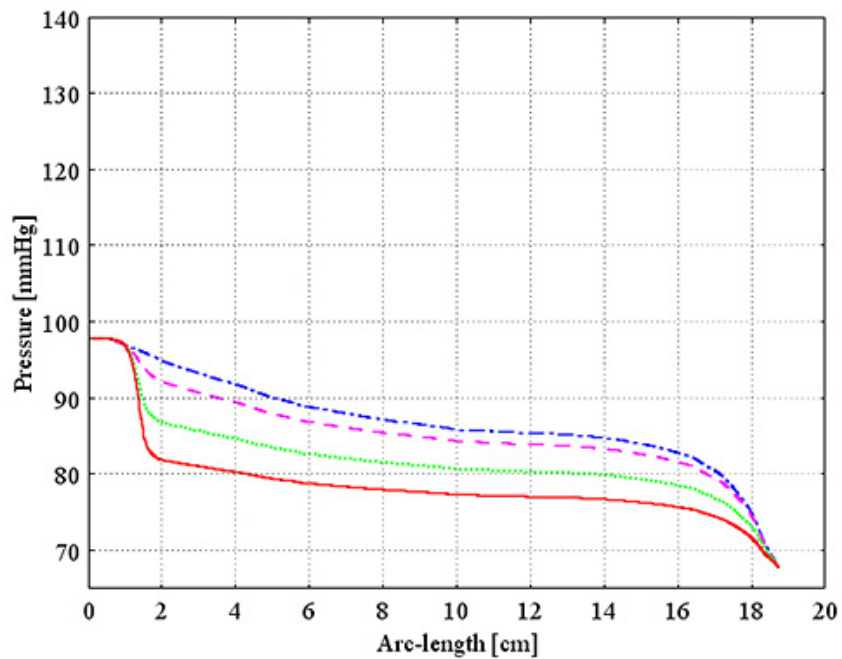
Figure 6.18 (a) and (b) present the velocity field at the peak of systole and the peak of diastole on the investigated line b_0b_2 in plane B of the domain with stenosed RCA having four different degrees of stenosis including 0%, 40%, 63%, and 72%. At the peak of systole, the maximal velocities obtained from the domain with RCA stenosis including 0%, 40%, 63%, and 72%, are 28 cm/s, 26 cm/s, 23 cm/s, and 20 cm/s, respectively. Similarly, at the peak of diastole, the maximal velocities obtained from the domain with RCA stenosis including 0%, 40%, 63%, and 72%, are 20 cm/s, 19 cm/s, 17 cm/s, and 14 cm/s, respectively.

Figure 6.19 (a) and (b) show the velocity field at the peak of systole and the peak of diastole on the investigated line c_0c_2 in plane C of the domain with stenosed RCA having different degrees of stenosis including 0%, 40%, 63%, and 72%. The results obtained from Figure 6.19 (a) and (b) are also similar to the results obtained from Figure 6.18 (a) and (b).

The results shown in Figure 6.18 and Figure 6.19 show that when the blood flows through the stenosed RCA, the velocity measured after stenosis region decreases with increasing of degree of stenosis .

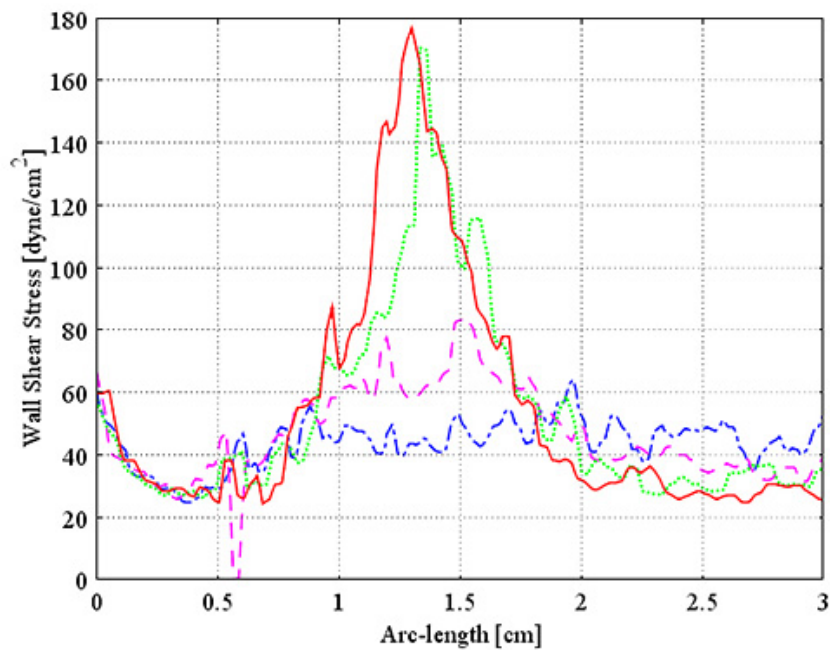


(a)

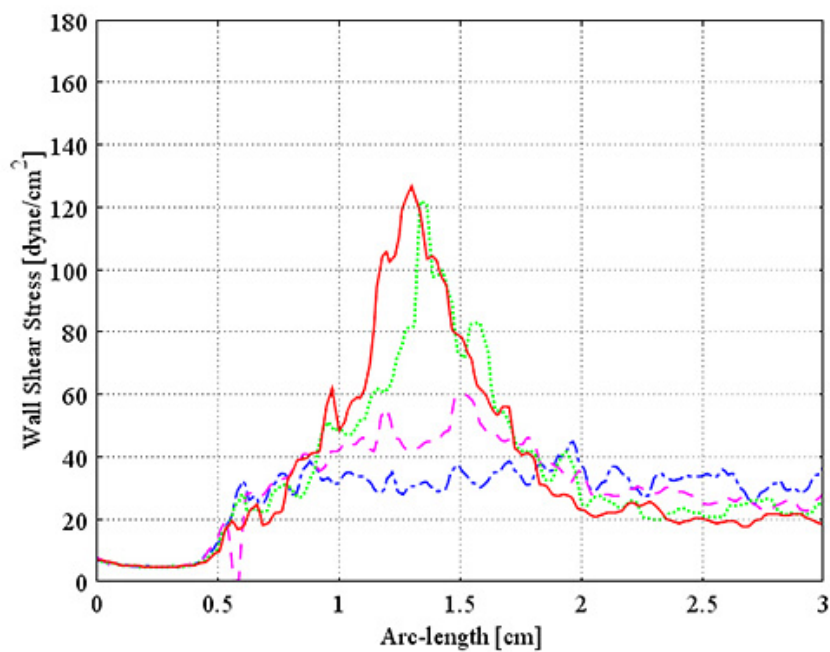


(b)

Figure 6.14: The pressure along the RCA axis obtained from the model with stenosed RCA having different degrees of stenosis including 0% (dash-dot line), 40% (dashed line), 63% (dotted line), and 72% (solid line), at two different times: (a) at the peak of systole; and (b) at the peak of diastole.

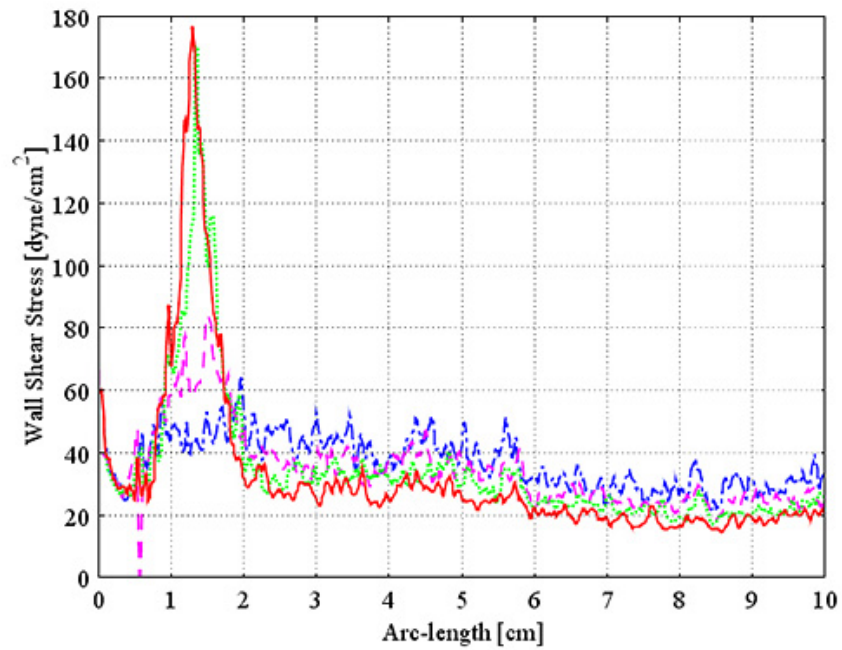


(a)

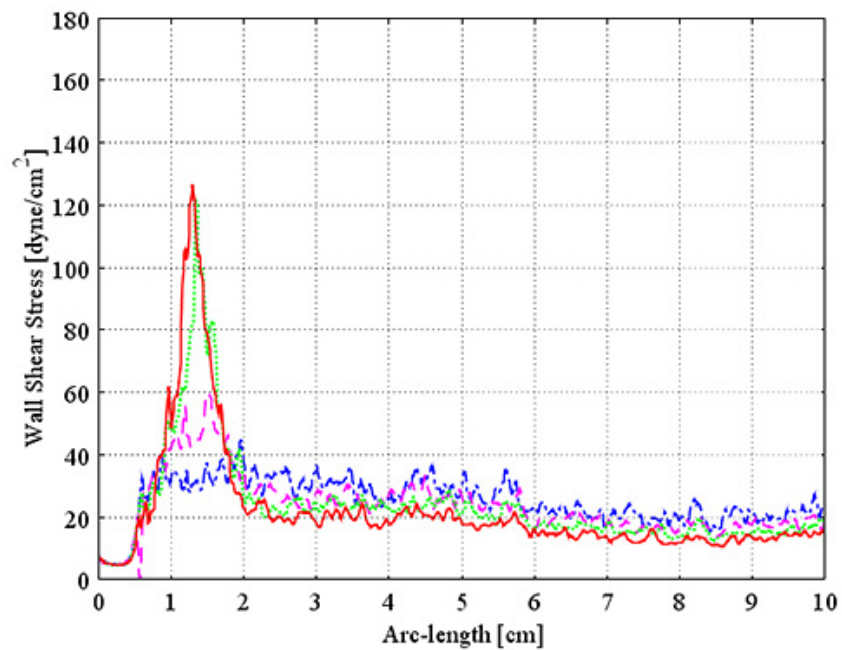


(b)

Figure 6.15: The wall shear stress along 3 cm of the RCA axis obtained from the model with stenosed RCA having different degrees of stenosis including 0% (dash-dot line), 40% (dashed line), 63% (dotted line), and 72% (solid line), at two different times: (a) at the peak of systole; and (b) at the peak of diastole.

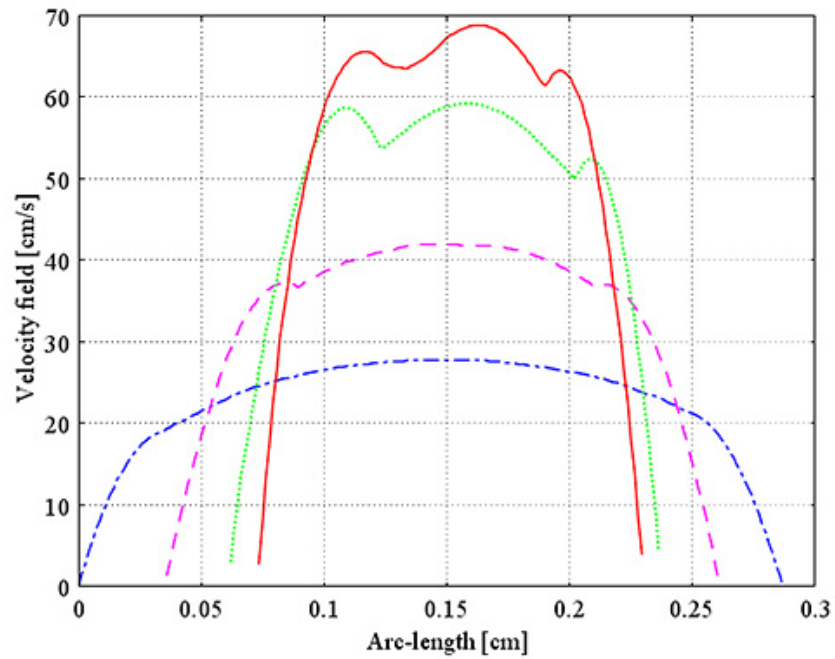


(a)

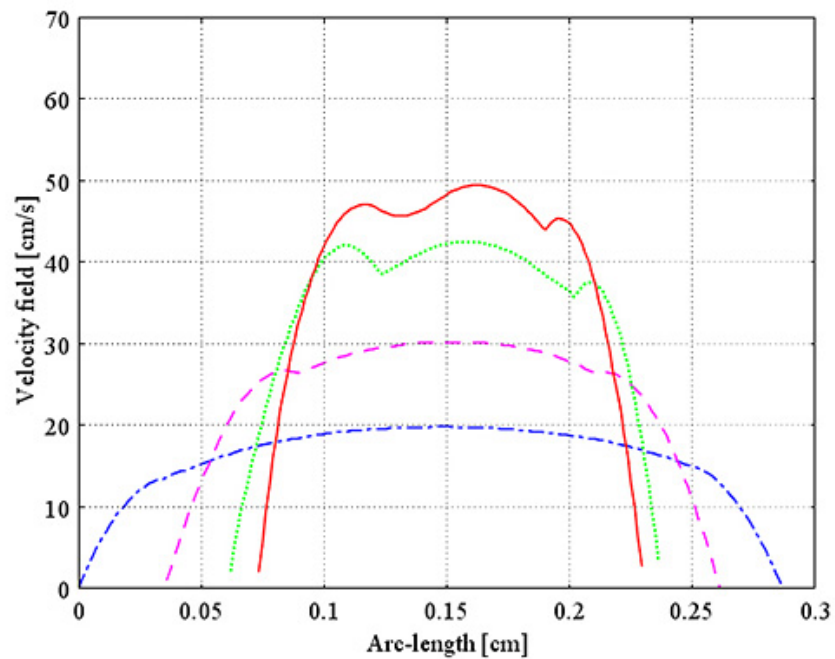


(b)

Figure 6.16: The wall shear stress along 10 cm of the RCA axis obtained from the model with stenosed RCA having different degrees of stenosis including 0% (dash-dot line), 40% (dashed line), 63% (dotted line), and 72% (solid line), at two different times: (a) at the peak of systole; and (b) at the peak of diastole.

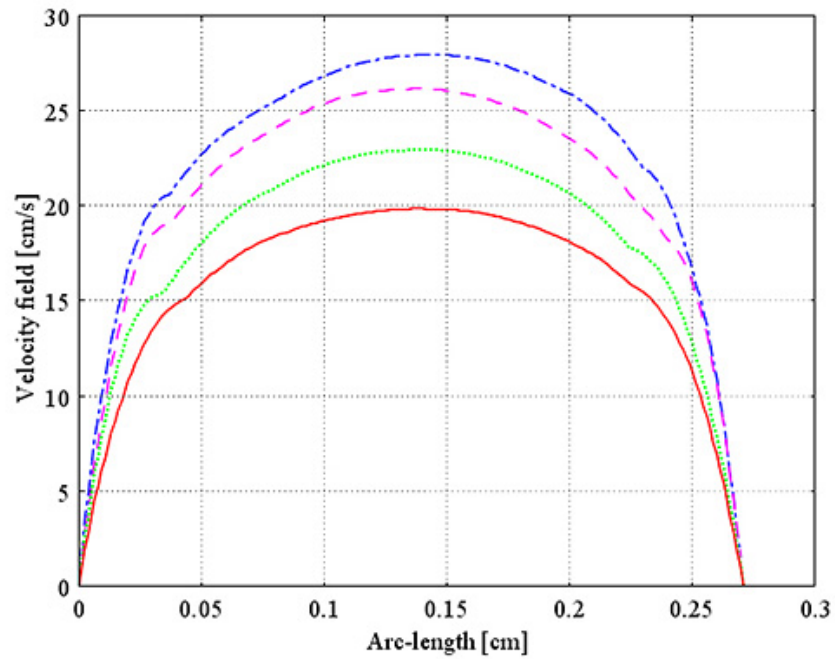


(a)

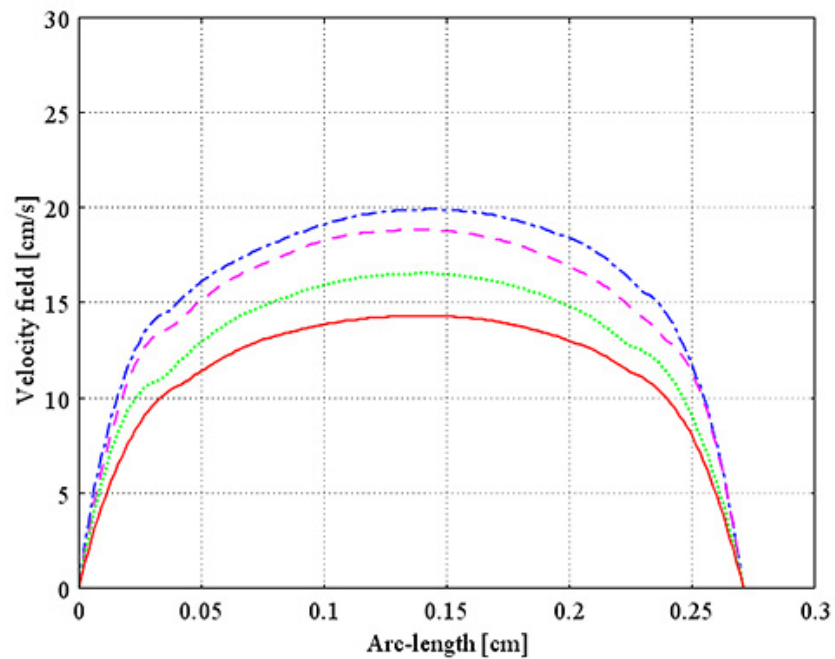


(b)

Figure 6.17: The maximal flow at investigated line a_0a_1 in plane A (Figure 6.8) obtained from the model with stenosed RCA having different degrees of stenosis including 0% (dash-dot line), 40% (dashed line), 63% (dotted line), and 72% (solid line), at two different times: (a) at the peak of systole; and (b) at the peak of diastole.

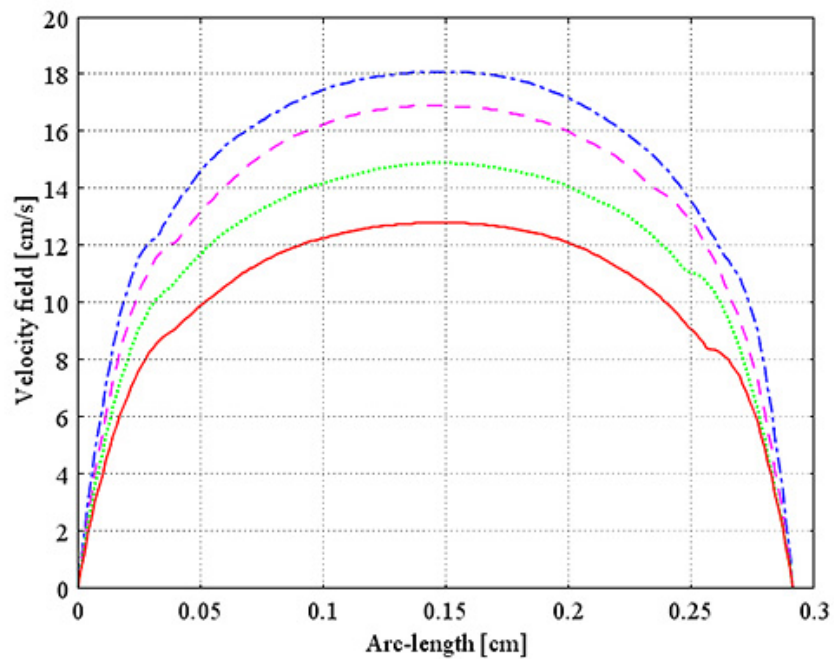


(a)

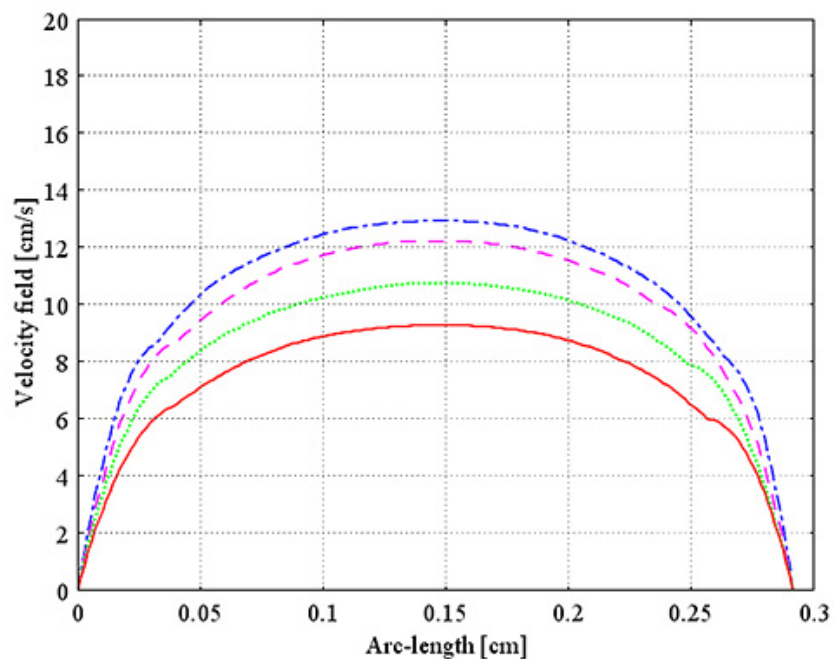


(b)

Figure 6.18: The maximal flow at investigated line b_0b_1 in plane B (Figure 6.8) obtained from the model with stenosed RCA having different degrees of stenosis including 0% (dash-dot line), 40% (dashed line), 63% (dotted line), and 72% (solid line), at two different times: (a) at the peak of systole; and (b) at the peak of diastole.



(a)



(b)

Figure 6.19: The maximal flow at investigated line c_0c_1 in plane C (Figure 6.8) obtained from the model with stenosed RCA having different degrees of stenosis including 0% (dash-dot line), 40% (dashed line), 63% (dotted line), and 72% (solid line), at two different times: (a) at the peak of systole; and (b) at the peak of diastole.

6.5 The Effect of Bypass Grafting in a Human Coronary Artery

To examine the effect of a bypass grafting in the human coronary artery system with four different stenosed RCA including 0%, 40%, 63%, and 72%, three-dimensional computational domains are used to simulate the flow of blood in the coronary artery system with a bypass graft. The distance of the graft connected to the RCA is about 7.5 – 8.0 cm from RCA inlet which is connected to the base of the aorta. Blood is assumed to be an incompressible non-Newtonian fluid based on Carreau's shear-thinning model. The results and discussions are presented in the following subsections.

6.5.1 Pressure

The pressure along the RCA axis obtained from the domain with no graft and with a bypass graft are presented in Figures 6.20 - 6.23. The results obtained from the domains with no graft compared with ones obtained from the domains with a bypass graft show that the bypass grafting can improve the pressure of blood along the RCA axis. However, in Figure 6.23 (a), there is a small drop of blood pressure in the stenosis region of the domain with 72% stenosed RCA.

6.5.2 Wall Shear Stress

Figures 6.24 - 6.27 show the wall shear stress along the investigated RCA axis obtained from the domains with no graft and with a bypass graft. The results obtained from domains with no graft compared with ones obtained from the domains with a bypass graft show that the bypass grafting can decrease the wall shear stress in the region between the RCA stenosis and the graft connected with RCA. However, when we consider the flow of blood in the stenosed RCA after the region of the graft connected with RCA, we can see that the wall shear stress obtained from the domain with a bypass graft is higher than the domain with no graft.

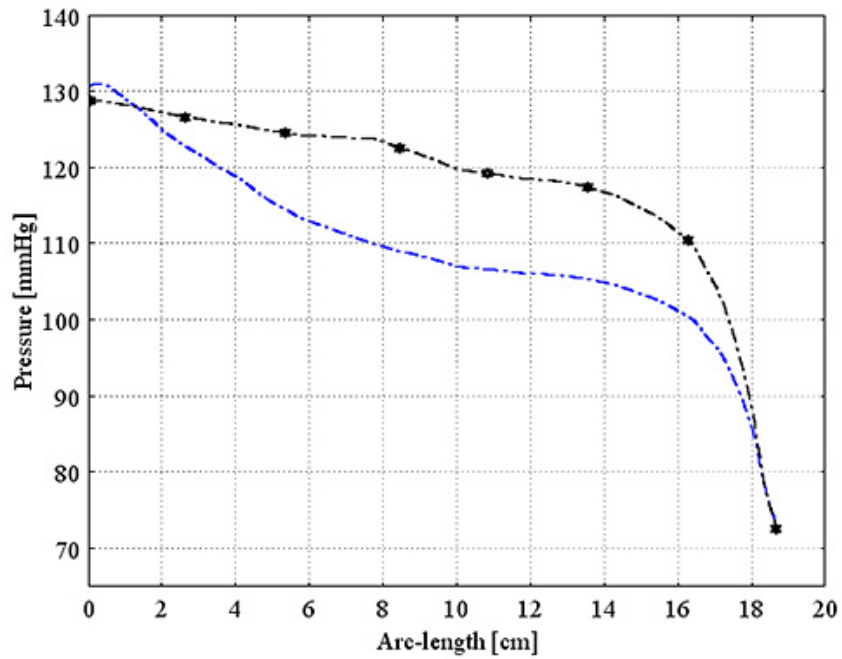
6.5.3 Velocity Field

To investigate the velocity profile of blood flow in the domain with no graft and with a bypass graft, the velocity field on the three investigated lines (Figure 6.8) obtained from the coronary artery system having four different stenosed RCA are investigated.

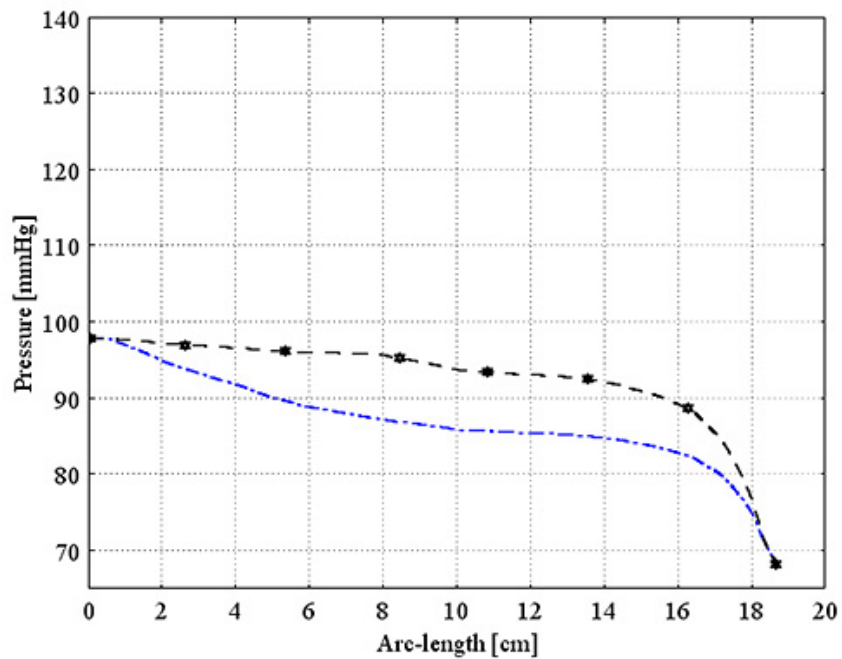
Figures 6.28 - 6.31 show the velocity field obtained from the domains with no graft and with a bypass on the investigated line a_0a_2 in plane A of the domain with four different stenosed RCA including 0%, 40%, 63%, and 72%. The results indicate that the bypass grafting decreases the blood velocity in the stenosis region.

Figures 6.32 - 6.35 present the velocity field obtained from the domains with no graft and with a bypass on the investigated line b_0b_2 in plane B of the domain with four different stenosed RCA including 0%, 40%, 63%, and 72%. The results indicate that the bypass grafting decreases the blood velocity in the region between the stenosis site and the graft connected to the RCA.

Figures 6.36 - 6.39 show the velocity field obtained from the domains with no graft and with a bypass on the investigated line c_0c_2 in plane C of the domain with four different stenosed RCA including 0%, 40%, 63%, and 72%. The results indicate that when the blood flows through the stenosed RCA with a graft, the mean velocity below region of the graft connected to the RCA increases.

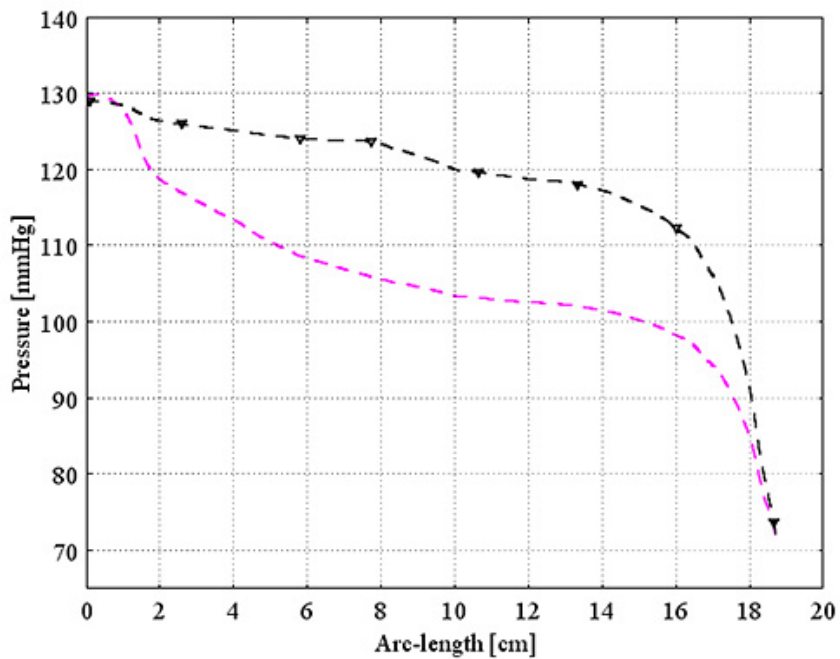


(a)

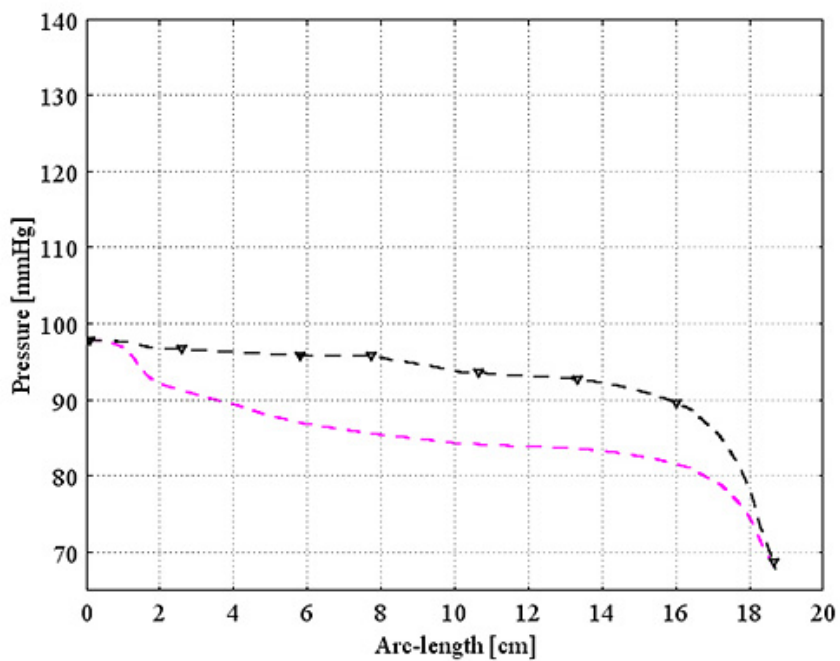


(b)

Figure 6.20: The pressure along the RCA axis obtained from the model having 0% stenosed RCA with no graft (dash-dot line) and with a bypass graft (dash-dot line with star), at two different times: (a) at the peak of systole; and (b) at the peak of diastole.

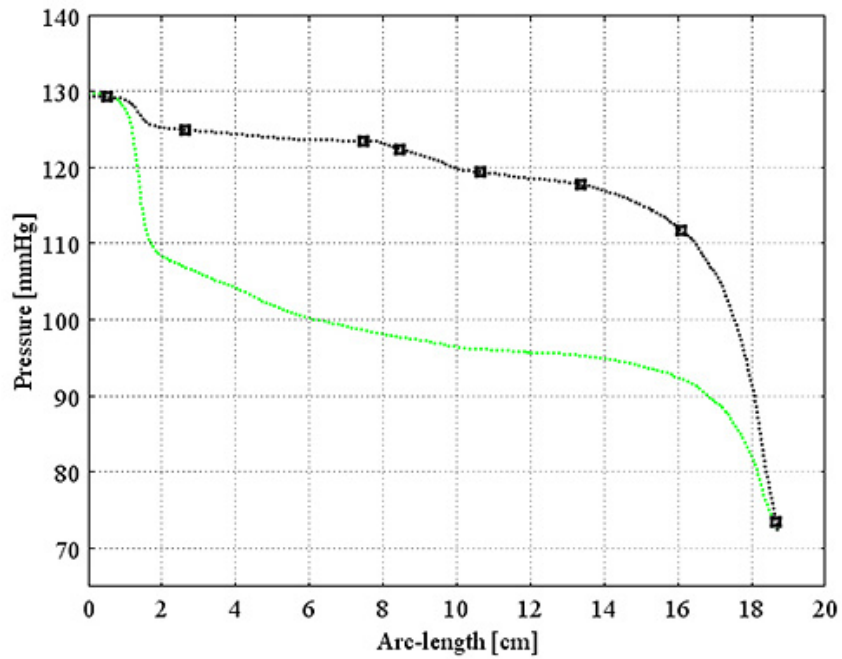


(a)

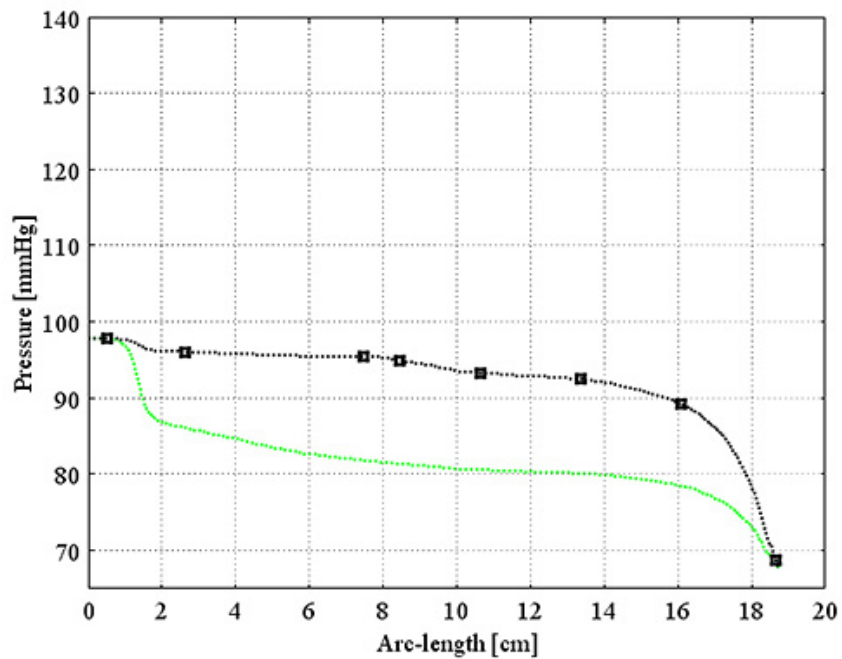


(b)

Figure 6.21: The pressure along the RCA axis obtained from the model having 40% stenosed RCA with no graft (dashed line) and with a bypass graft (dashed line with triangle), at two different times: (a) at the peak of systole; and (b) at the peak of diastole.

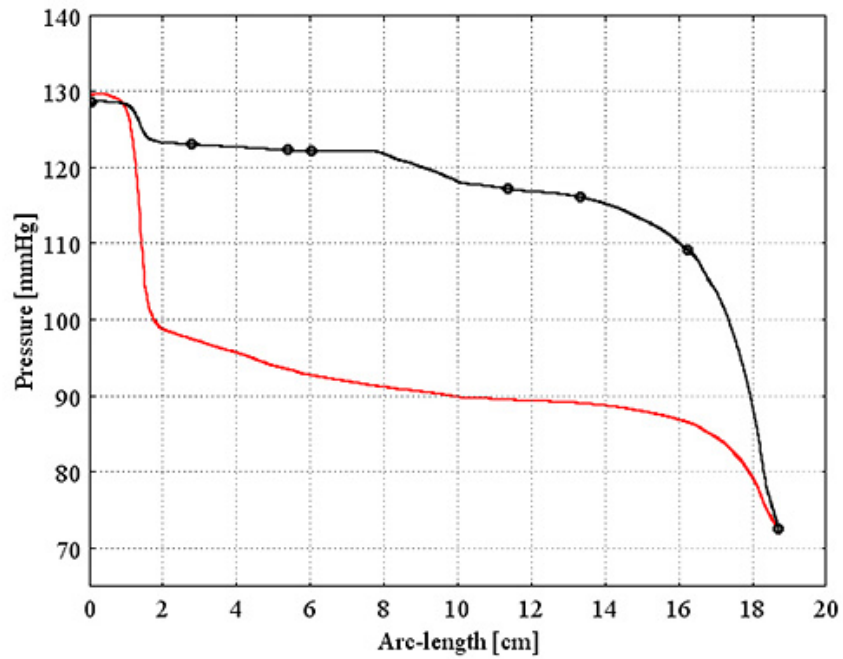


(a)

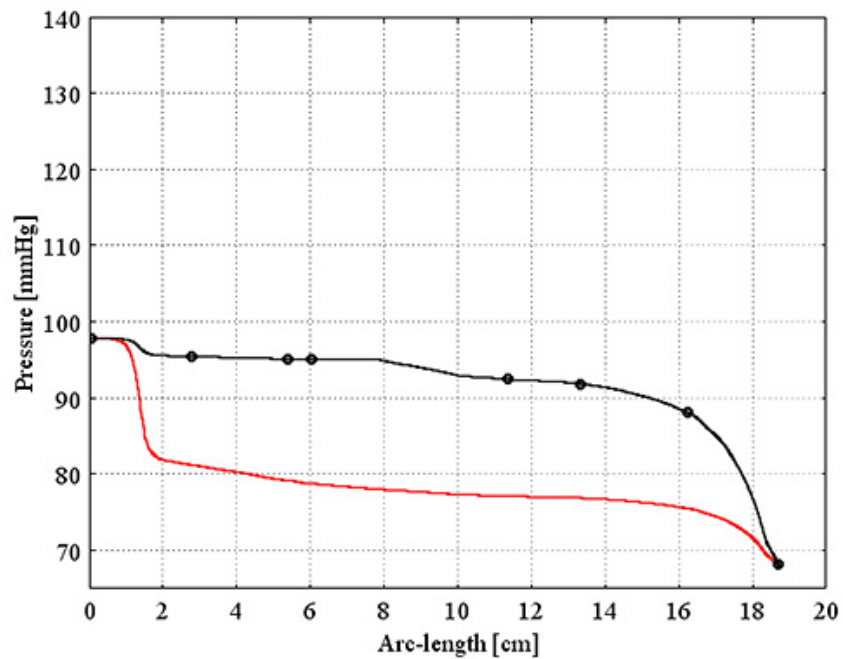


(b)

Figure 6.22: The pressure along the RCA axis obtained from the model having 63% stenosed RCA with no graft (dotted line) and with a bypass graft (dotted line with square), at two different times: (a) at the peak of systole; and (b) at the peak of diastole.

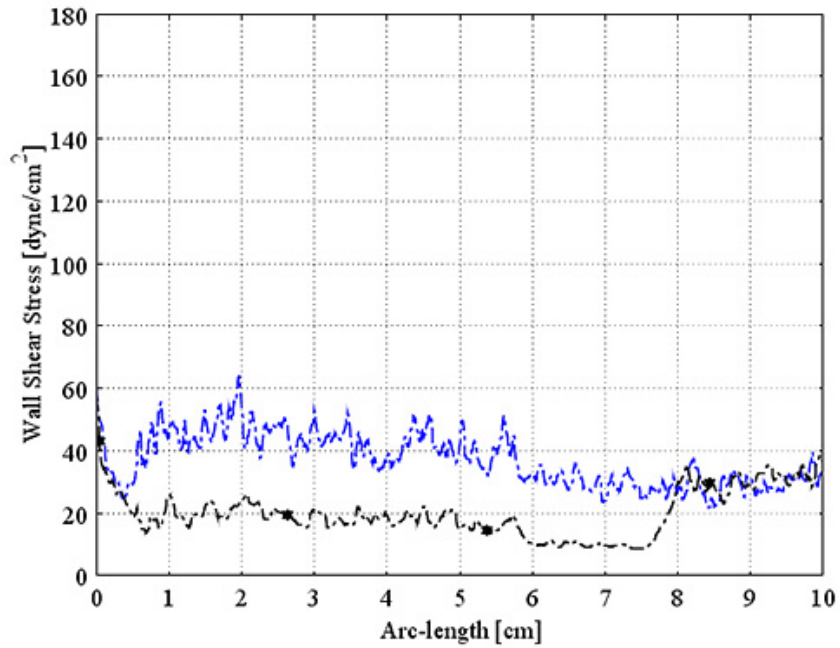


(a)

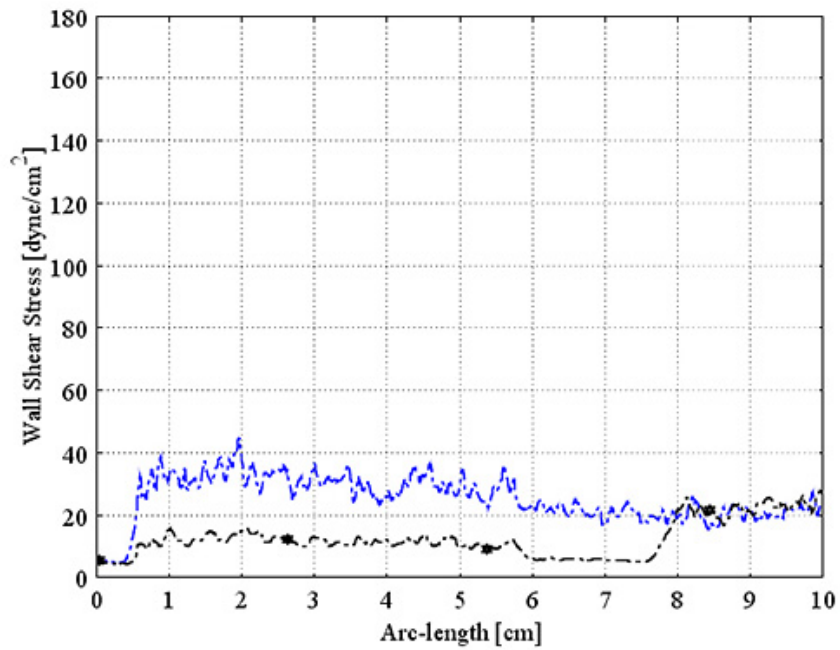


(b)

Figure 6.23: The pressure along the RCA axis obtained from the model having 72% stenosed RCA with no graft (solid line) and with a bypass graft (solid line with circle), at two different times: (a) at the peak of systole; and (b) at the peak of diastole.

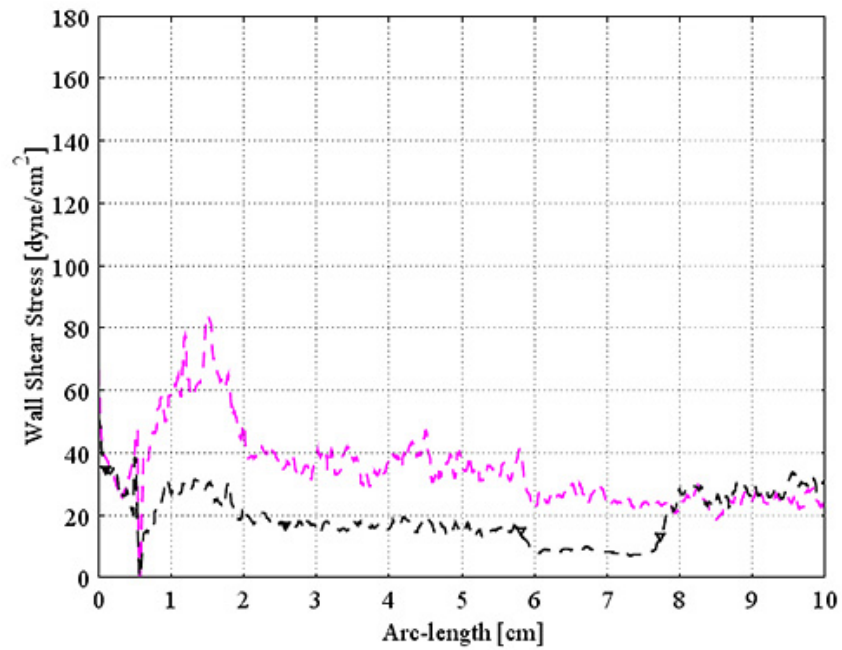


(a)

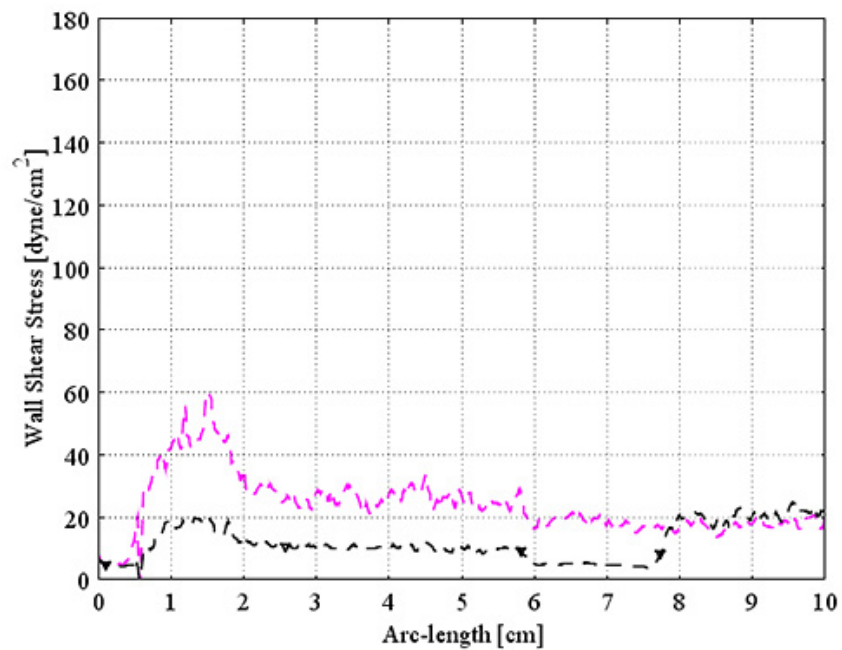


(b)

Figure 6.24: The wall shear stress along 10 cm of the RCA axis obtained from the model having 0% stenosed RCA with no graft (dash-dot line) and with a bypass graft (dash-dot line with star), at two different times: (a) at the peak of systole; and (b) at the peak of diastole.

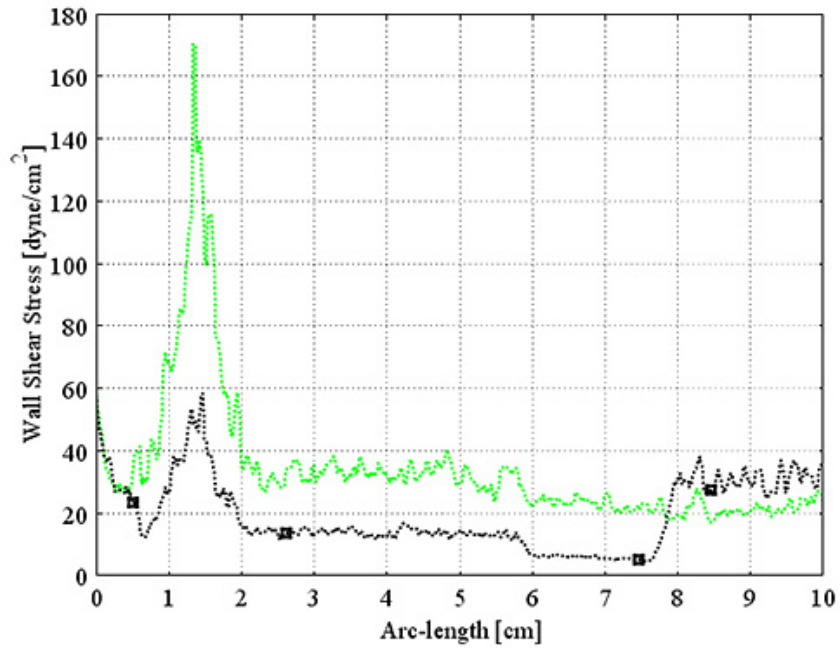


(a)

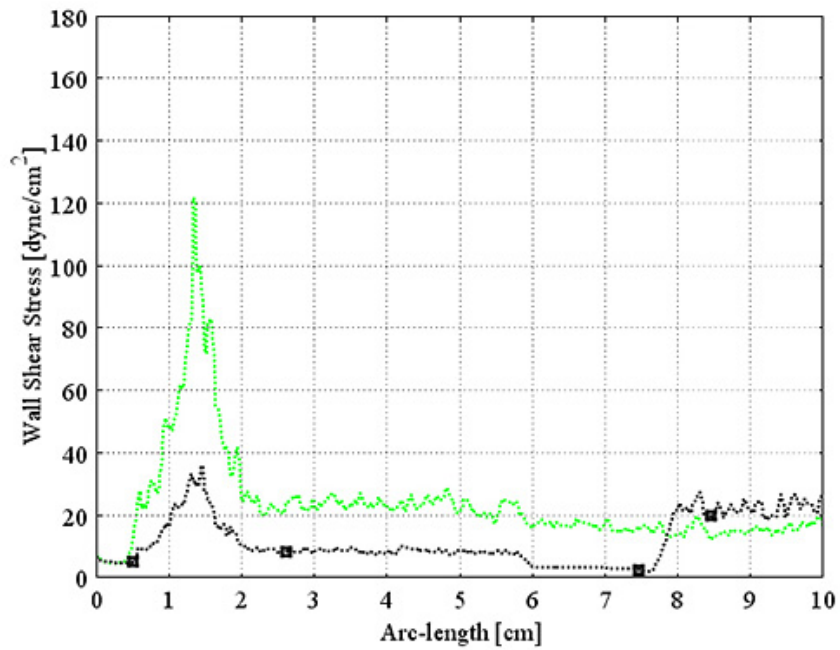


(b)

Figure 6.25: The wall shear stress along 10 cm of the RCA axis obtained from the model having 40% stenosed RCA with no graft (dashed line) and with a bypass graft (dashed line with triangle), at two different times: (a) at the peak of systole; and (b) at the peak of diastole.

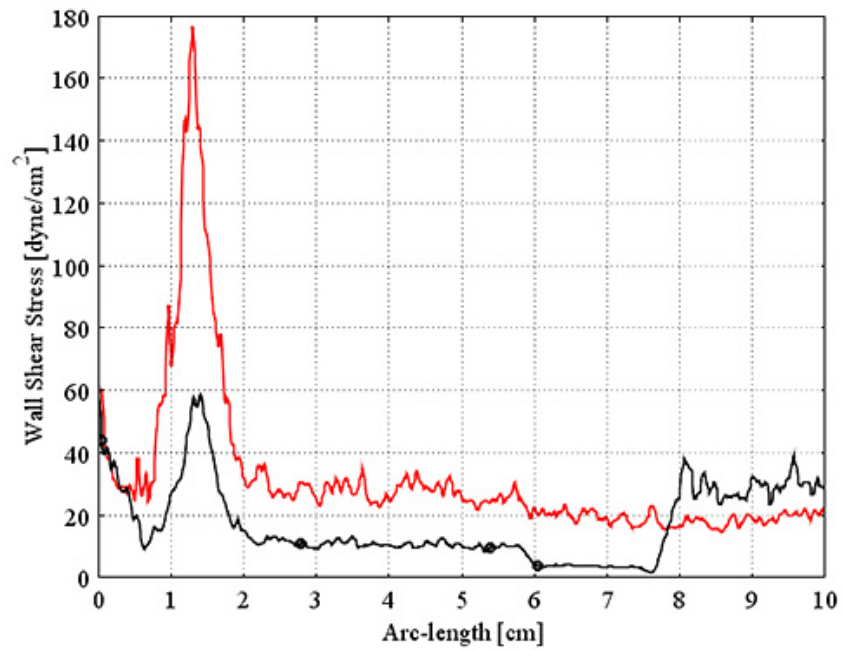


(a)

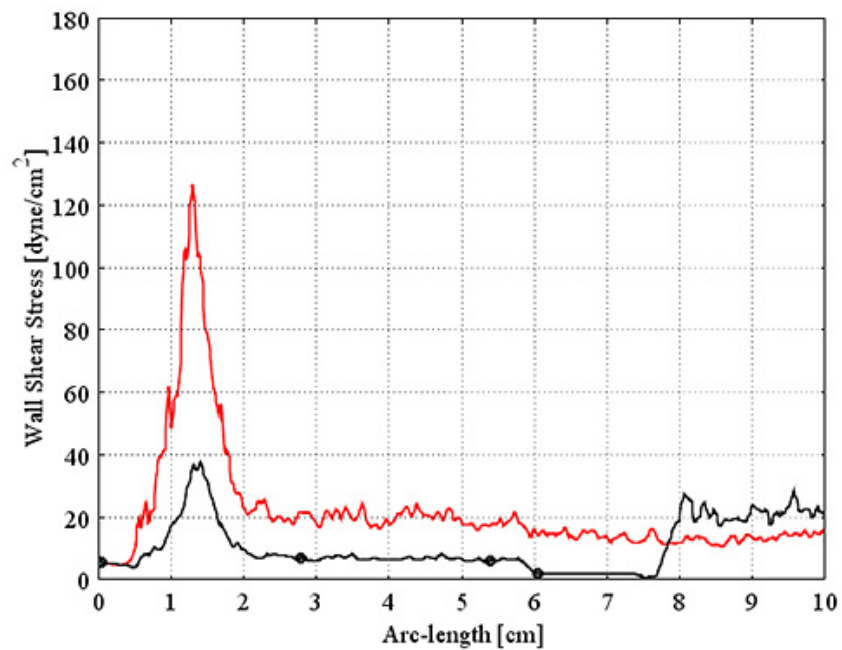


(b)

Figure 6.26: The wall shear stress along 10 cm of the RCA axis obtained from the model having 63% stenosed RCA with no graft (dotted line) and with a bypass graft (dotted line with square), at two different times: (a) at the peak of systole; and (b) at the peak of diastole.

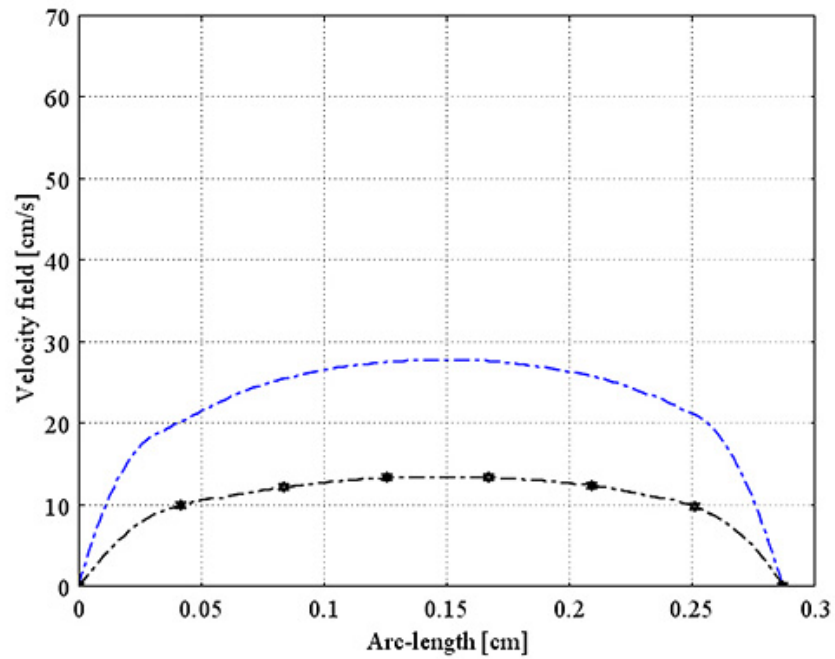


(a)

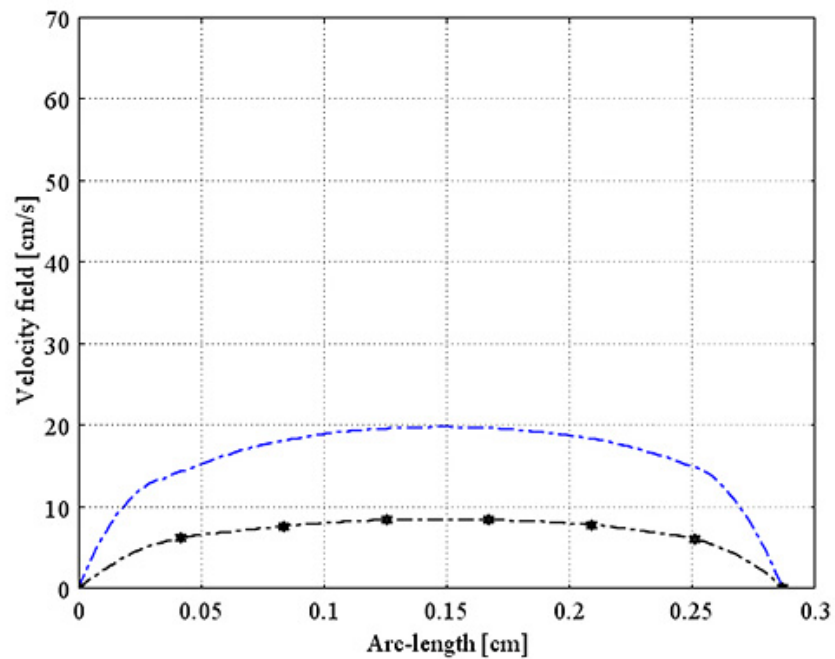


(b)

Figure 6.27: The wall shear stress along 10 cm of the RCA axis obtained from the model having 72% stenosed RCA with no graft (solid line) and with a bypass graft (solid line with circle), at two different times: (a) at the peak of systole; and (b) at the peak of diastole.

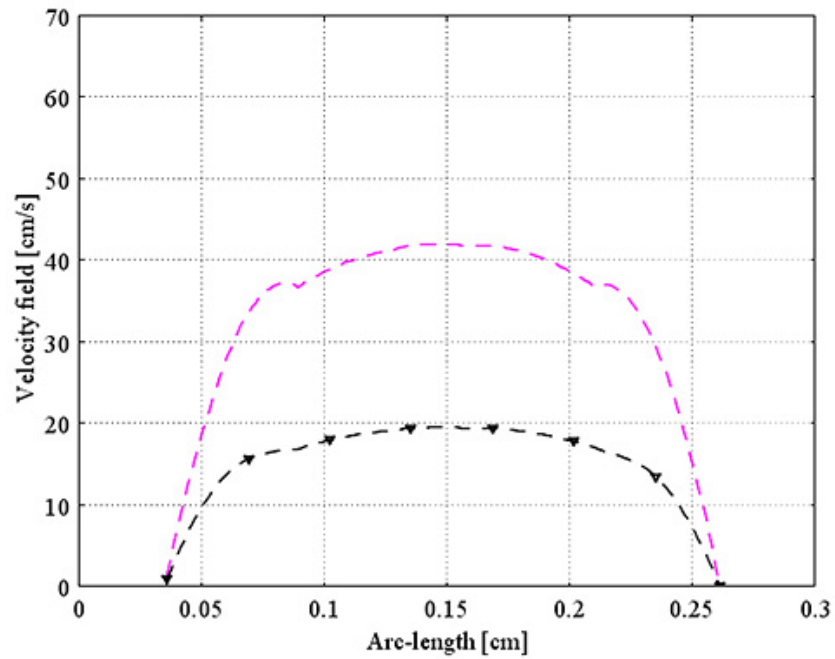


(a)

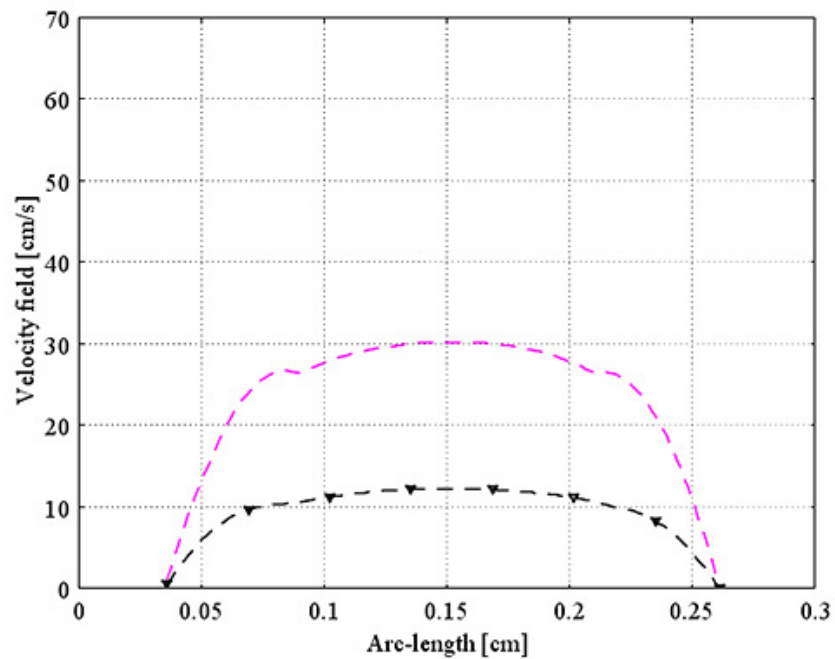


(b)

Figure 6.28: The maximal flow at investigated line a_0a_1 in plane A (Figure 6.8) obtained from the model having 0% stenosed RCA with no graft (dash-dot line) and with a bypass graft (dash-dot line with star), at two different times: (a) at the peak of systole; and (b) at the peak of diastole.

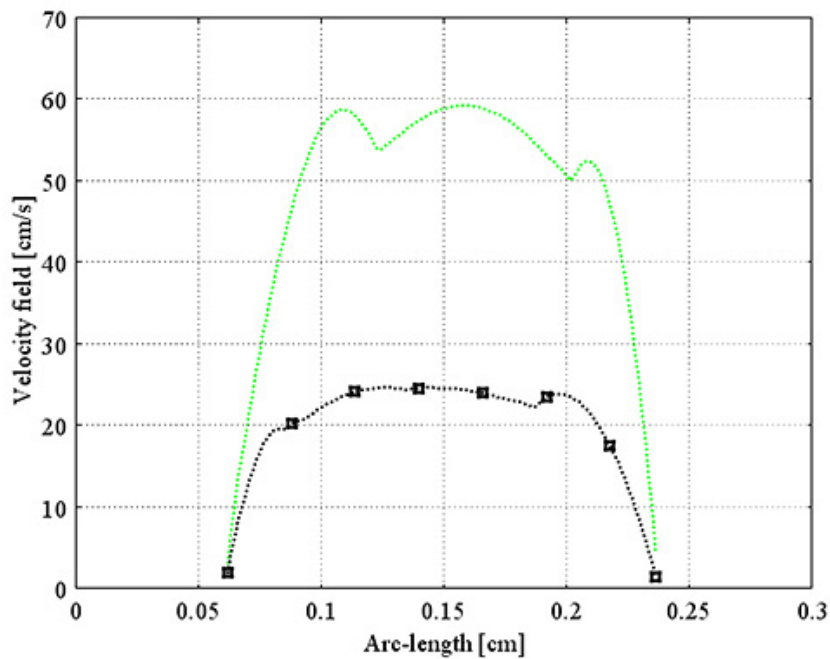


(a)

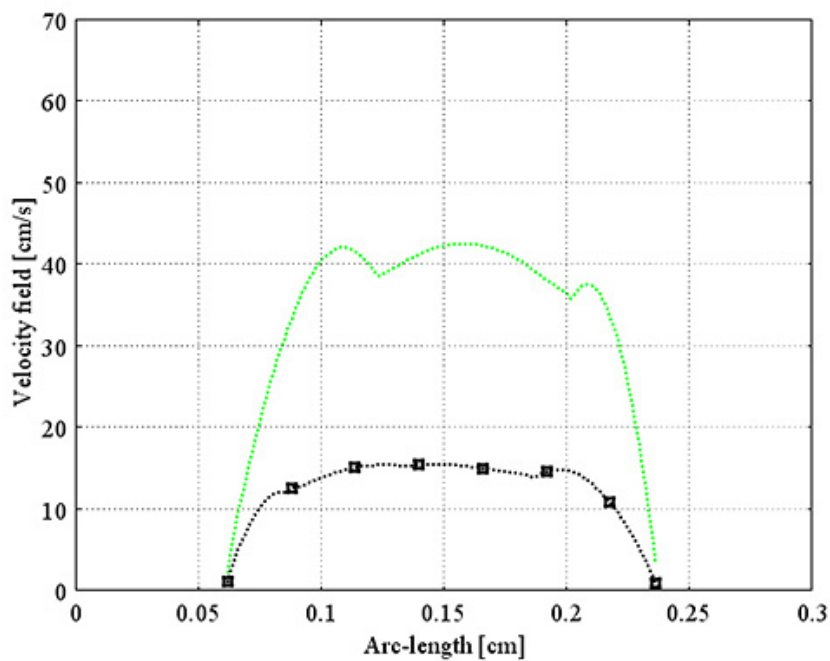


(b)

Figure 6.29: The maximal flow at investigated line a_0a_1 in plane A (Figure 6.8) obtained from the model having 40% stenosed RCA with no graft (dashed line) and with a bypass graft (dashed line with triangle), at two different times: (a) at the peak of systole; and (b) at the peak of diastole.

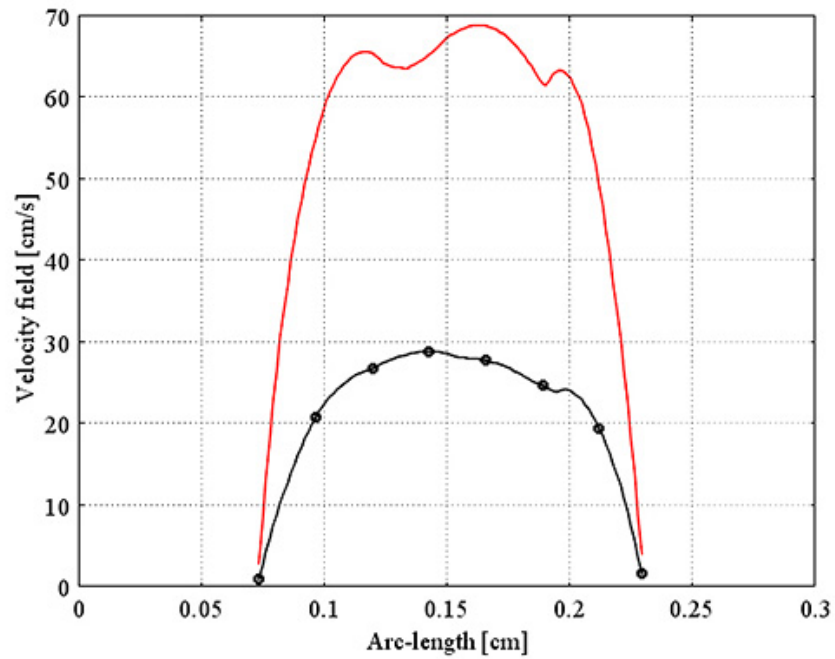


(a)

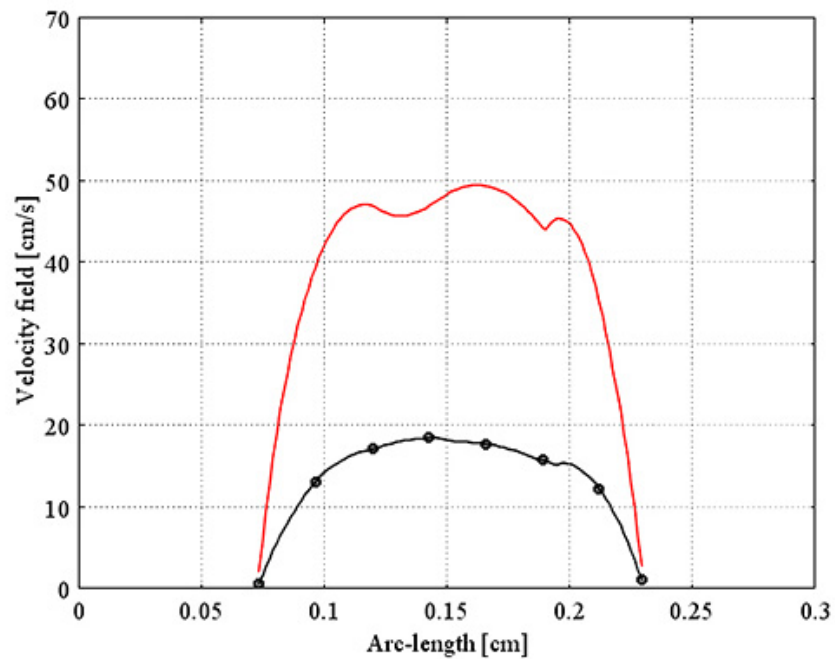


(b)

Figure 6.30: The maximal flow at investigated line a_0a_1 in plane A (Figure 6.8) obtained from the model having 63% stenosed RCA with no graft (dotted line) and with a bypass graft (dotted line with square), at two different times: (a) at the peak of systole; and (b) at the peak of diastole.

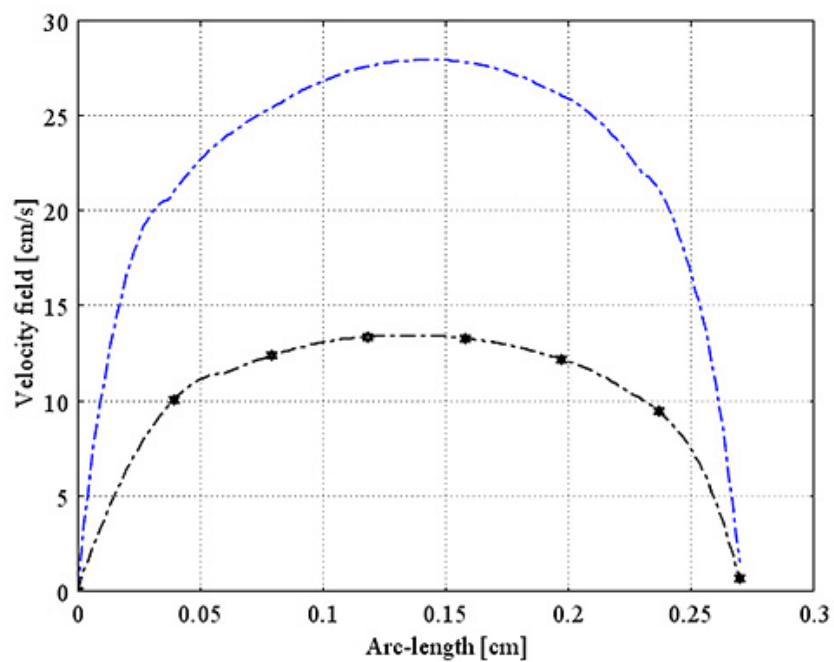


(a)

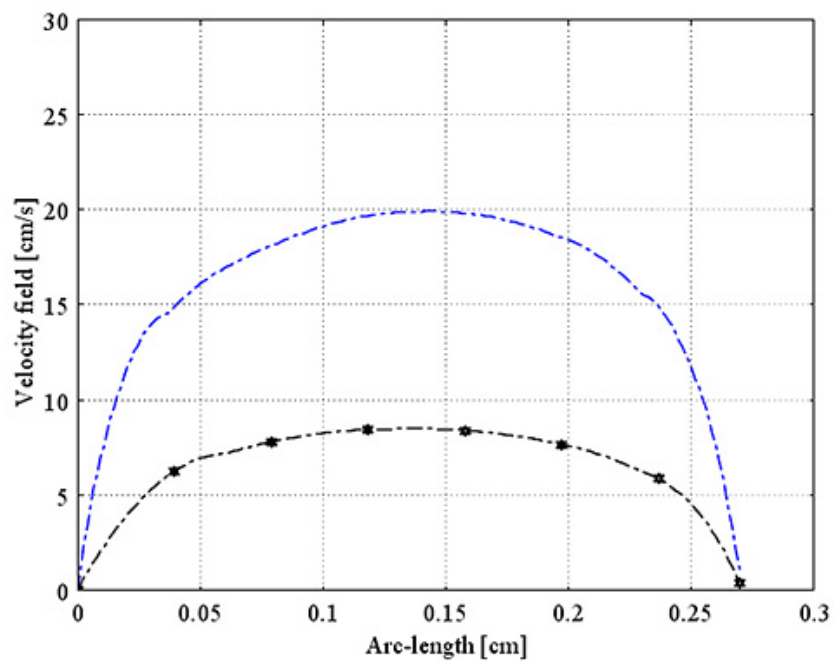


(b)

Figure 6.31: The maximal flow at investigated line a_0a_1 in plane A (Figure 6.8) obtained from the model having 72% stenosed RCA with no graft (solid line) and with a bypass graft (solid line with circle), at two different times: (a) at the peak of systole; and (b) at the peak of diastole.

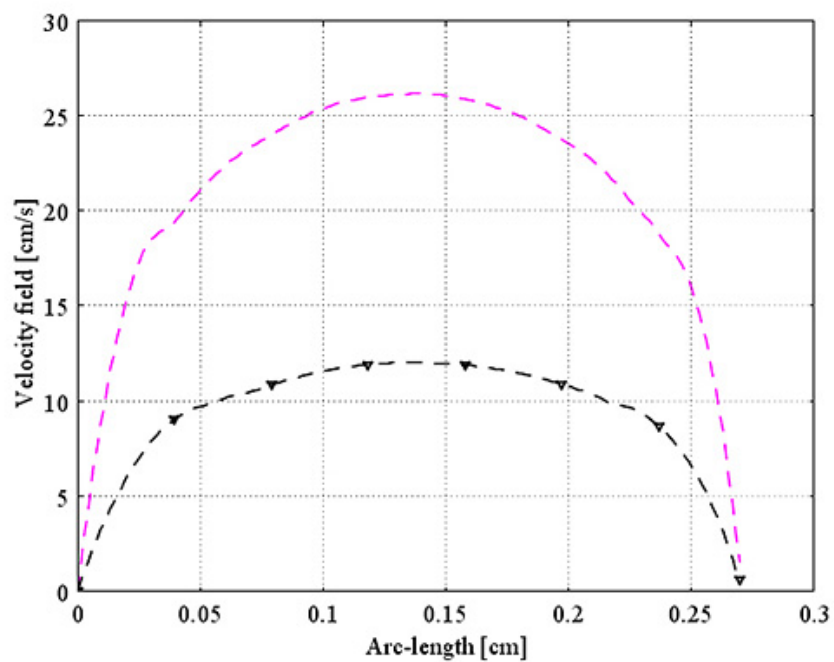


(a)

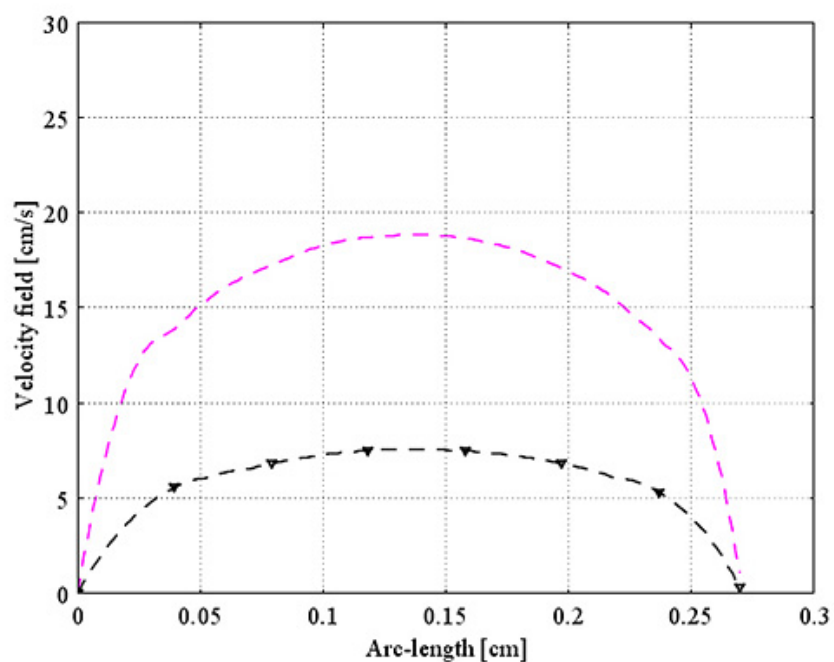


(b)

Figure 6.32: The maximal flow at investigated line b_0b_1 in plane B (Figure 6.8) obtained from the model having 0% stenosed RCA with no graft (dash-dot line) and with a bypass graft (dash-dot line with star), at two different times: (a) at the peak of systole; and (b) at the peak of diastole.

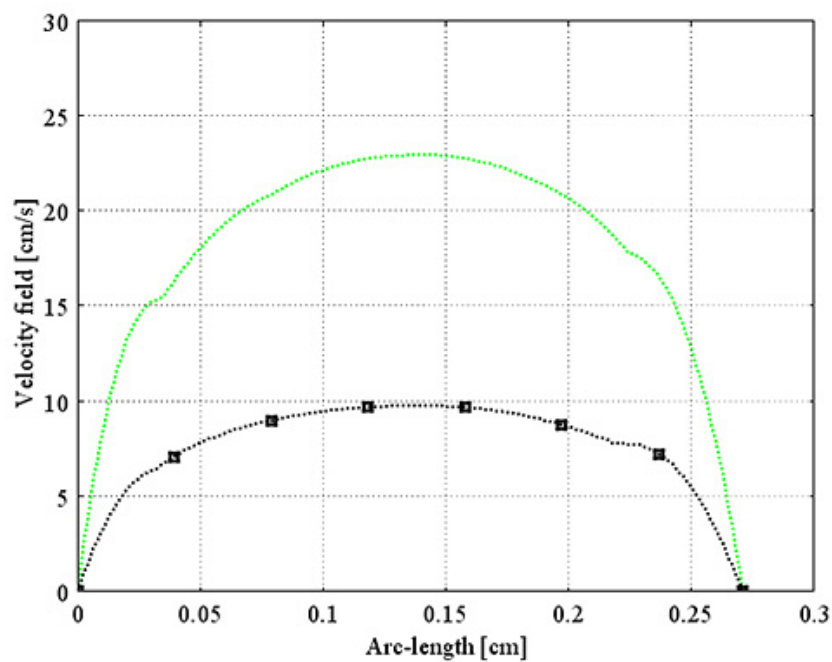


(a)

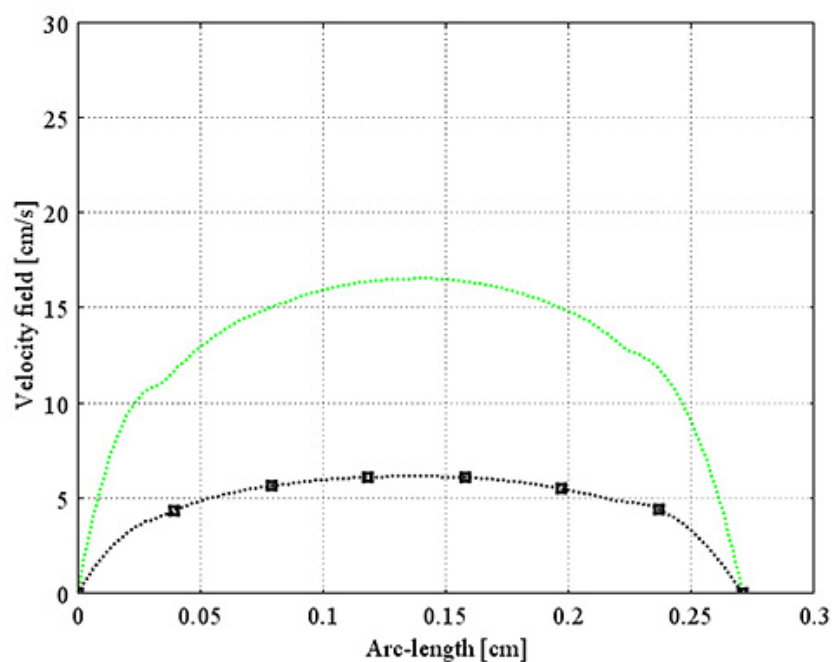


(b)

Figure 6.33: The maximal flow at investigated line b_0b_1 in plane B (Figure 6.8) obtained from the model having 40% stenosed RCA with no graft (dashed line) and with a bypass graft (dashed line with triangle), at two different times: (a) at the peak of systole; and (b) at the peak of diastole.

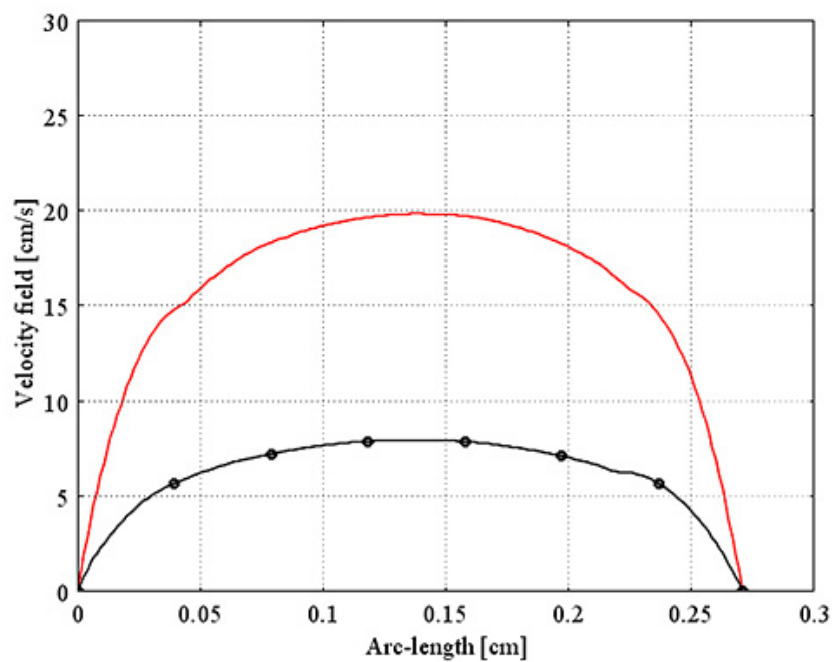


(a)

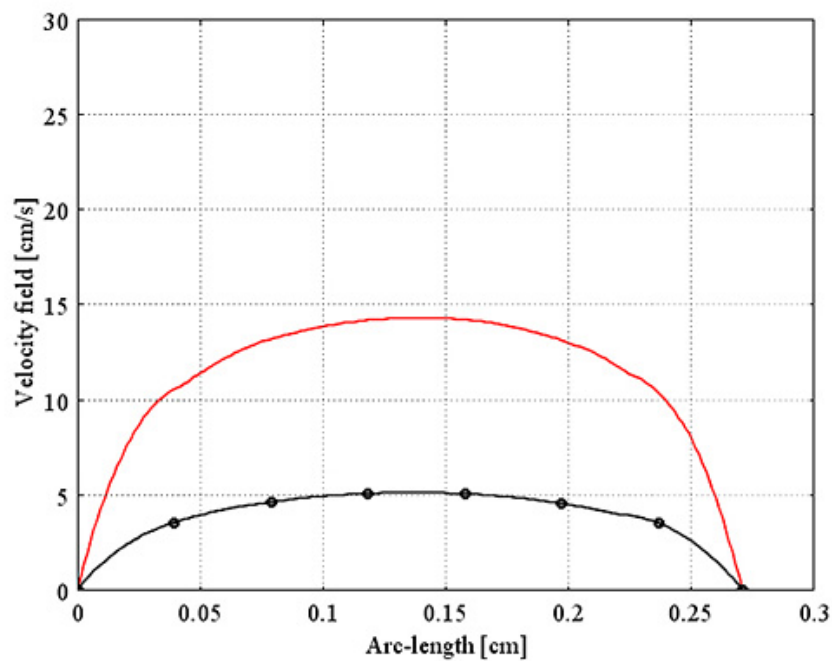


(b)

Figure 6.34: The maximal flow at investigated line b_0b_1 in plane B (Figure 6.8) obtained from the model having 63% stenosed RCA with no graft (dotted line) and with a bypass graft (dotted line with square), at two different times: (a) at the peak of systole; and (b) at the peak of diastole.

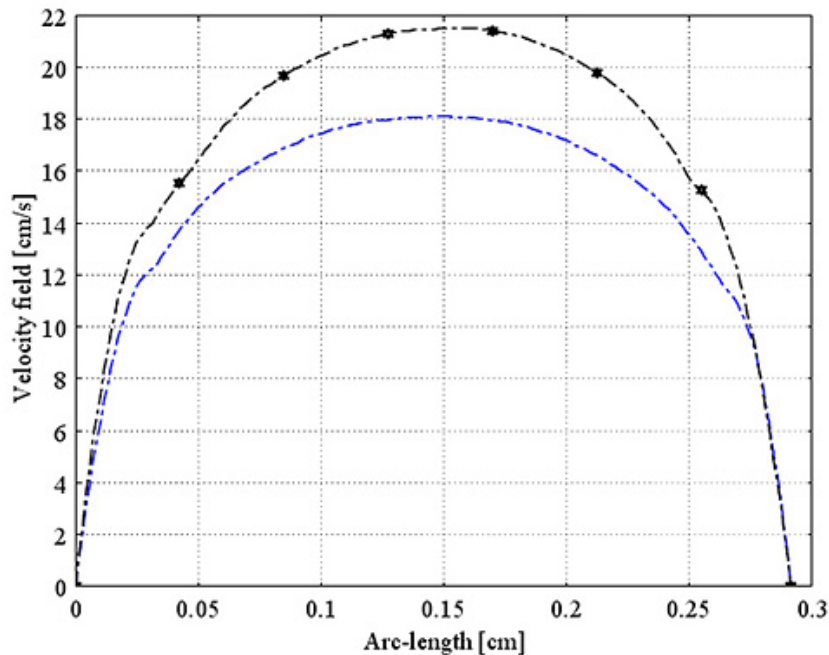


(a)

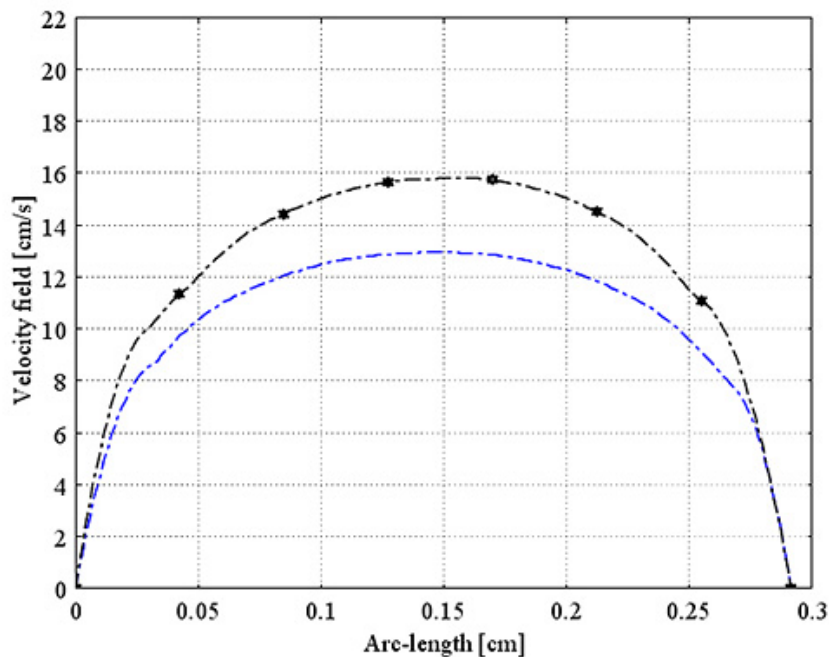


(b)

Figure 6.35: The maximal flow at investigated line b_0b_1 in plane B (Figure 6.8) obtained from the model having 72% stenosed RCA with no graft (solid line) and with a bypass graft (solid line with circle), at two different times: (a) at the peak of systole; and (b) at the peak of diastole.

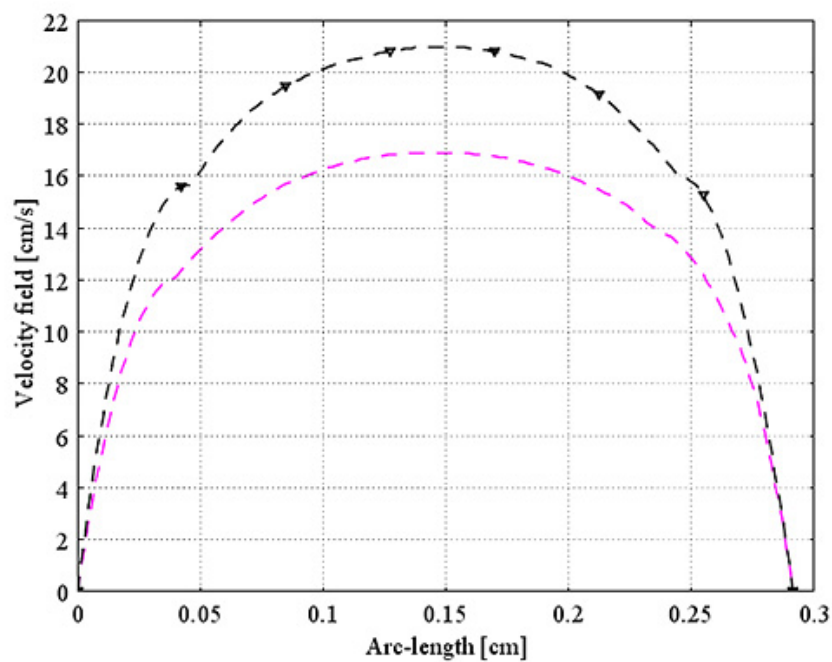


(a)

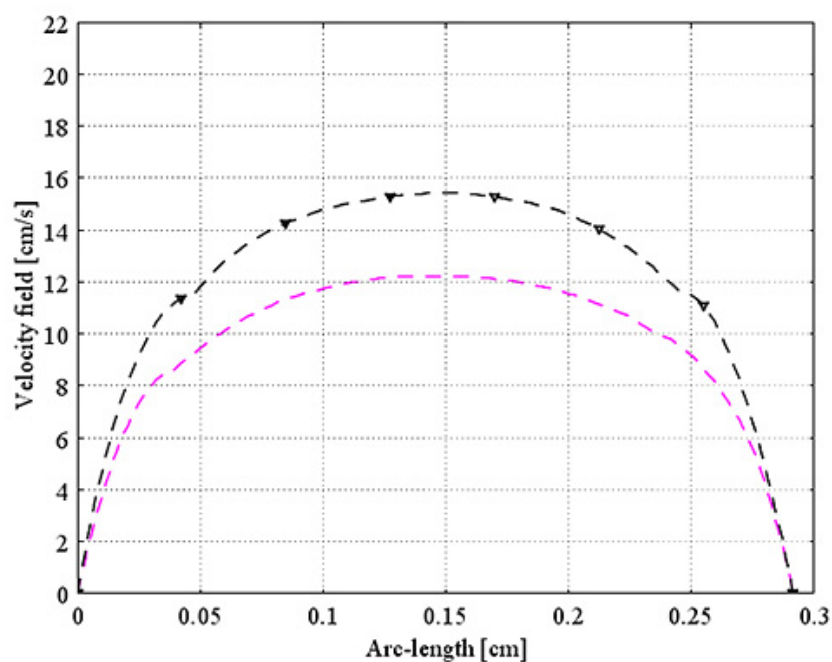


(b)

Figure 6.36: The maximal flow at investigated line c_0c_1 in plane C (Figure 6.8) obtained from the model having 0% stenosed RCA with no graft (dash-dot line) and with a bypass graft (dash-dot line with star), at two different times: (a) at the peak of systole; and (b) at the peak of diastole.

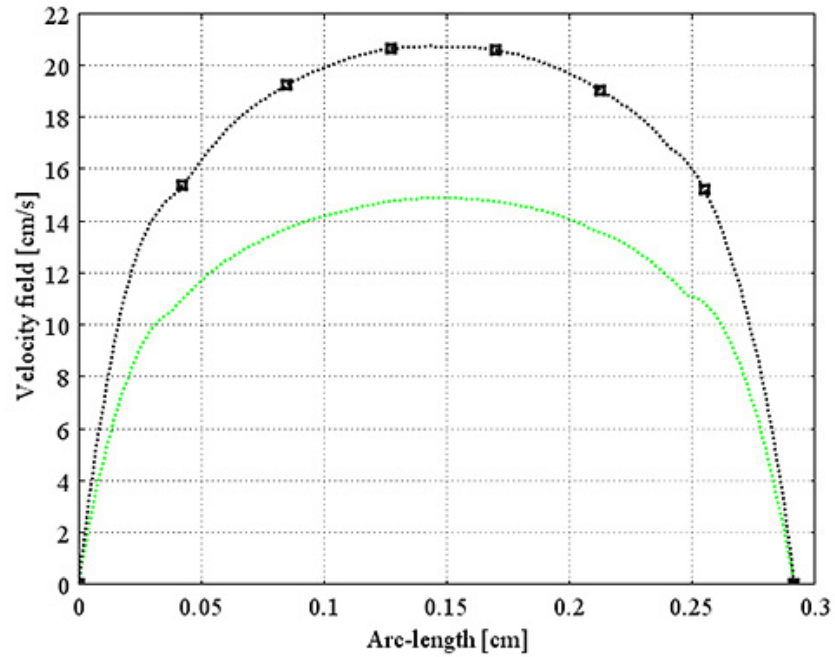


(a)

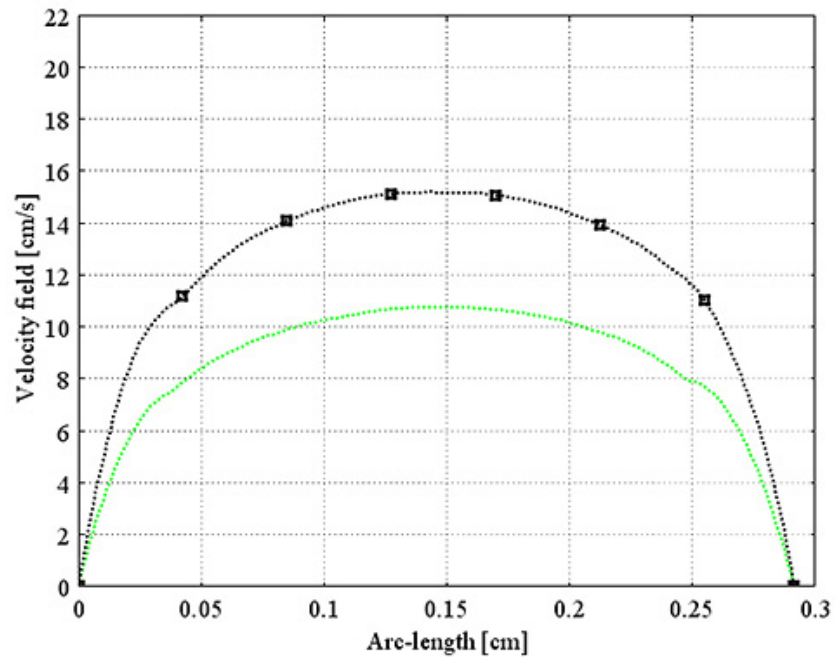


(b)

Figure 6.37: The maximal flow at investigated line c_0c_1 in plane C (Figure 6.8) obtained from the model having 40% stenosed RCA with no graft (dashed line) and with a bypass graft (dashed line with triangle), at two different times: (a) at the peak of systole; and (b) at the peak of diastole.

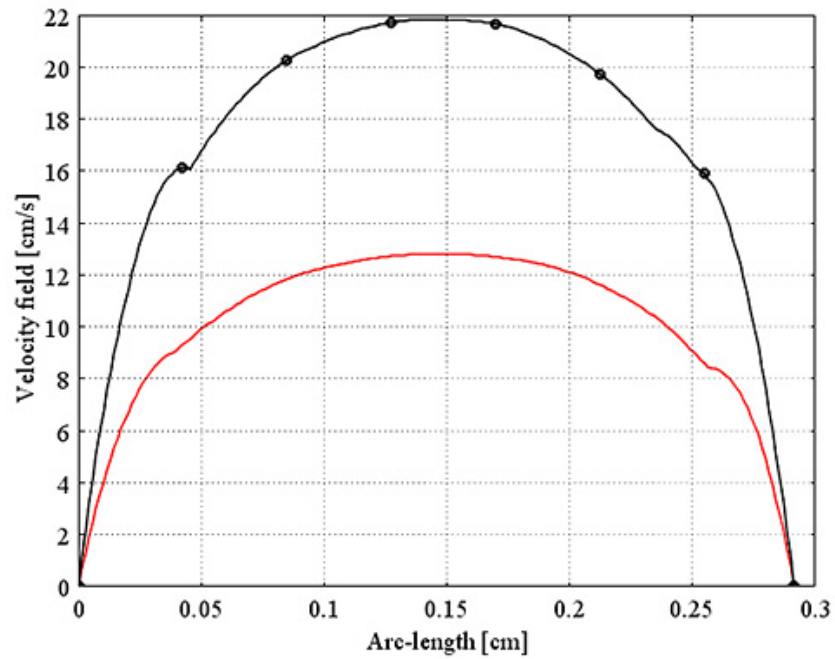


(a)

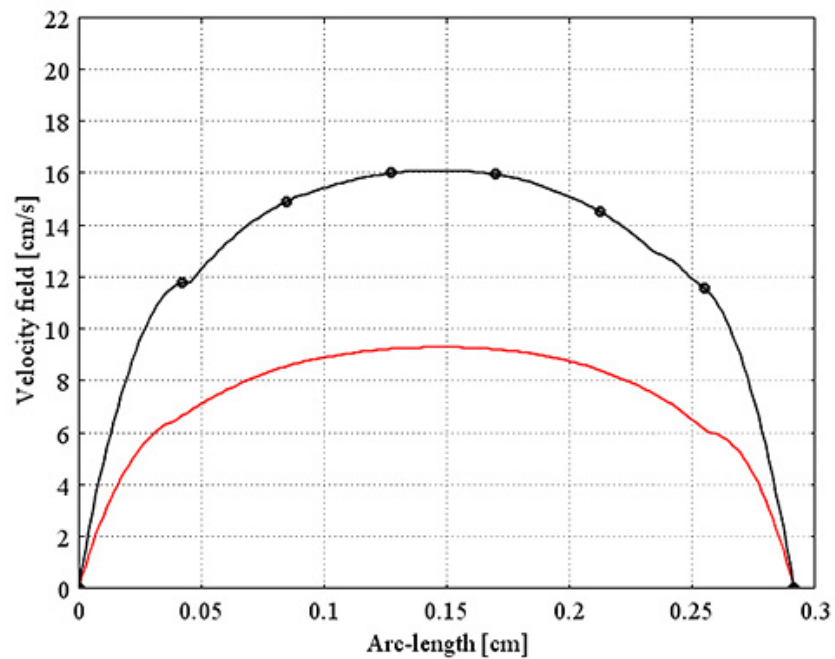


(b)

Figure 6.38: The maximal flow at investigated line c_0c_1 in plane C (Figure 6.8) obtained from the model having 63% stenosed RCA with no graft (dotted line) and with a bypass graft (dotted line with square), at two different times: (a) at the peak of systole; and (b) at the peak of diastole.



(a)



(b)

Figure 6.39: The maximal flow at investigated line c_0c_1 in plane C (Figure 6.8) obtained from the model having 72% stenosed RCA with no graft (solid line) and with a bypass graft (solid line with circle), at two different times: (a) at the peak of systole; and (b) at the peak of diastole.

CHAPTER VII

SUMMARY AND CONCLUSIONS

7.1 Summary of the Research

This thesis focuses on the study of the blood flow behavior in the system of human coronary arteries with no graft and with a bypass graft. The three-dimensional computational domain, constructed by using Mimics software, consists of the ascending aorta, the arch of aorta, the proximal left coronary artery, the right coronary artery (RCA), and a graft. Blood is assumed to be an incompressible non-Newtonian fluid. The motion of blood flow is governed by the continuity equation and the Navier-Stokes equations with pulsatile conditions on the boundaries. The numerical simulation is solved by using the COMSOL multiphysics package based on the finite element method. The effect of branching is investigated by using the system of human coronary arteries with no branch and with branches. The effect of the non-Newtonian property, stenosis, and bypass grafting are investigated by using the computational domains as follows:

- a system of human coronary arteries having 0% stenosed RCA,
- a system of human coronary arteries having 40% stenosed RCA,
- a system of human coronary arteries having 63% stenosed RCA,
- a system of human coronary arteries having 72% stenosed RCA,
- a system of human coronary arteries having 0% stenosed RCA with a bypass graft,
- a system of human coronary arteries having 40% stenosed RCA with a bypass graft,

- a system of human coronary arteries having 63% stenosed RCA with a bypass graft,
- a system of human coronary arteries having 72% stenosed RCA with a bypass graft.

The numerical results obtained from this study are summarized as follows:

- the branching effect reduces the pressure and maximal velocity and increases the wall shear stresses along the RCA axis. The results show that the branchings of the artery have significant effects on the blood flow;

- the non-Newtonian model shows a significantly higher wall shear stress than the Newtonian model. However, it has an insignificant effect on the pressure and the velocity of blood;

- the effect of stenosis shows that in the stenosis region the pressure drops more and the wall shear stress and maximal velocity increase as the degree of stenosis increases. However, the velocity measured after the stenosis region decreases as an increasing of stenosis degree;

- the pressure along the RCA with stenosis region can be improved by coronary artery bypass graft (CABG) surgery, but in the domain with 72% RCA stenosis there is still a drop of blood pressure in the stenosis region. The high wall shear stress around the stenosis site can be decreased by the CABG. The blood velocity in the region between the stenosis site and the graft connected to the RCA decreases but increases below the region of the graft connected to the RCA when bypass grafting.

Therefore, the results obtained from the realistic model is useful for medical diagnosis. These results can help a doctor to predict the coronary artery development and to determine a successful treatment.

REFERENCES

- [1] Aarnoudse W, Van't Veer M, Pijls NH, Ter Woorst J, Vercauteren S, et al. Direct volumetric blood flow measurement in coronary arteries by thermodilution. *Journal of the American College of Cardiology*. 2007;50(24):2294-304.
- [2] Ai L, Vafai K. A coupling model for macromolecule transport in a stenosed arterial wall. *International Journal of Heat and Mass Transfer*. 2006;49:1568-91.
- [3] Amornsamankul S, Wiwatanapataphee B, Wu HY, Lenbury Y. Numerical simulation of blood flow in the stenosed coronary artery. *The Asian Simulation and Modeling Conference*. 2007:195-201.
- [4] Anastasiou AD, Spyrogianni AS, Paras SV. Experimental study of pulsatile blood flow in micro channels. *7th European Congress of Chemical Engineering*. 2010.
- [5] Anastasiou AD, Spyrogianni AS, Koskinas KC, Giannoglou GD, Paras SV. Experimental investigation of the flow of a blood analogue fluid in a replica of a bifurcated small artery. *Medical Engineering & Physics*. 2012;34(2):211-8.
- [6] Bara CL, Verhey JF. Simulation of the fluid dynamics in artificial aortic roots: comparison of two different types of prostheses. *Journal of Artificial Organs*. 2008;11(3):123-9.
- [7] Basombro FG, Dari EA, Buscaglia GC, Feijo RA. Numerical experiments in complex haemodynamic flows. Non-Newtonian effects. *Interna-*

- tional Journal of Computational Fluid Dynamics. 2002;16(4):231-46.
- [8] Beratlis N, Balaras E, Parvinian B, Kiger K. A numerical and experimental investigation of transitional pulsatile flow in a stenosed channel. Journal of Biomechanical Engineering. 2005;127(7):1147-57.
- [9] Bernad SI, Barbat T, Bernad ES, Susan-Resiga R. Cardio vascular surgery - simulation based medical intervention. 9th WSEAS International Conference on Mathematics & Computer in Biology & Chemistry. 2008.
- [10] Bernad SI, Barbat T, Bernad ES, Susan-Resiga R. Numerical blood flow simulations in narrowed coronary venous bypass graft. Journal of Chinese Clinical Medicine. 2009;4(1):1-10.
- [11] Berthier B, Bouzerar R, Legallais C. Blood flow patterns in an anatomically realistic coronary vessel: influence of three different reconstruction methods. Journal of Biomechanics. 2002;35:1347-56.
- [12] Bertolotti C, Deplano V. Three-dimensional numerical simulations of flow through a stenosed coronary bypass. Journal of Biomechanics. 2000;33:1011-22.
- [13] Bertolotti C, Deplano V, Fuseri J, Dupouy P. Numerical and experimental models of post-operative realistic flows in stenosed coronary bypasses. Journal of Biomechanics. 2001;34:1049-64.
- [14] Boutsianis E, Dave H, Frauenfelder T, Poulikakos D, Wildermuth S, Turina M, Ventikos Y, Zund G. Computational simulation of intracoronary flow based on real coronary geometry. European Journal of Cardio-thoracic Surgery. 2004;26:248-56.

- [15] Chaichana T, Sun Z, Jewkes J. Computation of hemodynamics in the left coronary artery with variable angulations. *Journal of Biomechanics*. 2011;44(10):1869-78.
- [16] Chaiyaroj S, Viengteeravat S, Bhumarangura W, Khajarern S, Leelayana P, Purintrapiban B. Techniques and results of off-pump coronary artery bypass grafting using homemade intracoronary shunt. *Journal of the Medical Association of Thailand*. 2006;89(9):1434-9.
- [17] Chaniotis AK, Kaiktsis L, Katritsis D, Efstathopoulos E, Pantos I, Marmarelis V. Computational study of pulsatile blood flow in prototype vessel geometries of coronary segments. *Physical Medicine*. 2010;26(3):140-56.
- [18] Chen J, Lu XY. Numerical investigation of the non-Newtonian blood flow in a bifurcation model with a non-planar branch. *Journal of Biomechanics*. 2004;37:1899-911.
- [19] Chen J, Lu XY. Numerical investigation of the non-Newtonian pulsatile blood flow in a bifurcation model with a non-planar branch. *Journal of Biomechanics*. 2006;39:818-32.
- [20] Chen J, Lu XY, Wang W. Non-Newtonian effects of blood flow on hemodynamics in distal vascular graft anastomoses. *Journal of Biomechanics*. 2006;39:1983-95.
- [21] Cheung SCP, Wong KKL, Yeoh GH, Yang W, Tu J, Beare R, Phan T. Experimental and numerical study on the hemodynamics of stenosed carotid bifurcation. *Australasian Physical and Engineering Sciences in Medicine*. 2010;33:319-28.

- [22] Cho YI, Kensey KR. Effect of the non-Newtonian viscosity of blood on flows in a diseased arterial vessel. Part 1: Steady flows. *Biorheology*. 1991;28:241-62.
- [23] Chuchard P, Wiwatanapataphee B, Puapansawat T, Siriapisith T. Numerical simulation of blood flow in the system of human coronary arteries with stenosis. *Proceedings of the 4th WSEAS International Conference on Finite Differences - Finite Elements - Finite Volumes - Boundary Elements*. 2011;59-63.
- [24] Chuchard P, Puapansawat T, Siriapisith T, Wu YH, Wiwatanapataphee B. Numerical simulation of blood flow through the system of coronary arteries with diseased left anterior descending. *International Journal of Mathematics and computers in Simulation*. 2011;5(4):334-41.
- [25] Davis JM, Pozrikidis C. Numerical simulation of unsteady blood flow through capillary networks. *Bulletin of Mathematical Biology*. 2011; 73:1857-80.
- [26] Deplano V, Siouffi M. Experimental and numerical study of pulsatile flows through stenosis: Wall shear stress analysis. *Journal of Biomechanics*. 1999;32:1081-90.
- [27] Espinola-Klein C, Rupprecht HJ, Erbel R, Nafe B, Brennecke R, Meyer J. Ten-year outcome after coronary angioplasty in patients with single-vessel coronary artery disease and comparison with the results of the coronary artery surgery study (CASS). *Am J Cardiol* 2000;85:321-6.
- [28] Ethier CR, Steinman DA, Zhang X, Karpik SR, Ojha M. Flow waveform effects on end-to-side anastomotic flow patterns. *Journal of Biomechanics*. 1998;31:609-17.

- [29] Frauenfelder T, Boutsianis E, Schertler T, Husmann L, Leschka S, et al. Flow and wall shear stress in end-to-side and side-to-side anastomosis of venous coronary artery bypass grafts. *BioMedical Engineering On-Line*. 2007;6(35):1-13.
- [30] Frauenfelder T, Boutsianis E, Schertler T, Husmann L, Leschka S, et al. In-vivo flow simulation in coronary arteries based on computed tomography datasets: feasibility and initial results. *European Radiology*. 2007;17:1291-300.
- [31] Garcia V, Dias R, Lima R. In vitro blood flow behaviour in microchannels with simple and complex geometries. *Applied Biological Engineering - Principles and Practice*, Dr. Ganesh R. Naik (Ed.), ISBN:978-953-51-0412-4. 2012:393-416.
- [32] Grinberg L, Cheever E, Anor T, Madsen JR, Karniadakis GE. Modeling blood flow circulation in intracranial arterial networks: A comparative 3D/1D simulation study. *Annals of Biomedical Engineering*. 2010.
- [33] Huang ZJ, Tarbell JM. Numerical simulation of mass transfer in porous media of blood vessel walls. *American Journal of Physiology - Heart and Circulatory Physiology*. 1997;273:H464-H477.
- [34] Ishikawa T, Guimaraes LFR, Oshima S, Yamane R. Effect of non-Newtonian property of blood on flow through a stenosed tube. *Fluid Dynamics Research*. 1998;22:251-64.
- [35] Jafari A, Mousavi SM, Kolari P. Numerical investigation of blood flow. Part I: In microvessel bifurcations. *Communications in Nonlinear Science and Numerical Simulation*. 2008;13(8):1615-26.

- [36] Jafari A, Zamankhan P, Mousavi SM, Kolari P. Numerical investigation of blood flow. Part II: In capillaries. *Communications in Nonlinear Science and Numerical Simulation*. 2009;14(4):1396-402.
- [37] Janela J, Moura A, Sequeira A. A 3D non-Newtonian fluid-structure interaction model for blood flow in arteries. *Journal of Computational and Applied Mathematics*. 2010;234:2783-91.
- [38] Johnston BM, Johnston PR, Corney S, Kilpatrick D. Non-Newtonian blood flow in human right coronary arteries: steady state simulations. *Journal of Biomechanics*. 2004;37:709-20.
- [39] Johnston BM, Johnston PR, Corney S, Kilpatrick D. Non-Newtonian blood flow in human right coronary arteries: transient simulations. *Journal of Biomechanics*. 2006;39:1116-28.
- [40] Jonsdottir H, Baldursdottir L. The experience of people awaiting coronary artery bypass graft surgery: the Icelandic experience. *Journal of Advanced Nursing*. 1998;27:68-74.
- [41] Jung H, Choi JW, Park CG. Asymmetric flows of non-Newtonian fluids in symmetric stenosed artery. *Korea-Australia Rheology Journal*. 2004;16(2):101-8.
- [42] Kang MJ, Ji HS, Kim KC. In-vitro investigation of RBCs flow characteristics and hemodynamic feature through a microchannel with a microstenosis. *International Journal of Biology and Biomedical Engineering*. 2008;1(2):1-8.
- [43] Karner G, Perktold K. Effect of endothelial injury and increased blood pressure on albumin accumulation in the arterial: a numerical study. *Journal of Biomechanics*. 2000;33:709-15.

- [44] Kung EO, Les AS, Figueroa CA, Medina F, Arcaute K, et al. In vitro validation of finite element analysis of blood flow in deformable models. *Annals of Biomedical Engineering*. 2011;39(7):1949-60.
- [45] Laustsen J, Paaske WP, Oyre S, Pedersen EM. Dynamic quantification, visualisation and animation of blood velocities and flows in infrarenal aortic aneurysms in vivo by three-dimensional MR phase velocity encoding. *European Journal of Vascular and Endovascular Surgery*. 1995;9:383-8.
- [46] Li MX, Beech-Brandt JJ, John LR, Hoskins PR, Easson WJ. Numerical analysis of pulsatile blood flow and vessel wall mechanics in different degrees of stenoses. *Journal of Biomechanics*. 2007;40(16):3715-24.
- [47] Manimaran R. CFD simulation of non-Newtonian fluid flow in arterial stenoses with surface irregularities. *World Academy of Science, Engineering and Technology*. 2011;73:957-62.
- [48] McCommis KS, Goldstein TA, Abendschein DR, Misselwitz B, Pilgram T, Gropler RJ, Zheng J. Roles of myocardial blood volume and flow in coronary artery disease: an experimental MRI study at rest and during hyperemia. *European Radiology*. 2010;20:2005-12.
- [49] Morega AM, Dobre A, Morega M, Mocanu D. Computational Modeling of Arterial Blood Flow. *International Conference on Advancements of Medicine and Health Care through Technology. IFMBE Proceedings*. 2009;26:373-8.
- [50] Mustapha N, Mandal PK, Johnston PR, Amin N. A numerical simulation of unsteady blood flow through multi-irregular arterial stenoses. *Applied Mathematical Modelling*. 2010;34(6):1559-73.

- [51] Nag D, Datta A. Steady laminar flow of blood through successive restrictions in circular conduits of small diameter. *Proceedings of the Institution of Mechanical Engineers, Part C*. 2008;222:1557-73.
- [52] Nipawan T, Wiwatanapataphee B, Siriapisith T, Phoocharoen N, Wu YH. Effect of bypass graft on blood flow in stenotic coronary artery reconstructed from medical images. *Proceedings of the 5th Asian Mathematical Conference*. 2009.
- [53] Papaharilaou Y, Doorlya DJ, Sherwina SJ. The influence of out-of-plane geometry on pulsatile flow within a distal end-to-side anastomosis. *Journal of Biomechanics*. 2002;35:1225-39.
- [54] Park SM, Min YU, Kang MJ, Ji HS, Kim KC. In-vitro investigation of blood flow characteristics in stenotic right coronary artery. *Proceedings of SPIE, Fourth International Conference on Experimental Mechanics*. 2010;75226A.
- [55] Poltem D, Wiwatanapataphee B, Wu YH. A numerical study of non-Newtonian blood flow in stenosed coronary artery bypass with grafts. *Australian and New Zealand Industrial and Applied Mathematics Journal*. 2006;47:C277-C291.
- [56] Pozrikidis C. Numerical simulation of blood flow through microvascular capillary networks. *Bulletin of Mathematical Biology*. 2009;71:1520-41.
- [57] Ruengsakulrach P, Joshi AK, Fremes S, Butany J, Foster S, et al. Wall shear stress and atherosclerosis: numerical blood flow simulations in the mouse aortic arch. *12th WSEAS International Conference on Applied Mathematics*. 2007;199-207.

- [58] Sadeghian S, Navidbakhsh M, Molaie R. Numerical flow analysis in actual model of human coronary. 3rd WSEAS International Conference on Applied and Theoretical Mechanics. 2007;131-5.
- [59] Samijo SK, Willigers JM, Barkhuysen R, Kitslaar PJEHM, Reneman RS, et al. Wall shear stress in the human common carotid artery as function of age and gender. *Cardiovascular Research*. 1998;39: 515-22.
- [60] Sankaran S, Moghadam ME, Kahn AM, Tseng EE, Guccione JM, Marsden AL. Patient-specific multiscale modeling of blood flow for coronary artery bypass graft surgery. *Annals of Biomedical Engineering*. 2012.
- [61] Sankaranarayanan M, Chua LP, Ghista DN, Tan YS. Computational model of blood flow in the aorto-coronary bypass graft. *Biomedical Engineering Online*. 2005;4:1-13.
- [62] Sarifuddin, Chakravarty S, Mandal PK. Effect of heat and mass transfer on non-Newtonian flow links to atherosclerosis. *International Journal of Heat and Mass Transfer*. 2009;52:5719-30.
- [63] Shaaban AM, Duerinckx AJ. Wall shear stress and early atherosclerosis: a review. *American Journalism Review*. 2000;174:1657-65.
- [64] Shaik E, Hoffmann KA, Dietiker JF. Numerical simulations of pulsatile non-Newtonian flow in an end-to-side anastomosis model. *Simulation Modelling Practice and Theory*. 2008;16:1123-35.
- [65] Shalman E, Rosenfeld M, Dgany E, Einav S. Numerical modeling of the flow in stenosed coronary artery. The relationship between main hemodynamic parameters. *Computers in Biology and Medicine*. 2002; 32:329-44.

- [66] Sherwin SJ, Formaggia L, Peiro J, Franke V. Computational modelling of 1D blood flow with variable mechanical properties and its application to the simulation of wave propagation in the human arterial system. *International Journal for Numerical Methods in Fluids*. 2003; 43:673700.
- [67] Siddiqui SU, Verma NK, Mishra S, Gupta RS. Mathematical modelling of pulsatile flow of Cassons fluid in arterial stenosis. *Applied Mathematics and Computation*. 2009;210:1-10.
- [68] Siddiqui SU, Verma NK, Gupta RS. A mathematical model for pulsatile flow of Herschel-Bulkley fluid through stenosed arteries. *e-Journal of Science & Technology*. 2010;5(4):49-66.
- [69] Soulis JV, Giannoglou GD, Chatzizisis YS, Seralidou KV, Parcharidis GE, Louridas GE. Non-Newtonian models for molecular viscosity and wall shear stress in a 3D reconstructed human left coronary artery. *Medical Engineering & Physics*. 2008;30:9-19.
- [70] Staalsen NH, Pedersen EM, Ulrich M, Winther J, How TV, Hasenkam JM. An in vivo model for studying the local haemodynamics of end-to-side anastomoses. *European Journal of Vascular and Endovascular Surgery*. 1995;9:152-61.
- [71] Staalsen NH, Ulrich M, Kim WY, Pedersen EM, How TV, Hasenkam JM. An in vivo analysis and three-dimensional visualisation of blood flow patterns at vascular end-to-side anastomoses. *European Journal of Vascular and Endovascular Surgery*. 1995;10:168-81.
- [72] Stangeby DK, Ethier CR. Computational analysis of coupled blood-wall arterial LDL transport. *Journal of Biomechanical Engineering*. 2002;124:1-8.

- [73] Tada S, Tarbell JM. Interstitial flow through the internal elastic lamina affects shear stress on arterial smooth muscle cells. *American Journal of Physiology - Heart and Circulatory Physiology*. 2000;278:H1589-H1597.
- [74] Tan FP, Soloperto G, Bashford S, Wood NB, Thom S, Hughes A, Xu XY. Analysis of flow disturbance in a stenosed carotid artery bifurcation using two-equation transitional and turbulence models. *Journal of Biomechanical Engineering*. 2008;130(6).
- [75] Tang D, Yang C, Kobayashi S, Ku DN. Steady flow and wall compression in stenotic arteries: a three-dimensional thick-wall model with fluid wall interactions. *Journal of Biomechanical Engineering*. 2001; 123:548-57.
- [76] Taylor CA, Hughes TJR, Zarins CK, Effect of exercise on hemodynamic conditions in the abdominal aorta. *Basic research papers*. 1999;1077-89.
- [77] The Cleveland Clinic copyright 1995-2012. Medical Management of Coronary Artery Disease. http://my.clevelandclinic.org/heart/disorders/cad/treatment_medical.aspx [Accessed April 2011].
- [78] Tu C, Deville M. Pulsatile flow of non-Newtonian fluids through arterial stenoses. *Journal of Biomechanics*. 1996;29(7):899-908.
- [79] U-King-Im JM, Trivedi RA, Sala E, Graves MJ, Gaskarth M, et al. Evaluation of carotid stenosis with axial high-resolution black-blood MR imaging. *Eur Radiol*. 2004;14:1154-61.

- [80] Varghese SS, Frankel SH. Numerical modeling of pulsatile turbulent flow in stenotic vessels. *Journal of Biomechanical Engineering*. 2003;125:445-60.
- [81] Vasava P, Jalali P, Dabagh M. Pulsatile blood flow simulations in aortic arch: effects of blood pressure and the geometry of arch on wall shear stress. *ECIFMBE 2008, IFMBE Proceedings*. 2008;22:1926-9.
- [82] Vimmr J, Jonasava A. Computer Simulation of non-Newtonian effects on blood flow in a complete 3D bypass model. 8th World Congress on Computational Mechanics, 5th European Congress on Computational Methods in Applied Sciences and Engineering. 2008.
- [83] Vimmr J, Jonasava A. Non-Newtonian effects of blood flow in complete coronary and femoral bypasses. *Mathematics and Computers in Simulation*. 2010;80(6):1324-36.
- [84] Vimmr J, Jonasava A, Bublik O. Non-Newtonian effects of pulsatile blood flow in a realistic bypass graft geometry. 18th International Conference of Engineering Mechanics. 2012;1505-16.
- [85] Vorp DA, Steinman DA, Ethier CR. Computational modeling of arterial biomechanics. *Computing in Science & Engineering*. 2001;51-63.
- [86] Wellnhofer E, Osman J, Kertzsch U, Affeld K, Fleck E, Goubergrits L. Flow simulation studies in coronary arteries—impact of side-branches. *Atherosclerosis*. 2010;213(2):47-81.
- [87] Wikibooks. Human Physiology/The Cardiovascular System. http://en.wikibooks.org/wiki/Human_Physiology/The_cardiovascular_system [Accessed October 2011].

- [88] Wiwatanapataphee B, Poltem D, Wu YH, Lenbury Y. Simulation of pulsatile flow of blood in stenosed coronary artery bypass with graft. *Mathematical Biosciences and Engineering*. 2006;3(2):371-83.
- [89] Wiwatanapataphee B. Modelling of non-Newtonian blood flow through stenosed coronary arteries. *Dynamics of Continuous, Discrete and Impulsive Systems Series B: Applications & Algorithms*. 2008; 15:619-34.
- [90] Wiwatanapataphee B, Wu YH, Siriapisith T, Nuntadilok B. Effect of branching on blood flow in the system of human coronary arteries. *Mathematical Biosciences and Engineering*. 2012;9(1):199-214.
- [91] World Health Organization (WHO). Cardiovascular diseases (CVDs). <http://www.who.int/mediacentre/factsheets/fs317/en/index.html> [Accessed October 2012].
- [92] World Health Organization (WHO). The top 10 causes of death. <http://www.who.int/mediacentre/factsheets/fs310/en/index.html> [Accessed October 2012].
- [93] Yin W, Shanmugavelayudam SK, Rubenstein DA. 3D numerical simulation of coronary blood flow and its effect on endothelial cell activation. *Engineering in Medicine and Biology Society. EMBC. Annual International Conference of the IEEE*. 2009;4003-6.
- [94] Zhang MM, Cheng L, Zhou Y. Recent development on fluid-structure interaction control based on surface perturbation. *Dynamics of Continuous, Discrete and Impulsive System, Series B: Applications & Algorithms*. 2007;14(S8):149-65.

- [95] Zhang XJ, Li XY, He F. Numerical simulation of blood flow in stented aneurysm using lattice boltzmann method. APCMBE 2008, IFMBE Proceedings. 2008;19:113-6.
- [96] Zhu H, Qian M, Zou Y, Song R, Niu L, Jiang B, Guang Q, Zheng H. The validation of Echo-PIV technique used in a stenosis model. 5th International Conference on Bioinformatics and Biomedical Engineering. 2011:1-4.

BIOGRAPHY

NAME	Mr. Buraskorn Nuntadilok
DATE OF BIRTH	December 13, 1979
PLACE OF BIRTH	Roi-et, Thailand
INSTITUTIONS ATTENDED	Chiang Mai University, 1998–2002 Bachelor of Science (Mathematics) Mahidol University, 2002–2007 Master of Science (Applied Mathematics) Mahidol University, 2008–2012 Doctor of Philosophy (Mathematics)
HOME ADDRESS	320/79 Moo 8 Thambol Chompoo, Amphur Muang, Lampang, 52100 Thailand
E-MAIL	buraskorn.nun@gmail.com